Electrochemical Energy Reviews (2021) 4:382–446
https://doi.org/10.1007/s41918-020-00093-0

REVIEW ARTICLE

High-Mass-Loading Electrodes for Advanced Secondary Batteries and Supercapacitors

Feng Wu[1,2] · Mingquan Liu[1] · Ying Li[1] · Xin Feng[1] · Kun Zhang[1] · Ying Bai[1] · Xinran Wang[1] · Chuan Wu[1,2]

Received: 26 September 2020 / Revised: 27 October 2020 / Accepted: 31 December 2020 / Published online: 25 March 2021

Abstract

The growing demand for advanced electrochemical energy storage systems (EESSs) with high energy densities for electric vehicles and portable electronics is driving the electrode revolution, in which the development of high-mass-loading electrodes (HMLEs) is a promising route to improve the energy density of batteries packed in limited spaces through the optimal enlargement of active material loading ratios and reduction of inactive component ratios in overall cell devices. However, HMLEs face significant challenges including inferior charge kinetics, poor electrode structural stability, and complex and expensive production processes. Based on this, this review will provide a comprehensive summary of HMLEs, beginning with a basic presentation of factors influencing HMLE electrochemical properties, the understanding of which can guide optimal HMLE designs. Rational strategies to improve the electrochemical performance of HMLEs accompanied by corresponding advantages and bottlenecks are subsequently discussed in terms of various factors ranging from inactive component modification to active material design to structural engineering at the electrode scale. This review will also present the recent progress and approaches of HMLEs applied in various EESSs, including advanced secondary batteries (lithium-/sodium-/potassium-/aluminum-/calcium-ion batteries, lithium metal anodes, lithium-sulfur batteries, lithium-air batteries, zinc batteries, magnesium batteries) and supercapacitors. Finally, this review will examine the challenges and prospects of HMLE commercialization with a focus on thermal safety, performance evaluation, advanced characterization, and production cost assessment to guide future development.

Keywords High mass loading · Thick electrode · High energy density · Advanced secondary battery · Supercapacitor

Abbreviations

EESSs	Electrochemical energy storage systems
AMs	Active materials
NMC	Lithium Ni–Mn–Co oxide
GITT	Galvanostatic intermittent titration technique
EIS	Electrochemical impedance spectroscopy
NMC622	$LiNi_{0.6}Mn_{0.2}Co_{0.2}O_2$
CAs	Conductive additives
LCO	$LiCoO_2$
LFP	$LiFePO_4$
CB	Carbon black
XPS	X-ray photoelectronic spectroscopy
EDS	Energy-dispersive spectrometer
FTIR	Fourier transform infrared spectrometer
CMC	Carboxymethyl cellulose
PAA	Poly(acrylic acid)
PEO	Polyethylene oxide
PC	Porous carbon
SSA	Specific surface area
DFT	Density functional theory
PVP	Polyvinyl pyrrolidone
CVD	Chemical vapor deposition
ALD	Atomic layer deposition
VAN	Vertically aligned nanostructure
GO	Graphene oxide
CNTs	Carbon nanotubes
BIEF	Built-in electric field
NVP	$Na_3V_2(PO_4)_3$
GICs	Graphite intercalation compounds
PIL	Poly(ionic liquid)
3D-CSE	3D conductive scaffold electrode
ICNEs	Integrated composite network-based electrodes
CNF	Cellulose nanofiber

✉ Chuan Wu
chuanwu@bit.edu.cn

[1] School of Materials Science and Engineering, Beijing Institute of Technology, Beijing 100081, China

[2] Collaborative Innovation Center of Electric Vehicles in Beijing, Beijing 100081, China

LTP	$Li_4Ti_5O_{12}$
PVA	Poly(vinyl alcohol)
CSP	Cold sintering process
NCM	$LiNi_{0.8}Co_{0.1}Mn_{0.1}O_2$
NCA	$LiNi_{0.8}Co_{0.15}Al_{0.05}O_2$
LNMO	$LiNi_{0.5}Mn_{1.5}O_4$
Na-GICs	Sodium–graphite intercalation compounds
ASC	Asymmetric supercapacitor

1 Introduction

Clean and sustainable energy storage techniques have attracted tremendous attention due to the pressing energy crisis involving the deletion of fossil fuels. And considering the unstable and intermittent nature of renewable energy production from water, wind, solar, and geothermal sources, advanced electrochemical energy storage systems (EESSs) are critical power supplies in emerging electric vehicle, smart grid and portable electronic device applications [1]. And among various EESSs, rechargeable batteries (RBs) and supercapacitors (SCs) are particularly promising and have been widely applied in different applications due to distinct charge/discharge mechanisms. In terms of RBs, energy is stored through redox reactions under evaluated electrochemical potentials and involves the reversible insertion/extraction of metal ions to/from active host materials to provide relatively high energy density but low power density due to slow charge kinetics [2], allowing RBs to be particularly suitable for electronic devices in long-term operations. Alternatively, SCs possess high charge/discharge rates and power densities due to relatively fast electrochemical processes based on rapid ion absorption/desorption or fast surface redox reactions [3]. However, SC energy densities are far lower than RBs due to limited active surfaces for ion accumulation, meaning SCs are more suitable for application in rapid power supply and immediate stop-and-go recovery systems. Accordingly, great efforts have been devoted in the past decades to the development of corresponding EESSs with high energy density and uncompromised power density; however, enormous challenges remain. In general, advanced strategies proposed to obtain high energy EESSs include: (1) the development of emerging battery systems based on newly discovered electrochemical mechanisms such as multi-electron reaction systems [4]; (2) the broadening of battery electrochemical potential windows through rational strategies such as electrolyte engineering [5]; (3) the design of anode/cathode active materials (AMs) to achieve high specific capacity; and (4) the engineering of electrode structures to achieve ideal battery configurations with high mass loadings [6].

Overall, RBs and SCs are comprised of similar components, including positive/negative electrodes, a separator, an electrolyte, a current collector and a cell case. Among these, electrode materials have decisive impacts on the electrochemical performance of EESSs and recent reviews have provided comprehensive overviews of corresponding novel AMs [7–10]. In brief, the AM design principle can be summarized into the fine-tuning of electrical/ionic conductivity, intrinsic electronic states, morphological/dimensional adaptability, structural stability, high capacity, and low-cost properties in which problem-oriented methods such as morphology regulation, electronic structure tuning, pore structure control, heteroatoms doping, and composite AM design have attracted significant interest and have been employed to fabricate ideal AMs. Of these, the design of nanostructured AMs is the most appealing to improve EESS electrochemical performance due to advantages including: (1) shortened ionic diffusion distances; (2) enlarged electrode/electrolyte contact areas; (3) suppressed volume variations during ion insertion/extraction; (4) increased AM utilization efficiency; and (5) homogenized AM coatings or distributions on composite slurries [11]. Despite this, the great progress of AM design is mainly focused on the intrinsic performance evaluation of AMs in which corresponding electrode configurations are mostly based on ultrathin slurry film coatings (low mass loading) on current collectors [6, 12]. And because gravimetric performance as a common performance parameter is based on the amount of energy stored per unit weight, the inclusion of overall device component mass (including electrodes, polymer binders, conductive additives, current collectors, separators, electrolytes, and packing units) will lead to significantly lower gravimetric performances in these ultrathin electrodes as compared with values obtained based only on AM mass [13]. However, performance parameters based on overall device mass are of practical significance in electric vehicle, portable and miniaturized electronics applications that require power sources that can deliver maximum energy in very limited spaces and therefore, to realize the commercial application of AMs and achieve high energy density EESSs [14], ideal battery configurations should involve the rational design of high-mass-loading electrodes (HMLEs) with low mass ratios of passive components [6, 12, 15, 16]. However, research into the differences between laboratory and commercial devices remains insufficient and effective strategies for HMLEs are still in early stages.

Based on the different electrode configurations of HMLEs and conventional ultrathin film electrodes (Fig. 1a, b), HMLEs possess clear advantages, including (1) lowered production costs due to the reduction of inactive components and (2) significantly enhanced overall energy densities in the limited spaces of devices due to full occupation by AMs [17]. Despite this, the current progress of advanced HMLEs to achieve equivalent electrochemical performances to conventional ultrathin electrodes remains lacking. One reason involves unfavorable cohesion with AMs and weak attachment between AMs and current collectors that can give rise

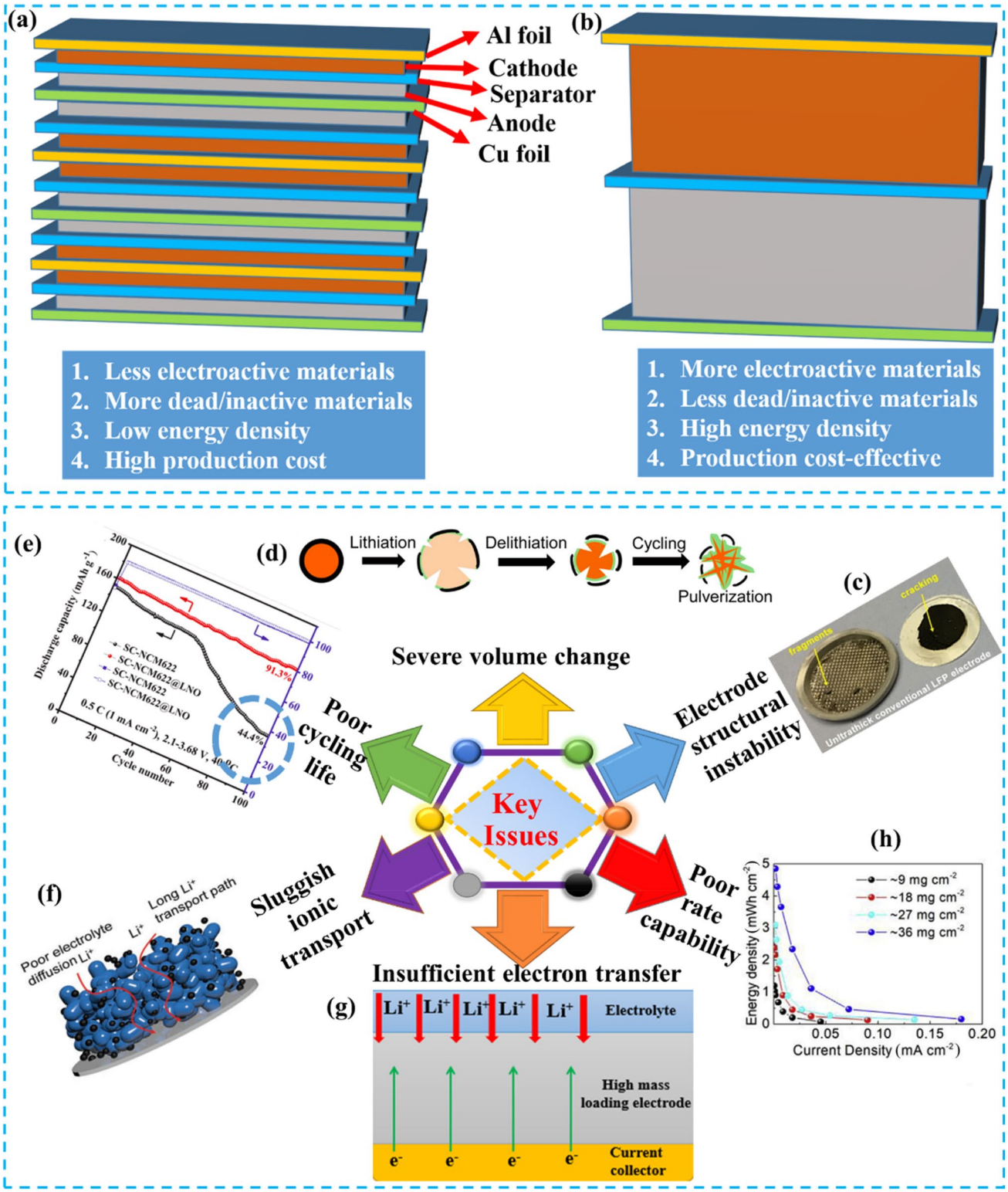

Fig. 1 **a** Low mass loading electrode configuration and its disadvantages. **b** High mass loading electrode configuration and its advantages. **c**–**h** Key issues of HMLEs. **c** Electrode deformation after long-term cycling. Reprinted with permission from Ref. [18]. Copyright © 2017, Wiley–VCH. **d** Schematic of silicon expansion after cycling. Reprinted with permission from Ref. [24]. Copyright © 2014, American Chemical Society. **e** Poor cycling performances of HMLEs derived from conventional coating processes showing only 44% capacity retention after 100 cycles. Reprinted with permission from Ref. [25]. Copyright © 2020, Elsevier. **f** Poor electrolyte diffusion. Reprinted with permission from Ref. [17]. Copyright © 2017, Wiley–VCH. **g** Limited charge transfer depth in conventional 2D current collector-based electrodes. **h** Poor rate capability. Reprinted with permission from Ref. [26]. Copyright © 2019, Elsevier

to weakened electrode mechanical strength (Fig. 1c) and cause the easy fracture and delamination of AMs from current collectors during charge/discharge [18]. In addition, AMs can experience severe volume variation (Fig. 1d) due to the significant accumulation of internal micro-strains during metal ion insertion/extraction [19]. These adverse dynamic microstructural variations can also affect stable solid electrolyte interphase (SEI) formation, which can result in the poor cycling life of corresponding HMLEs (Fig. 1e) [20]. Another prominent issue of advanced HMLEs involves poor electron/ion transport efficiency due to ultrathick electrode designs in which HMLEs based on conventional slurry coating processes are densely packed and possess high tortuosity, which will lead to low electrolyte diffusion efficiency (Fig. 1f) and limited electron transfer depth (Fig. 1g) [12, 17]. These factors will also considerably increase battery polarization and capacity degradation during cycling that are further exasperated under high current density or fast scan rates. In other words, the rate performance (Fig. 1h) and power density of HMLEs are relatively poor compared with conventional thin electrodes. The poorly developed pore structure of dense slurry coatings on HMLEs can further result in weak affinity and limited electrode/electrolyte contact area to increase charge transfer resistance and low electron/ion transport efficiency can lead to uncontrollable dendrite formation during metal plating/stripping [21], which can penetrate separators to result in short circuiting and potential safety hazards [22]. Based on all of this, the exploration of novel electrode material chemistry and advanced electrode configurations to address these issues is urgently needed as the development of HMLEs remains in early stages.

And although pioneering reviews in recent years have discussed HMLE designs in EESSs such as thick electrodes for lithium batteries through low-tortuosity structural design [6] and vertically aligned nanostructure design [16], hierarchical 3D electrodes design [12], pseudocapacitor electrode design under high mass loading [23], these generally focus on the summarization of special or single strategies or limited EESS application (for SCs or lithium batteries only). To address this, this review will provide a current and comprehensive overview of emerging HMLEs with special attention on recent developments in advanced HMLEs towards EESS applications. This review will first provide a basic understanding of HMLE electrochemical properties and based on these understandings, this review will subsequently provide an overview of pioneering strategies in the design of advanced HMLEs to meet the requirements of high-performance EESSs, including inactive component optimization, electroactive material modulation and integrated electrode construction. This review will further discuss the advantages and disadvantages associated with the further development of these strategies and comprehensively analyze the recent progress of HMLEs in emerging battery systems containing advanced secondary battery systems and supercapacitors. Finally, this review will propose challenges and prospects to guide future development towards reliable HMLEs for commercial application.

2 Basic Electrochemical Behaviors of HMLEs

The development of HMLEs towards practical application requires the in-depth understanding of the fundamental electrochemical behaviors of HMLEs. Based on this, this section will analyze the diverse performance metrics and fundamental parameters reflecting electrochemical behavior as a result of mass loading or electrode thickness change as summarized in Fig. 2.

Pore structures are physical parameters that can determine the electrochemical performance of HMLEs [15, 16]. At the molecular level, hierarchical pore structures (Fig. 2a) can benefit electrolyte diffusion to improve energy storage capacity and rate capability in HMLEs as demonstrated by using a transmission line model proposed by Black et al. [27] and experimental data obtained by Ervin et al. [28]. However, the correlation between ultra-micropores (pore sizes smaller than ions) and capacity enhancements remains controversial as first reported by Chmiola et al. [29] and has since attracted many follow-up studies. Correspondingly, ion de-solvation and correlated superionic state theories based on molecular simulations have been proposed, involving the storage of ions in pores resulting from de-shelled ionic solvation shells [30], and the entering of pores with sizes comparable to or smaller than ion sizes [31]. Subsequently, great efforts have been devoted to the further understanding of influences based on pore width, shape, and spatial distribution on electrochemical performance in which advanced characterization methods such as Raman spectroscopy combined with nuclear magnetic resonance [32], in situ small-angel X-ray scattering [33], in situ X-ray diffraction [34], and density functional theory (DFT) calculations [35] have been carried out. Due to complex interactions between pore sizes, pore volumes, and pore distributions within electrolyte systems (such as ionic liquid, inorganic and aqueous electrolytes), however, reasonable and suitable pore structures obtained through molecular simulations remain difficult. Moreover, these factors become more complex and difficult to study in HMLEs because molecular simulations need to take into consideration electrode mass loading or thickness. Porosity and tortuosity (Fig. 2b) are correlating factors that can influence the internal electrochemical properties of HMLEs, especially electron and ion transfer properties within porous electrodes in which based on the definition of effective diffusion coefficients [6]:

$$D_{\text{eff}} = D_0 \times \frac{\varepsilon}{\tau} \tag{1}$$

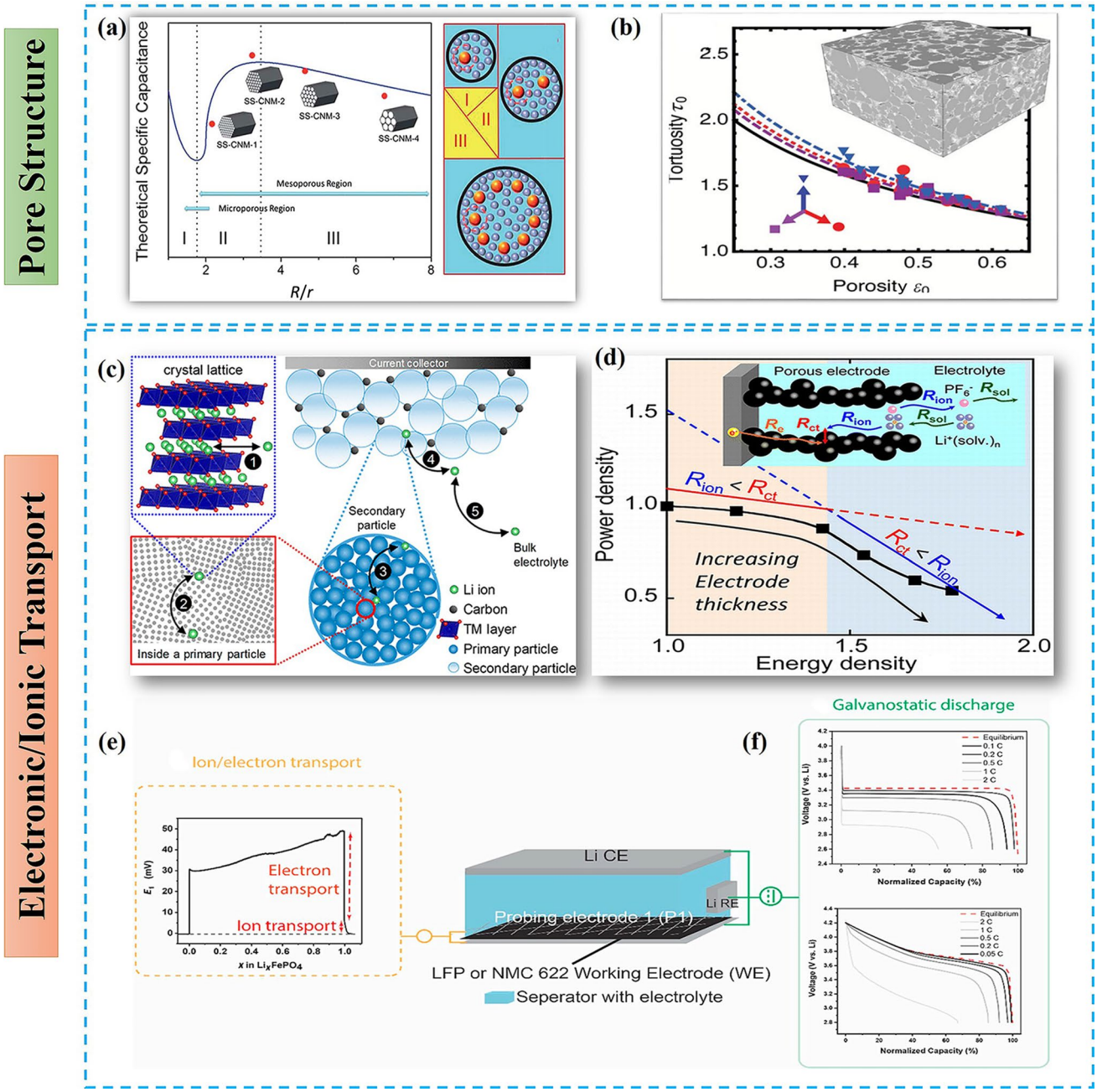

Fig. 2 The basic electrochemical behaviors of HMLEs. **a** The theoretical capacitance of porous carbons with different pore sizes. Reprinted with permission from Ref. [36]. Copyright © 2014, The Royal Society of Chemistry. **b** Relationship between porosity and tortuosity. Reprinted with permission from Ref. [37]. Copyright © 2014, Wiley–VCH. **c** Li ion diffusion pathways from crystal lattices to bulk electrolytes. Reprinted with permission from Ref. [38]. Copyright © 2018, American Chemical Society. **d** Internal resistances of porous electrodes for lithium-ion batteries (LIBs) and the relationship between power density and energy density with changing electrode thickness. Reprinted with permission from Ref. [39]. Copyright © 2015, American Chemical Society. **e** The design of a working electrode for the *operando* measurement of potential drops and **f** the galvanostatic discharge profiles of cells based on LFP (up) and NMC 622 (down) electrodes. Reprinted with permission from Ref. [40]. Copyright © 2020, Elsevier

in which D_0 is the diffusion coefficient of the electrolyte, D_{eff} is the electrode diffusion coefficient, ε is the electrode porosity and τ is the tortuosity. Porosity enlargement and tortuosity reduction can promote ion diffusivity, indicating that the structural engineering of low-tortuosity electrodes can enhance the performance of HMLEs.

The fundamental understanding of internal resistance and electron/ion transport in HMLEs is also important. Based

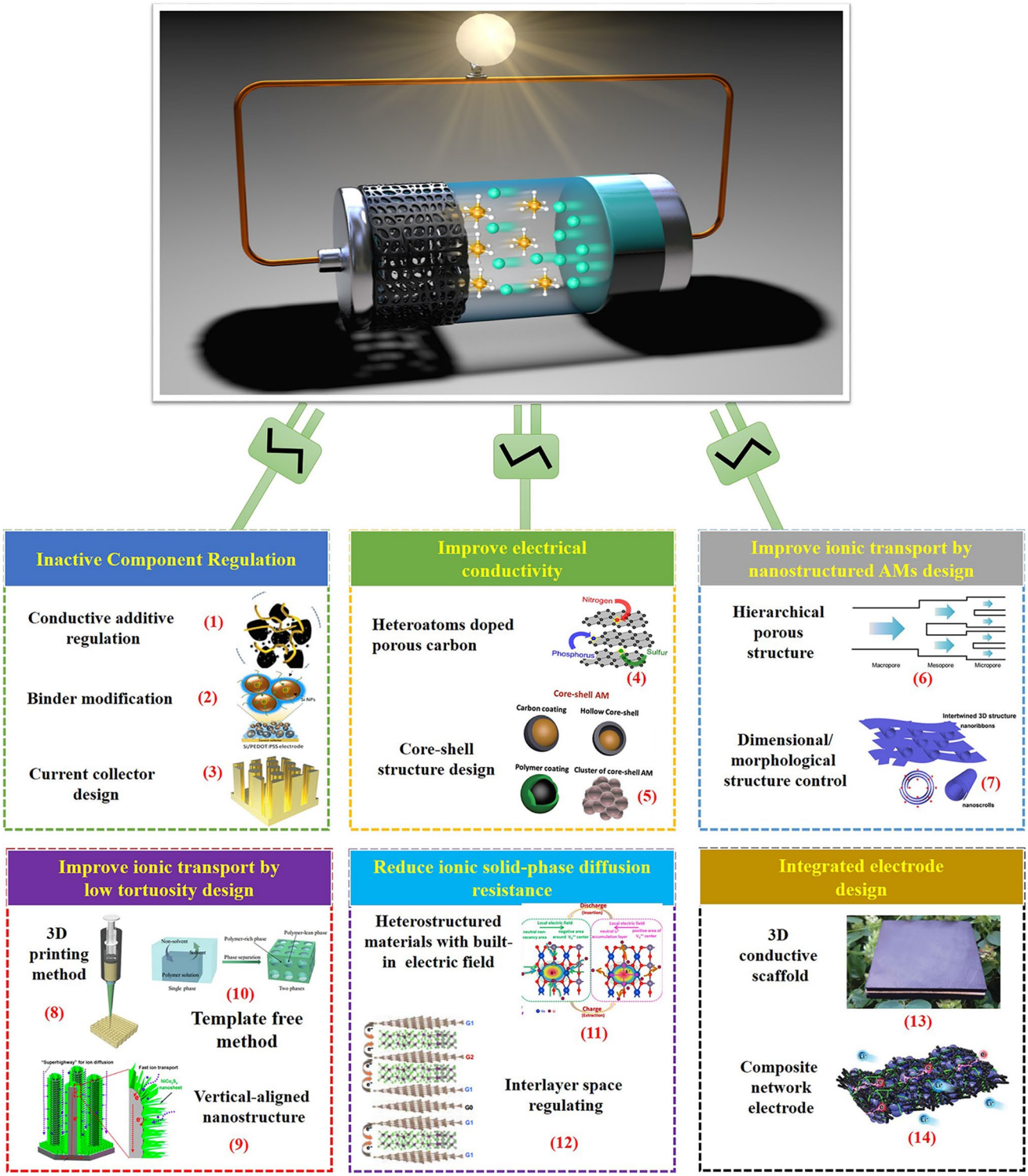

on this, Chen et al. [38] used a lithium Ni–Mn–Co oxide (NMC) cathode 100–300 μm in thickness as a model system to study the rate-limiting Li-ion diffusion pathways within the thick electrode during charge/discharge and reported that Li-ion diffusion from electrodes to electrolytes can be sorted into five categories (Fig. 2c), including solid-phase diffusion into AM crystal structures, solid-phase diffusion into primary particles, liquid-phase diffusion from one primary particle to another particle, liquid-phase diffusion into porous electrodes and liquid-phase diffusion in bulk electrolytes. Galvanostatic intermittent titration technique (GITT) and electrochemical impedance spectroscopy (EIS)

◂**Fig. 3** Overview of advanced strategies summarized in this review. (1) Conductive additive regulation. Reprinted with permission from Ref. [43]. Copyright © 2019, Wiley–VCH. (2) Binder modification. Reprinted with permission from Ref. [44]. Copyright © 2016, American Chemical Society. (3) Current collector regulation. Reprinted with permission from Ref. [45]. Copyright © 2018, Wiley–VCH. (4) Heteroatoms doping in porous carbon. Reprinted with permission from Ref. [46]. Copyright © 2015, American Chemical Society. (5) Core–shell structure design. Reprinted with permission from Ref. [47]. Copyright © 2019, Wiley–VCH. (6) Hierarchical pore structure design. Reprinted with permission from Ref. [48]. Copyright © 2017, The Royal Society of Chemistry. (7) Dimensional morphological structure control. Reprinted with permission from Ref. [49]. Copyright © 2017, Elsevier. (8) 3D printing. Reprinted with permission from Ref. [50]. Copyright © 2020, Wiley–VCH. (9) Vertical-aligned structure design. Reprinted with permission from Ref. [51]. Copyright © 2020, American Chemical Society. (10) Template-free phase separation. Reprinted with permission from Ref. [52]. Copyright © 2019, The Royal Society of Chemistry. (11) Charge density distribution of heterostructured material design. Reprinted with permission from Ref. [53]. Copyright © 2017, American Chemical Society. (12) Interlayer spacing regulation. Reprinted with permission from Ref. [54]. Copyright © 2020, The Royal Society of Chemistry. (13) Wood-based 3D integrated SC. Reprinted with permission from Ref. [55]. Copyright © 2017, The Royal Society of Chemistry. (14) Composite network design. Reprinted with permission from Ref. [56]. Copyright © 2019, Wiley–VCH

measurements were used to quantify Li^+ diffusivity (D_{Li}). These researchers also reported the critical thickness of thick electrodes to be ~200 μm, above which the reduction of specific capacity and rate capability would occur. Through the analysis of D_{Li} versus potential variations of electrodes with increasing thickness, these researchers also confirmed that the rate-limiting mechanism governing diffusion kinetics involved the liquid-phase diffusion region of porous electrodes rather than the solid-state diffusion of Li^+, demonstrating that the structural engineering of electrodes with varying morphology and porous structures can enhance ion transport efficiency. Li et al. [41] also used COMSOL multiphasic software to numerically model the limiting factors of thick electrode performance and obtained a similar critical thickness for optimal volumetric energy density. These researchers further studied the effects of AM particle size, electrolyte molarity and several electrode fabrication methods on thick electrode performance and highlighted cell polarization and material underutilization as key factors offsetting thick electrode performance in which increased electrolyte molarity and nanoscale AM particle size can contribute to enhanced ion diffusion and reduced internal resistance in HMLEs. Takeuchi et al. [39] further combined EIS using a symmetric cell and the transmission line model theory to systematically investigate ionic resistance in pores (R_{ion}) and charge-transfer resistance for Li intercalation (R_{ct}) and found that changes in R_{ion} and R_{ct} negatively correlated with increasing electrode thickness (Fig. 2d). These researchers also reported that the power density of thick electrodes strongly correlated with internal resistance as influenced by R_{ion} and R_{ct}. To further *operando* probe ion and electron transport in porous HMLEs, Wang et al. [40] characterized R_{ion} and R_{ct} of HMLEs based on phase-transformation-type $LiFePO_4$ (LFP) and solid-solution-type $LiNi_{0.6}Mn_{0.2}Co_{0.2}O_2$ (NMC622) with a high mass loading of 20 mg cm^{-2} by measuring the dynamic variations of the potential drop as caused by ion/electron transport (Fig. 2e, f). They highlighted the facts that HMLE capacity loss at high rates was related to the ion/electron potential drop in thick electrodes and that different AMs possess different sensitivities to the potential drop due to different lithiation mechanisms. These researchers also reported that HMLE capacities based on phase transformation materials were more sensitive to the ion/electron transport potential drop as compared with solid solution materials and that the further understanding of the effects of electrode design on battery performance can be obtained by using this method.

Currently, most studies into HMLEs only roughly investigate the influence of mass loading or thickness on battery performance using single or limited controlling experiments that often ignore correlating but vital factors. However, Wood et al. [37] comprehensively quantified and determined the origins of tortuosity anisotropy in different porous electrodes through experimental (synchrotron radiation X-ray tomographic microscopy, electron microscopy) and theoretical (diffusion simulation, differential effective medium approximation) methods. Iyuke et al. [42] carried out modeling analysis to report that many electrochemical merits of HMLEs were co-influenced and required optimization, such as effective electrode thickness utilization (or AM utilization efficiency), optimal applied charge current density and effective electrode and electrolyte conductivity. For example, electrode effective thicknesses can increase with high electrolyte conductivity but decrease with high applied charge current, which suggests the existence of a maximum or optimal charge current, above which effective thickness or AM utilization is reduced.

Based on all of this, enhanced HMLE electrochemical performance can be achieved through the development of hierarchically porous structures, decreased electrode tortuosity, reasonable AM morphology, increased electrolyte molarity, nanosized AM particle sizes, etc. In addition, various performance influencing factors and technical parameters need to be carefully optimized in HMLEs for practical application.

3 Advanced Strategies for High-Performance HMLEs

Various advanced strategies have been developed to tackle the key challenges of HMLEs and improve electrochemical performance. Based on this, this section will summarize

representative strategies in which an overview is provided in Fig. 3.

3.1 Inactive Component Regulation

Slurry coating is a major electrode process in both laboratory and industrial settings. Due to the random self-packing of electrode components through uncontrollable processing however, the homogenous distribution of slurry components is difficult to achieve which will result in poor electrical contact and weak internal adhesion and interconnection of components. This phenomenon is exasperated in the case of HMLEs and can lead to insufficient electron transfer and ion transport. Battery capacity and cycling stability also experience significant reduction under high charge/discharge rates, meaning that the establishment of stable and electron/ion conductive networks through the control of ratios, distribution states, material types and manufacturing conditions for individual electrode components is essential in high performance HMLEs.

3.1.1 Conductive Additive Regulation

AMs such as silicon, sulfur and several metal oxides commonly possess low electrical conductivities making them not conducive to high rate capability electrodes. For example, current LIB cathode materials such as $LiCoO_2$ (10^{-3} S cm^{-1}), $LiMn_2O_4$ (10^{-5} S cm^{-1}), $LiFePO_4$ (10^{-9} S cm^{-1}) and $LiNiO_2$ (10^{-2} S cm^{-1}) generally experience low electronic conductivity [57]. Here, the addition of conductive additives (CAs) with a certain compensation ratio of AMs can enhance the overall electronic conductivity of electrodes in which CA/AM electrical contact states differ based on the dimensional/morphological properties of CAs and AMs and can be classified into four types (Fig. 4a), including: (1) widely studied composite slurries based on powdered AMs coupled with powdered carbon black to show "point-to-point" electrical contact; (2) "point-to-line" electrical contact between powdered AMs and 1D carbon nanofibers or nanotubes (CFs or CNTs); (3) "point-to-plane" electrical contact for powdered AMs coupled with 2D CAs (e.g., graphene and MXene); and (4) "plane-to-plane" electrical contact derived from 2D AMs connected to 2D CAs. And because many advanced electrode designs possess multiple electrical contact states due to the constitution of various dimensional/morphological AMs and CAs, corresponding identification is often difficult.

Among CAs, carbon black (CB) with "point-to-point/line/plane" electrical contact is the most commonly studied due to advantages including cost effectiveness, easy fabrication and resource abundance. However, the irregular morphological properties and non-uniform distributions of CB make corresponding electrode conductivity and battery performance generally insufficient. Here, the simplest method to improve CB-based electrode performance is to control CB versus AM ratios in composites. In addition, the rational change of electrode manufacturing processes can ensure the uniform distribution of CB in composites to enhance the electrical conductivity of electrodes. The introduction of capillary suspensions into slurry preparation can further allow for a stable composite graphite/CB/binder electrode with a mass loading of 16.5 mg cm^{-2} and a thickness of 250 μm and CA/AM homogenous interconnections can easily be controlled through mechanical energy adjustments [58]. Overall, the influence of CAs on HMLE behavior is of great significance in the enhancement of performance. Based on this, Karkar et al. [59] employed three morphologically representative CAs including powdery CB, carbon nanofibers (CFs) and carbon nanoplatelets (CPs) to incorporate with high-loading LIB anode materials and found that "point-to-plane" electrical contact between AMs and CPs not only ensured electrical conductivity improvements in corresponding electrodes, but also contributed to electrode mechanical strength that is vital for long-term cycling, which these researchers attributed to the efficient cohesion and robust electron conductive structure of the CP framework.

Compared with powdered CAs, 1D fiber-like (containing CFs and CNTs) and 2D sheet-like carbon materials (such as graphene and MXene) possess high-aspect ratios that can more efficiently increase overall electronic conductivity in electrodes at specific volume fractions [57]. This is because CNTs possess enriched sp^2 hybridized C=C bonds and unique 1D cylindrical tubules of graphite sheets that can enhance electron transfer. High electrical conductivities are reflected by a low resistivity of 10^{-6} Ω cm^{-1} and maximum current densities for individual single-walled CNTs (SWCNTs) of 10^9–10^{10} A cm^{-2} as well as high conductivities of 10^6 S m^{-1} and over 10^5 S m^{-1} for SWCNTs and multi-walled CNTs (MWCNTs) respectively [10, 68]. Because of this, the serious inter-particle resistance of HMLEs can be improved by prolonging CNT-based conducting networks (Fig. 4b, c) to provide robust potentials in the fabrication of high conductivity HMLEs [69]. Planar structured graphene also exhibits high electrical conductivity (10^6 S m^{-1}) with high electron mobility in excess of 15000 cm^2 $(V\ s)^{-1}$ at room temperature and is therefore also a promising conductive agent for high performance HMLEs. Compared with acetylene black, graphene possesses a unique heavily crumpled structure with a large surface area that is beneficial for the absorption of nanostructured AMs and the accommodation of volume change, all of which can further contribute to excellent cycling stability [70]. Despite this, Yang et al. [71] reported that the rate performance of thick electrodes constructed using LFP/graphene decreased with increasing the graphene content and attributed this to the prolonged ion diffusion pathways as a result of large graphene layer

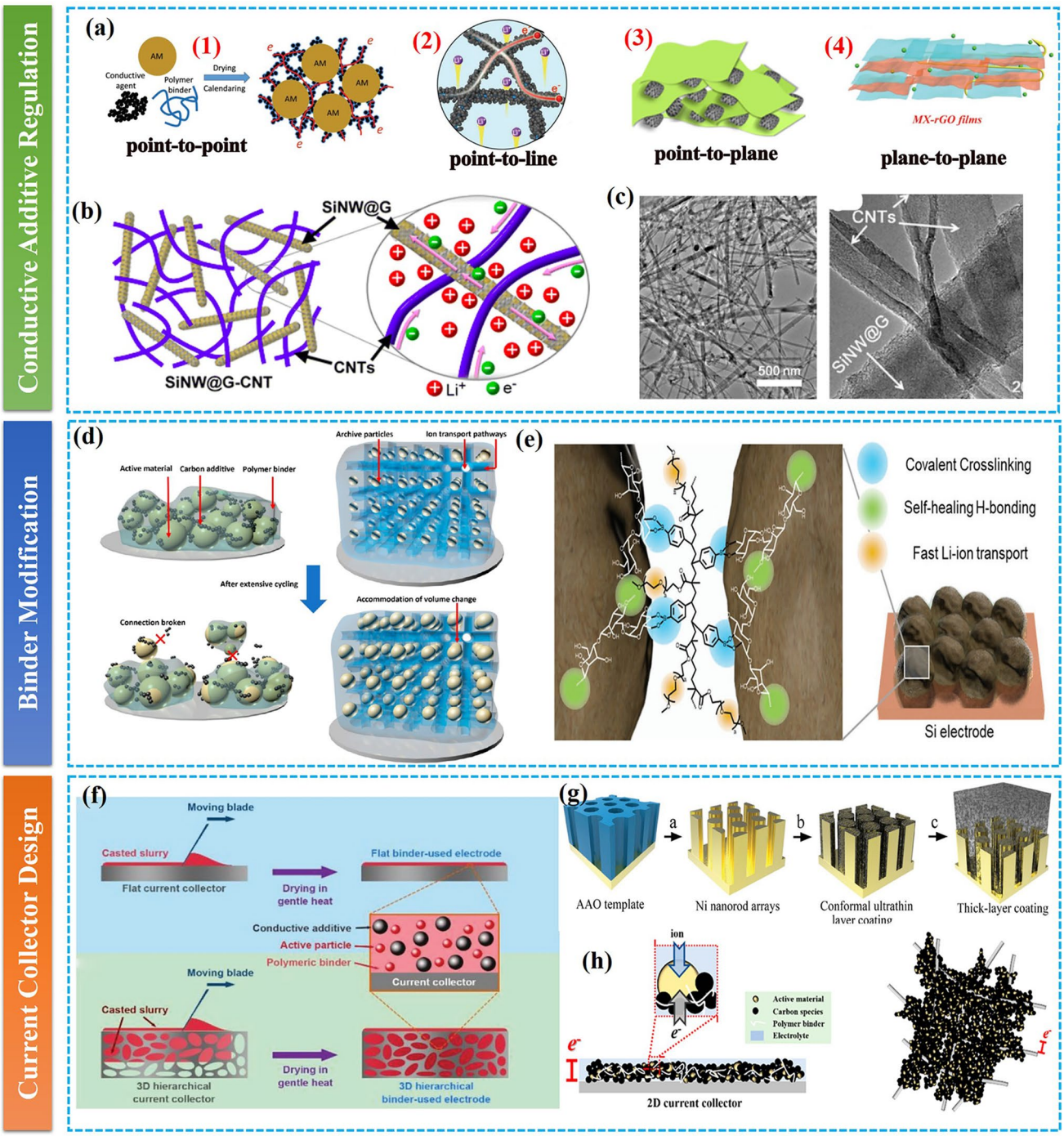

Fig. 4 **a** Different CA/AM electrical contact states: (1) "point-to-point" state. Reprinted with permission from Ref. [47]. Copyright © 2019, Wiley–VCH. (2) "Point-to-line" state. Reprinted with permission from Ref. [60]. Copyright © 2018, Wiley–VCH. (3) "Point-to-plane" state. Reprinted with permission from Ref. [61]. Copyright © 2018, American Chemical Society. (4) "Plane-to-plane" state, reproduced with permission Ref. [62], Copyright © 2018, Wiley–VCH. **b** Schematic illustration of the 3D the intertwined network of the Si@CNT anode, and **c** corresponding TEM images of Si@CNT anode. Reprinted with permission from Ref. [63]. Copyright © 2013, American Chemical Society. **d** Comparison of conventional and future battery electrodes using advanced binder systems for LIBs. Reprinted with permission from Ref. [64]. Copyright © 2017, American Chemical Society. **e** Schematic of a polysaccharide-based polymer binder in a Si electrode with strong interactions. Reprinted with permission from Ref. [65]. Copyright © 2020, Wiley–VCH. **f** Differences between planar current collectors and 3D porous current collectors. Reprinted with permission from Ref. [66]. Copyright © 2018, Wiley–VCH. **g** A 3D nickel nanoarray-based current collector enabling thick MnO_2 coating. Reprinted with permission from Ref. [45]. Copyright © 2015, Wiley–VCH. **h** Nonplanar HMLE structure with interwoven carbon fibers as the current collector. Reprinted with permission from Ref. [67]. Copyright © 2015, American Chemical Society

stacking. Because of this, the graphene content should be precisely controlled to balance the electronic conductivity and ionic diffusion efficiency of HMLEs. MXene can also be applied as a CA to obtain highly conductive electrodes such as an MXene bonded AC electrode with an electrical conductivity of 166 S cm^{-1} and an MXene bonded hard carbon electrode [61]. Continuous MXene scaffolds can also efficiently improve electrode stability due to the greatly enhanced ability to accommodate volume change [72]. Overall, CNTs, graphene, and MXene can allow for the effective construction of HMLEs with highly conductive network structures that can display compact and structurally stable properties due to superior structural features and strong interactions. Because of this, electrode conductivity can be improved through the addition of only small amounts of CNTs, graphene and MXene. Despite this, easy stacking and aggregation as well as complex fabrication processes, high production costs and low yields all limit further application in which scalable yet cost-effective manufacturing methods need to be developed for future application.

3.1.2 Binder Modification

Ideal electrodes that are structurally robust should possess optimized components that are rationally shaped, sized, dispersed, interconnected and wired to current collectors. In addition, these electrodes should be compatible with electrolytes to allow for low resistances. Here, polymer binders can be applied to enhance cohesion between slurry components and adhesion between electrode slurries and current collectors [64]. Advanced binder systems should also provide adequate mechanical adhesion, good compatibility and AM/CA surface modification to allow for stable SEI layers and accommodate volume variation to increase HMLE cycling performance (Fig. 4d). In addition, the even control of binder dispersion is vital for electron and ion transport through the formation of continuous internal pathways. And because binder distribution and migration during drying are major factors influencing electrode performance, pioneered research has been conducted to investigate the correlation between binder migration and electrode drying kinetics using characterization methods such as X-ray photoelectronic spectroscopy (XPS), energy-dispersive spectrometry (EDS), and Raman spectroscopy [73–75]. For example, the EDS mapping of a 400-μm-thick electrode under quick drying showed the existence of uneven binder fluctuation on the electrode surface and the AM/current collector interface as well as a concentration gradient across the thick electrode, which suggested the heterogeneous diffusion of the binder [74], indicating low drying rates are more conducive to ideal HMLEs. Binders also impart blocking effects on pore structures and corresponding distribution and migration can affect the porosity and tortuosity of electrodes. For example, Gasteiger et al. [76] systematically studied five types of polymer binders and their influence on thick electrode performances and found that different binders led to different tortuosity in correspond graphite anodes in which the rate performance of the electrodes decreased with increased tortuosity, suggesting that the reasonable control of binder types and distributions to optimize electrode porosity/tortuosity is essential in advanced HMLEs.

As a conventional polymer binder, PVDF has been widely used to fabricate HMLEs due to desirable binding capabilities and good electrochemical stability. However, PVDF cannot maintain electrode integrity during substantial AM volume expansion due to weak van der Waals forces between binders and AMs, leading to rapid capacity fading during cycling [77]. Alternatively, binders with abundant carboxylic groups possessing large molecular polarity such as carboxymethyl cellulose (CMC), poly(acrylic acid) (PAA), and alginate can mitigate this by enabling the uniform coverage and formation of stable SEI layers due to strong interfacial interactions between binders and AMs [78]. Regardless, optimal binders should be able to be scaled up to be compatible with electrode processing such as blade coating. For example, CMC binders with high viscosity can lead to inhomogeneous mixing and coating and the formation of cracks during electrode drying in thick dry films, which demonstrates unsuitability in HMLE construction [79]. To address this problem, Schappacher et al. [79] proposed a composite binder design that provided a targeted solution to fulfill the different requirements of HMLEs through the control of diverse binder advantages and synergistic effects, in which the designed composite binder was composed of CMC, PAA and polyethylene oxide (PEO) as well as a high solid content (65%) to enable crack-free thick electrodes. Here, the binder system was rationally designed based on careful considerations of crack-free and porous HMLE design requirements in which high viscosity CMC was partially replaced with low-viscosity PAA to ensure homogenous blade coating and moderate electrode porosity. PAA can also buffer mechanical stress to improve cycling performance whereas PEO is a commonly applied polymeric component in polymer electrolytes with high ionic conductivity [80, 81]. Carbon microfibers were also added to regulate the mechanical properties and pore size of the electrode during blade coating to contribute to the maintenance of crack-free strength.

Because conventional PVDF is an expensive fluorinated polymer and *N*-methyl pyrrolidone (NMP) is a toxic solvent, corresponding electrode formation is suboptimal. And although natural polysaccharide binders such as xanthan gum, guar gum, sodium alginate and catechol-conjugated polymers are promising choices due to the ease of production, these binders cannot accommodate substantial stress due to linear chain structures [65]. However, the cross-linking of natural binders using small molecules as crosslinkers

to precisely modulate bond strength can enable the delocalizing of concentrated stress on single chains and improve binder resilience. For example, Park et al. [65] engineered a novel polysaccharide binder to incorporate high-loading silicon nanoparticles over 2 mg cm^{-2} in which ion-conductive boronic crosslinkers spontaneously reacted with guar gum and polystyrene backbones to result in a high mechanical strength supramolecular network with well-balanced secondary interactions and covalent bonding (Fig. 4e). The regulation of intrinsic structural parameters in binders is another promising approach to enhance performance because multi-grafted block copolymer binders can be well defined through the altering of side chain lengths and tuning of grafting density degrees in which copolymer binders with optimized side chain lengths and adequate grafting densities can enhance the interconnections of electrode components to contribute to desirable electrode performances [82]. For example, Cao et al. [83] designed a structurally optimized copolymer binder that was able to interconnect with high-loading silicon over 2.5 mg cm^{-2}. Based on this, the deeper exploration of structure–performance relationships between polymer binders and electrochemical performance involving the control of binder morphology and structure is necessary for HMLEs.

Conducting polymers are promising multifunctional binder systems that can minimize inactive component occupation in electrode formulation because of their ability to act as both binders and CAs. Conducting polymers can also be modified to improve electronic conductivity, mechanical adhesion and electrolyte uptake through the introduction of various functional groups and the design of multidimensional nanostructures [64]. For example, formic acid was introduced to the in situ secondary doping of PEDOT:PSS to further improve electrical conductivity up to 4.2 S cm^{-1} and produce high-performance high-silicon-content electrodes (80%) [44]. Despite this, conducting polymer binders suffer from complex preparation methods and high costs.

3.1.3 Current Collector Design

Conventional current collectors generally involve 2D planar shaped materials such as copper foil, aluminum foil and carbon foil. However, these 2D current collectors are unsatisfactory for HMLEs due to several reasons, including: (1) high planar current collector densities that can lead to low effective material mass ratios in which AM occupation in electrodes is only 22.94% and 36.27% for 2D Cu and Al current collectors, respectively, but more than 50% for current collector colonization [84]; (2) poor resistance to electrochemical corrosion during repeated cycling; (3) weak cohesion between current collectors and AMs as well as repeated volume change (ion intercalation/extraction) during cycling, which will lead to the cracking, dropout and exfoliation of AMs in HMLEs [18, 85]; and (4) limited charge transfer to AMs in HMLEs leading to the underutilization of active sites [86]. Alternatively, porous 3D current collectors (Fig. 4f) can not only offer robust 3D scaffolds to reinforce AM loading, but also act as 3D conducting networks for effective charge delivery throughout thick electrodes [66]. In addition, 3D current collectors with high surface area, excellent conductance and outstanding physical–chemical stability can significantly increase AM mass loading to further promote utilization efficiency in which 3D porous Al or Cu current collectors are typical substitutes for conventional 2D ones [12]. Shear testing has also indicated that electrodes based on 3D porous current collectors can exhibit better mechanical responses than conventional planar current collectors due to improvements in AM/current collector interconnections. In addition, the smooth electron transfer and rapid ion transport of 3D porous electrodes can allow for thick electrodes with good rate capability. Different cell sizes of 3D current collectors can also influence electrode performance. For example, Joo et al. [87] prepared 3D nickel foams 450, 800, and 1200 μm in cell size to establish 300–600 μm thick HMLEs in a range of 30–60 mg cm^{-2} and reported that although the electrode using the 1200 μm cell sized nickel foam demonstrated the highest areal capacity, corresponding rate performance was the lowest due to low charge transport in the thick electrode. These researchers further suggested based on the combined consideration of high capacity and moderate rate capability, suitable nickel foam cell sizes should be in the range of 450–800 μm. 3D nanostructured current collectors (3D-NCC) with various dimensional units such as nanowires, nanotubes, nanorods, nanosheets and nanoflakes are also ideal alternatives to reduce interfacial resistance between electroactive materials and current collectors due to enlarged interfacial contact spots as a result of the high surface area of 3D-NCCs [88]. Because of this, the electrochemical performance of thick-film-coated electrodes can be improved due to efficient charge transport and enhanced active site utilization. For example, Liu et al. [44] prepared a 3D nickel current collector with vertical nanoarrays using Anodic Aluminum Oxide (AAO) template methods (Fig. 4g) and reported that due to the significantly reduced interfacial resistance of the AM/current collector as a result of enlarged interfacial contact, the 3D nickel current collector allowed for a high-loading electrode with a nearly 3-μm-thick MnO_2 coating that possessed excellent rate capability.

Despite the large mass ratios of metal current collectors in electrode components, performances still fail to meet practical HMLE requirements. Here, the development of ultralight current collectors with high mechanical strength is promising. For example, Fang et al. [84] obtained an ultralight, highly conductive and porous carbon nanofiber-based 3D carbon current collector (3D-CCC) through the one-pot

carbonization of commercial biomass cotton and reported that this 3D-CCC can allow for AM loadings of over 50% to enable 300 μm thick electrodes, resulting in significantly enhanced areal capacities and rate performances as compared with electrodes obtained from conventional 2D current collectors. This is because the porous carbon structure can facilitate ionic diffusion and effectively alleviate electrode volume expansion to contribute to long-term cycling performance. In addition, the 3D nanofiber interwoven structure is a suitable scaffold to build nonplanar electrode structures with robust electronic/ionic contact. Nonplanar electrodes can also overcome limited electron transport as compared with traditional planar current collectors to provide efficient ion transfer in thick electrodes (Fig. 4h). For example, Zheng et al. [67] used commercial carbon cloth as a current scaffold and electron transport medium coupling with $LiCoO_2$ (LCO) to obtain an 800-μm-thick composite electrode that possessed an ultrahigh mass loading of 213 mg cm^{-2}. Based on this, ultralight porous carbon current collectors with improved conductivity, multiscale pore structures, high elasticity, compressibility, and stretch-ability are promising research topics.

3.2 Regulation of AM Properties

3.2.1 Improving the Electrical Conductivity of AMs

Heteroatoms Doping The timely transport of electrons and ions as mass loadings increase is vital to ensure the rapid delivery of charge in high capacity or high rate HMLEs

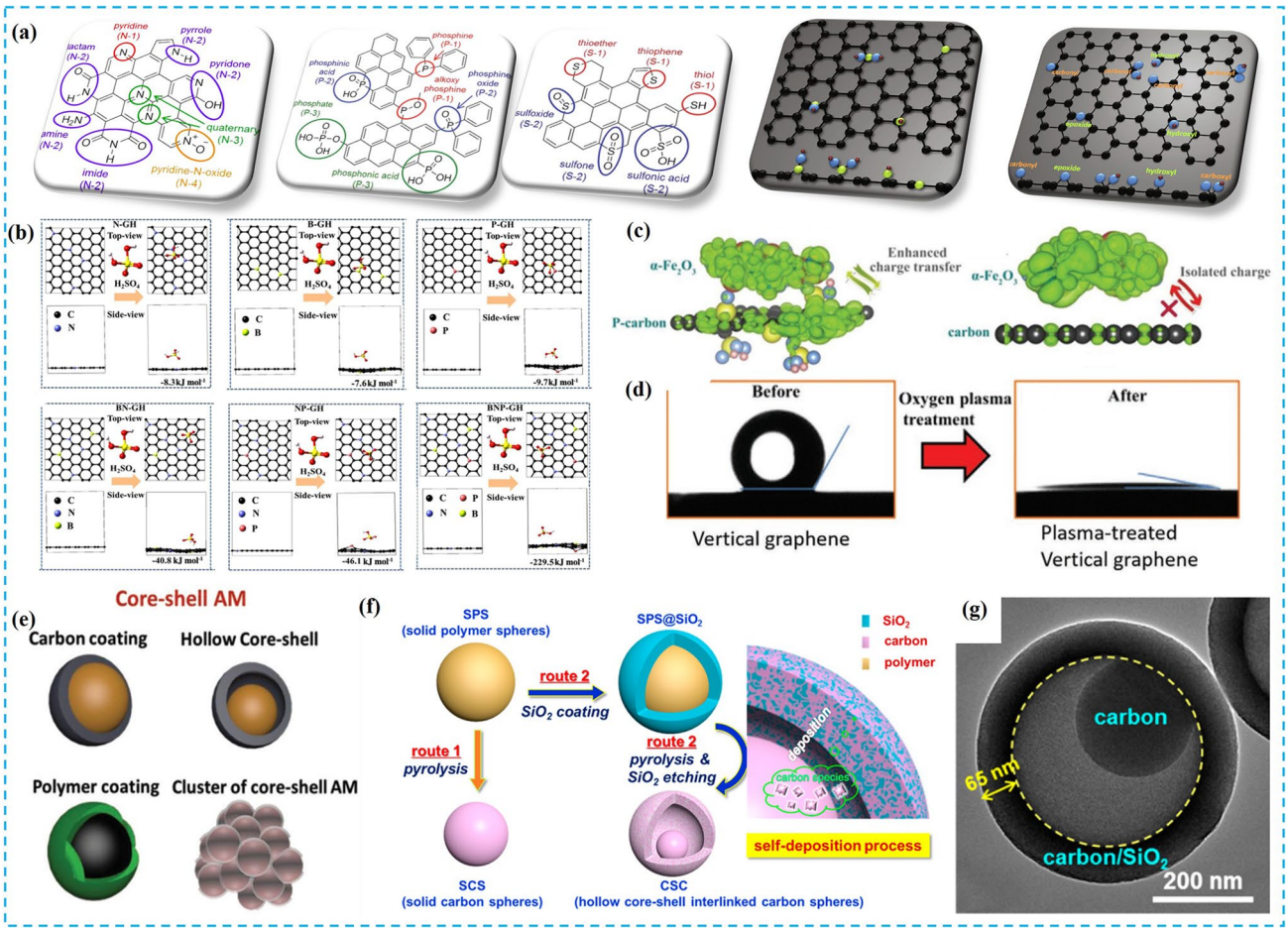

Fig. 5 **a** Schematics of possible N, P, S, B, and O configurations in carbon matrixes. N, P, O configurations are reprinted with permission from Ref. [46]. Copyright © 2017, American Chemical Society. B and O functionalization are reprinted with permission from Ref. [102]. Copyright © 2020, Elsevier. **b** H_2SO_4 adsorption energy on single and multi-heteroatom-doped graphene, reprinted with permission from Ref. [93]. Copyright © 2018, Elsevier. **c** Charge density distributions of α-Fe_2O_3/carbon composites with and without P-doping. Reprinted with permission from Ref. [99]. Copyright © 2019, Elsevier. **d** Water contact angles of vertical graphene before and after O-plasma treatment. Reprinted with permission from Ref. [100]. Copyright © 2018, Elsevier. **e** Core–shell structured AMs. Reprinted with permission from Ref. [47]. Copyright © 2019, Wiley–VCH. **f** Fabrication process of hollow core–shell interlinked carbon spheres and **g** corresponding SEM image. Reprinted with permission from Ref. [103]. Copyright © 2015, American Chemical Society

[12]. Because of this, the electrical conductivity of porous electrode materials is a decisive factor in high performance HMLEs. For example, although porous carbon (PC) is a widely used material in EESSs due to high specific surface areas (SSAs), stable physical–chemical properties and low production costs, PCs with ultrahigh SSAs generally exhibit undesirable electrical conductivity, which is detrimental to HMLEs [43]. To compensate for the poor performance of PCs, heteroatoms doping is considered to be an effective route to regulate corresponding electronic states and facilitate electron transfer [89], in which single atom doping (N, S, P, B, O) and multi-atom doping (N/S, N/P, N/B, N/P/S, etc.) are common methods to tailor the electronic conductivity of PCs (Fig. 5a) [90–92]. Here, theoretical calculations based on density functional theory (DFT) are key indicators that can be used to understand the effects of foreign element incorporation on carbon material electronic property. For example, comparisons of H_2SO_4 adsorption energy for carbon materials with single doping (N-, B-, P-), co-doping (N/B, N/P) and ternary doping (N/B/P) indicated that multi-atom doping can contribute to higher adsorption energy and superior electrochemical performances (Fig. 5b) [93]. In general, the introduction of heteroatoms with different electronegativities from carbon can induce the charge density redistribution of carbon materials and lead to low band gap energy and rapid electron transfer on graphene basal planes [94–98]. Heteroatoms possessing relatively large atomic sizes can further distort carbon structures and enlarge interlayer spacing to break balanced spin density and expose more electroactive defects [89].

Interactions between metal-based active centers and carbon supports can also improve the electrical conductance of electrodes. For example, charge density distributions clearly indicate enhanced charge transfer efficiency between α-Fe_2O_3 and P-doped carbon but isolated interconnections in un-doped carbon, confirming the regulation of electronic configuration through P-doping (Fig. 5c) [99]. In fact, heteroatom-doping can affect many properties in carbon materials other than electrical conductivity, including wettability (Fig. 5d), interlayer spacing (especially for hard carbons) and porosity [100]. And therefore, the rational design of heteroatom-doping configurations is useful in the regulation of carbon surface states to improve interfacial electronic/ionic contact between electrodes and electrolytes and contribute to advanced HMLEs. However, heteroatom doping levels must be controlled at reasonable levels as well because excessive doping can negatively influence the electronic structure of carbon. In the case of carbon nitride (C_3N_4, a typical N-doped carbon with ultrahigh N contents up to 57% atomic N but poor electrical conductivity of nearly 10^{-5} S cm^{-1}), for example, Pender et al. [101] found that highly defective C_3N_4 (a high N content) endowed much higher Li^+ storage than highly graphitized C_3N_4 (a low N content) in which the defects contributed to increased Li^+ adsorption sites and reversible faradaic Li^+ reactions with N atoms. Based on this, suitable doping and rational tuning are both key methods to improve the performance of heteroatom-doped carbon electrodes.

Core–Shell Design The design of core–shell structures with AM cores and CA shells can effectively ensure stable electronic contact between electroactive materials and conductive agents. Based on this, many core–shell designs (Fig. 5e) including carbon coatings, conducting polymer coatings, hollow core–shell morphology and core–shell AM clusters have been proposed [47]. And among these, carbon coatings are a more promising approach because carbon layers can not only lower electron migration distance, but also protect core AMs from serious volume expansion. And although varying carbon morphology including 1D carbon nanofibers, 2D carbon nanosheets and 3D graphene networks has been employed to design nanostructured core–shell AMs, carbon coatings inevitably introduce additional challenges including high SSA and low tap density for core–shell AMs that can lead to side reactions and low volumetric performances, respectively [104]. Here, the design of rational structures involves the complete encapsulation of secondary AM particles with carbon frameworks to form micronized particles with highly interconnected structures (Fig. 5f, g) such as a pomegranate-inspired Si/C nanostructure and hollow core–shell interlinked carbon spheres that cannot only prevent severe side reactions and large SEI formation on individual nanoparticles, but also improve electrode packing density [103, 105].

In terms of fabrication, one widely used strategy involves the pretreatment of AM precursors with additional carbon precursors through co-annealing under high temperature to in situ form ultrathin carbon coating layers that can homogenously and flexibly match with the morphology and microstructure of the AM. Another promising strategy involves the simple, cost-effective and direct carbonization of metal–organic molecules to in situ form core–shell AMs. Here, intrinsically coordinated compounds can possess strong chelating effects between metal centers and surrounding organic frameworks to enable the uniform and stable embedding of metal nanoparticles in carbon frameworks. Typical organic compounds also possess strong chelating effects with metal ions to allow for the fabrication of core–shell AMs. Moreover, 3D hydrogel foam derived from organic components is another promising precursor to obtain the homogeneous dispersion of active nanoparticles in 3D conductive matrixes [106], in which the interconnected hierarchically porous structure and continuous conductive pathways are conducive to electronic/ionic transport and allow for HMLEs with high areal capacities and excellent rate capabilities. Typical organic molecules such as polyvinyl pyrrolidone (PVP), dopamine, citric acid and chitosan

can further be used as complexing agents to anchor metal ions for further processing into ultrathin carbon nanosheets incorporated with ultrafine metal nanoparticles. Synthesis processes such as chemical vapor deposition (CVD), atomic layer deposition (ALD), 3D printing and other advanced techniques can also be used to obtain core–shell nanostructures. However, complex procedures, unique equipment requirements and high costs impede easy application. In addition, precursor costs need to be reduced to meet commercial demands.

3.2.2 Improving the Ionic Diffusion Efficiency of Porous Electrodes

Nanostructured AM Design Nanostructured AMs are promising in advanced HMLEs due to unique properties derived from confined dimensional features and combined bulk and surface properties that can reduce ionic diffusion pathways as a result of the synergetic effects of nanoscaled morphology and porous structure [11, 115, 116]. Here, hierarchical porous AM structures involve two or more porous structures that include micropores with pore widths smaller than 2 nm, mesopores with pore widths ranging from 2 to 50 nm and

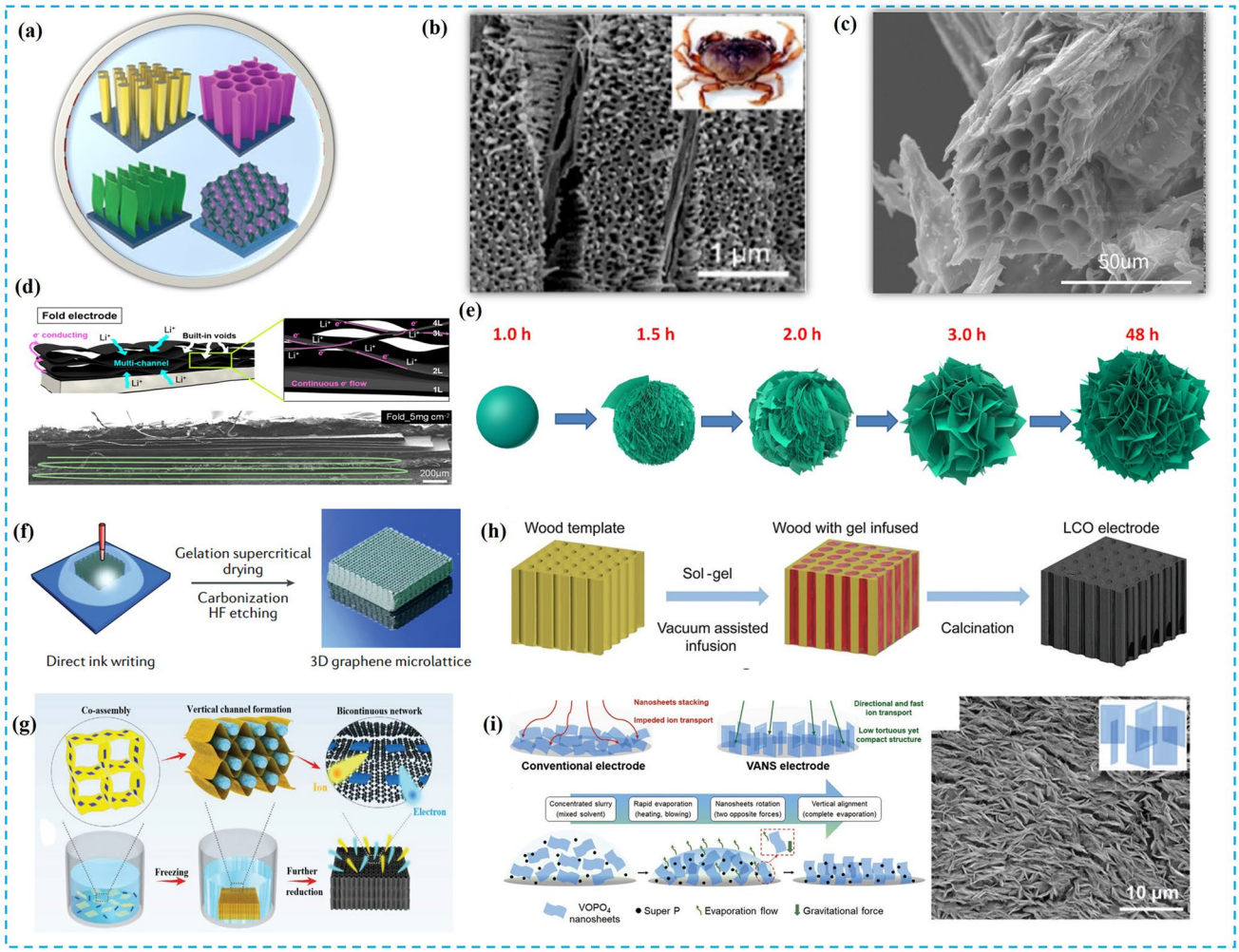

Fig. 6 **a** Illustration of different 3D nanostructured electrodes. Reprinted with permission from Ref. [88]. Copyright © 2020, Wiley–VCH. **b**, **c** Biomass derived 3D hierarchical porous structures, including (**b**) crab shells. Reprinted with permission from Ref. [107]. Copyright © 2013, American Chemical Society. **c** Wood. Reprinted with permission from Ref. [108]. Copyright © 2019, Elsevier. **d** Illustration of a folded graphene electrode with abundant ionic transport channels. Reprinted with permission from Ref. [109]. Copyright © 2018, American Chemical Society. **e** The formation process of CaV_4O_9 micro-flowers. Reprinted with permission from Ref. [110]. Copyright © 2018, Elsevier. **f** The 3D printing of a 3D graphene microlattice. Reprinted with permission from Ref. [111, 112]. Copyright © 2016, The Royal Society of Chemistry. **g** The ice-template-assisted fabrication of a vertical-channeled thick electrode. Reprinted with permission from Ref. [113]. Copyright © 2019, Wiley–VCH. **h** Wood-template for a thick LCO cathode. Reprinted with permission from Ref. [17]. Copyright © 2019, Wiley–VCH. **i** Illustration of the construction of vertical aligned $VOPO_4$ electrodes and the corresponding SEM image. Reprinted with permission from Ref. [114]. Copyright © 2015, Wiley–VCH

macropores with pore widths higher than 50 nm in which micropores can generally act as active sites for ion adsorption whereas mesopores/macropores can act as electrolyte buffer regions to lower mass transport distance, resulting in high rate capability HMLEs [48]. Corresponding fabrication methods of hierarchical porous AMs involve hard and soft template methods (such as the silica template, the salt template, the metal oxide template, the ice template, the organic polymer template and the surfactant template), double-template methods, molecular unit self-assembly methods and template-free methods [12, 48, 117]. Alternatively, 3D hierarchical electrodes (Fig. 6a) with continuous conductive networks and open porous structures can significantly enhance electron and ion transport efficiency and are therefore also ideal structures for advanced HMLEs [12, 118]. However, 3D hierarchical electrodes possess low packing densities due to the presence of many dead macropores and void spacing that can lead to low volumetric battery performance. To address this, a balance between material density, porosity and electrode thickness through dedicated strategies is necessary. In terms of cost-effective starting materials for hierarchical porous electrodes, biomass precursors and corresponding derivates are good choices due to their sustainability, abundance and environmental friendliness. In particular, some biomass-derived AMs can inherent the natural pore/morphology properties of biomass precursors without the need for templates, thus allowing for facile and large-scale production processes. Natural biomass materials can also possess unique 3D microstructures such as interconnected channels over multiple length scales (Fig. 6b, c) to provide natural 3D hierarchical conductive scaffolds and templates to fabricate HMLEs [107, 108, 119].

The tuning of nano-dimensional morphology is also a viable strategy to engineer the mass diffusion properties of AMs. For example, graphene quantum dots (GQDs) are 0D graphene derivatives with ultrafine lamellar sizes (< 10 nm) and a π-conjugated core structure as well as enriched edge sites for charge storage that can couple with conductive materials such as graphene, CNTs, activated carbon, and conducting polymers to effectively fabricate interconnected porous HMLEs and provide abundant active sites and sufficient ion transport pathways [120]. Alternatively, 1D CNTs and 2D graphene both suffer from serious restacking due to strong interlayer interactions that can lead to undesirable electrochemical performances in corresponding HMLEs. In addition, the electrochemical performance of 2D graphene nanosheets without ion migration channels under high mass loading is generally hindered. However, Wang et al. [109] reported that folded graphene structures (Fig. 6d) did not possess these issues because folded graphene electrodes possess abundant multi-channels and built-in voids between folded graphene layers that allowed for abundant and short ion diffusion pathways. The control of the pore structure of graphene nanosheets can also effectively enable mass transfer between graphene layers in which Su et al. [121] reported that nano-copper-assisted annealing followed by the removal of nano-copper led to the uniform distribution of small hierarchical in-plane pores within graphene layers as well as sufficient ionic diffusion regions. Multi-dimensional AM structures constructed by using 2D/1D/0D microstructures are also promising due to the combination of multiple advantages. For example, Mai et al. [110] were able to construct HMLEs based on 3D compact CaV_4O_9 micro-flowers assembled by using 2D nanosheets (Fig. 6e) that ensured rapid electron/ion transport as induced by ultrathin nanosheets and pore-enriched 3D networks with interconnected channels for electrode–electrolyte contact. Despite this, future research should focus on the understanding of structure-performance relationships in these complex nanostructured AMs.

Lower Tortuosity Design Because low-tortuosity structures can contribute to enhanced ion transport efficiency in thick electrodes, effective strategies have been proposed to engineer low-tortuosity electrode structures. For example, extrusion-based 3D printing (Fig. 6f) is an emerging and reliable technology that can accurately and efficiently construct complex 3D structures for advanced electrodes [122]. Extrusion-based 3D printing is also highly versatile and flexible in the rational design of HMLEs due to the ability to fine-tune electrode thicknesses, ordered internal pore structures, geometric shapes and functional composition [123]. One key issue for 3D printing is the preparation of suitable printing inks that possess favorable shear-thinning and good viscoelastic properties however, which prevents the direct printing of highly robust 3D structures without collapse. Because of this, the final electrochemical performance of corresponding HMLEs is related to many factors such as the printing speed, the printing shape, the ink precursor intrinsic rheological property and the electrode porosity in which the search for optimal ink materials and matched printing parameters is vital in 3D-printed HMLEs [122]. Here, flexible carbon materials featuring nanostructures and changeable shapes that can allow for facile 3D printing include materials such as graphene oxide (GO), CNTs and carbon black whereas most reported AMs for energy-related applications involve inorganic materials that require additional additives to incorporate, which hinder resulting electrochemical performance and require the development of additive-free and highly stable AMs for 3D printing. In addition, more attention needs to be paid to the manufacturing size and time of 3D printing methods to meet the demands of large-scale and inexpensive HMLE production.

Alternatively, vertically aligned nanostructures (VANs) can allow for the precise regulation of nanosized and ordered porous AM structures to obtain low-tortuosity electrodes [16]. Based on this, extensive research has been conducted in the past decades in the search for rational fabrication

methods to obtain VAN-based AMs, which include magnetically assisted [124], template-assisted and directly oriented growth methods. And because enhanced ion diffusion properties can contribute to the thickness-independent performance of HMLEs, the structurally templated formation of oriented pores/channels is an appealing method to synthesis VAN electrodes. Ice-template-assisted freeze drying is another widely used method to design vertical-channeled nanostructures through the assembly of small molecules (Fig. 6g) [125]. Alternatively, natural wood with its inherent microstructure composed of numerous ordered and vertically aligned microchannels is also a fascinating biotemplate to engineer VAN electrodes in which continuous networks with numerous vertical channels and wide pores as inherited from wood (Fig. 6h) can enable rapid ion diffusion [17]. Despite this, most template-guided methods generally generate large pores in electrodes to result in numerous "death pores" without charge storage contribution to result in low volumetric performance. To address this, pore structures need to be rationally adjusted and inactive porosity needs to be reduced through the use of controllable templates such as easily removable salt templates that are uniform and small in size. Based on this, the use of controllable templates combined with advanced printing techniques can become promising in the fine regulation of porosity in low-tortuosity HMLEs.

As for template-free approaches, these can be used to directly form VAN electrodes for the scalable production of low-touristy HMLEs. For example, Yu et al. [114] reported that the rational control of solvent evaporation rates in conventional slurry drying procedures can induce dense film electrodes with VAN nanosheets and that the key to the successful synthesis of orientation ordered composites is the rapid evaporation of mixed solvents in which nanosheets can experience rotating clockwise processes as induced by opposite forces (downward gravitational force

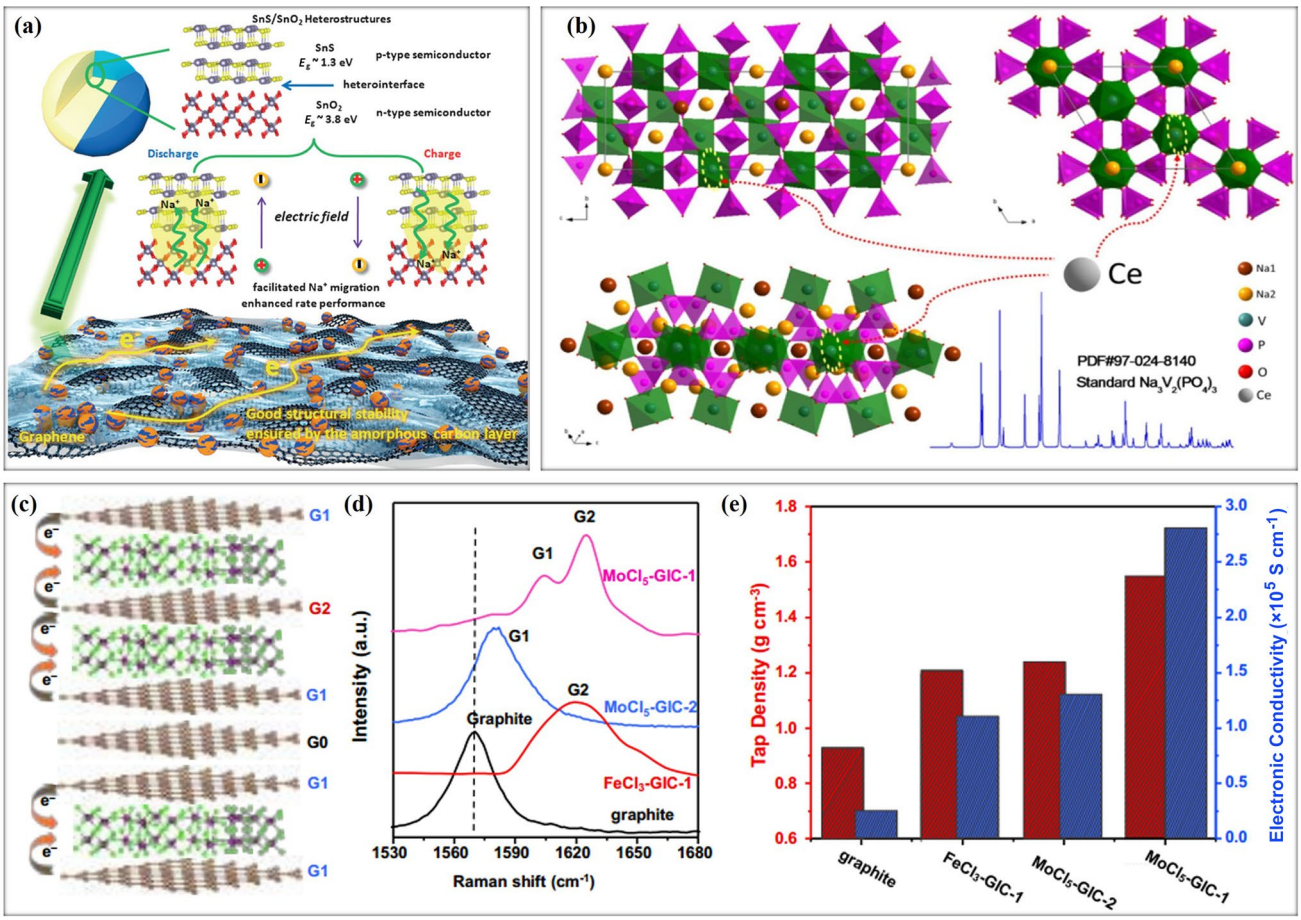

Fig. 7 **a** Schematic of the induced BIEF effects of SnS/SnO_2 heterostructures showing facilitated Na^+ migration and enhanced rate performance. Reprinted with permission from Ref. [128]. Copyright © 2016, Wiley–VCH. **b** Ce^{3+} partial substitution for V in NVP/C complex to design heterostructured AMs. Reprinted with permission from Ref. [129]. Copyright © 2017, Elsevier. **c** Schematic structures of enlarged interlayer distances after $MoCl_5$ intercalation. **d** Enlarged Raman G-band regions. **d** Tap density and electrical conductivity of the samples. **c**–**e** Reprinted with permission from Ref. [54]. Copyright © 2020, The Royal Society of Chemistry

and upward force) until vertically aligned (Fig. 6i). Park et al. [126] also used physical vapor deposition to fabricate vertically aligned monolithic electrodes involving 40-μm-thick WS_2/C arrays on Al foil. Another promising template-free method involves phase inversion that can be applied to prepare hierarchical porous membranes for water cleaning treatment processes but is less useful for energy storage applications. However, Yu et al. [127] recently pioneered this strategy to fabricate carbon electrodes with hierarchically and near vertically aligned pore structures in which the resulting hierarchical macroporous structure allowed a corresponding carbon electrode to become an ideal sulfur host with rapid ion/electrolyte transport and high sulfur loading capability.

3.2.3 Reduction in Ionic Solid-Phase Diffusion Resistance

One key obstacle for metal ion batteries involves low ionic solid-phase migration efficiency into crystal structures during ion insertion/extraction, which will lead to poor rate capability and low energy storage capacity. Here, heterostructured materials obtained through the coupling of nanocrystals with different band gaps to generate built-in electric field (BIEF) effects near heterointerfaces due to charge redistribution can boost interfacial charge transport and surface reaction kinetics [130]. Based on this, various heterostructured materials have been explored, such as Bi_2S_3-Bi_2O_3 nanosheets [131], SnS/SnO_2 [128], Bi_2MoO_6 nanosheets [130], Ni^{2+}-doped Co_3O_4 nanocrystals with generated Co vacancies [132] and ternary $CuGeO_3$ nanosheets with modulated oxygen vacancies [53], most of which suggest that BIEF effects can improve ion diffusion and electron conduction (Fig. 7a) to result in desired specific capacity, rate performance and cycling stability. Alternatively, oxygen vacancy (*V*o) engineering through the removal of oxygen in perfect crystal structures is considered to be an effective method to generate BIEF effects [133], in which DFT calculations suggest that abundant Vo sites can significantly reduce Li^+ diffusion activation energy to lead to rapid Li^+ migration [133]. Ion-doping is another promising approach to enhance bulk phase electronic conductivity and ion mobility in which Zhang et al. [129] partially substituted V with Ce^{3+} in a $Na_3V_2(PO_4)_3$/C complex (Fig. 7b) and reported that the resulting Ce^{3+}-doped sample possessed a Na ion diffusion coefficient of 4.903×10^{-11} cm^2 s^{-1} that was higher than that of the pristine NVP/C electrode with 1.719×10^{-11} cm^2 s^{-1}, which indicated enhanced Na ion migration efficiency. Moreover, interlayer spacing modulation is an ideal strategy to design open structured AMs for efficient ionic diffusion (Fig. 7c, d), whereas the insertion of guest ions or small molecules is a common method to expand the interlayer spacing of layered compounds [134]. For example, Liu et al. [54] used molybdenum pentachloride ($MoCl_5$)-graphite intercalation compounds (GICs) with high binding energy as HMLEs and reported that intercalated $MoCl_5$ was tightly grafted between adjacent graphite layers to result in a high electrical conductivity of 2.8×10^5 S cm^{-1} (Fig. 7e) as well as rapid ion diffusion due to the open structures as a result of the rationally expanded interlayer distances. These researchers also reported that the tuning of interlayer spacing can enhance active site utilization on inner graphene layers.

3.3 Integrated Electrode Design

Although HMLE structural engineering is a feasible method to improve battery energy density, advanced HMLEs are not easily attained through conventional blade coating methods due to pore blocking, enlarged internal resistance and poor interfacial stability as a result of polymer binders as well as unstable electronic contact between AMs and current collectors. Alternatively, binder-free and current-collector-free HMLE configurations, referred to as integrated electrode designs, can guarantee improved energy density in overall devices through the maximization of AM packing and the reduction of inactive components, allowing integrated electrodes to possess robust mechanical strength for self-support, stable chemical properties for long time cycling, abundant multiscale pores for efficient ion diffusion and interconnected conductive frameworks for electron transport. Because of this, numerous integrated electrodes have been developed in the past decades and can be divided into two aspects, including (1) 3D conductive scaffolds as electroactive components or supports to load AMs and (2) composite network structures through the use of robust and conductive building blocks.

3.3.1 3D Conductive Scaffold Electrodes

3D conductive scaffold electrode (3D-CSE) designs can provide multifunctional platforms for the engineering of HMLEs with complex structures based on diverse AMs such as carbon foam, carbon sponge, monolithic carbon, nanofiber interweaved carbon cloth/fiber, ultralight and porous carbon aerogels and other 3D carbon frameworks. For example, carbon cloth (CC) as a flexible carbon support containing interwoven 1D microfibers has been widely used to fabricate flexible and bendable electrodes due to intrinsically excellent electrical conductivity, porous structure, good corrosion resistance and highly integrated strength [141], in which many controllable methods have been applied to load AMs onto CC surfaces, such as hydrothermal methods, chemical vapor deposition, electrodeposition and dip-coating methods (Fig. 8a). Despite this, the surface attachment of AMs on CC leads to the insufficient utilization of CC and restricted mass loading whereas the utilization of

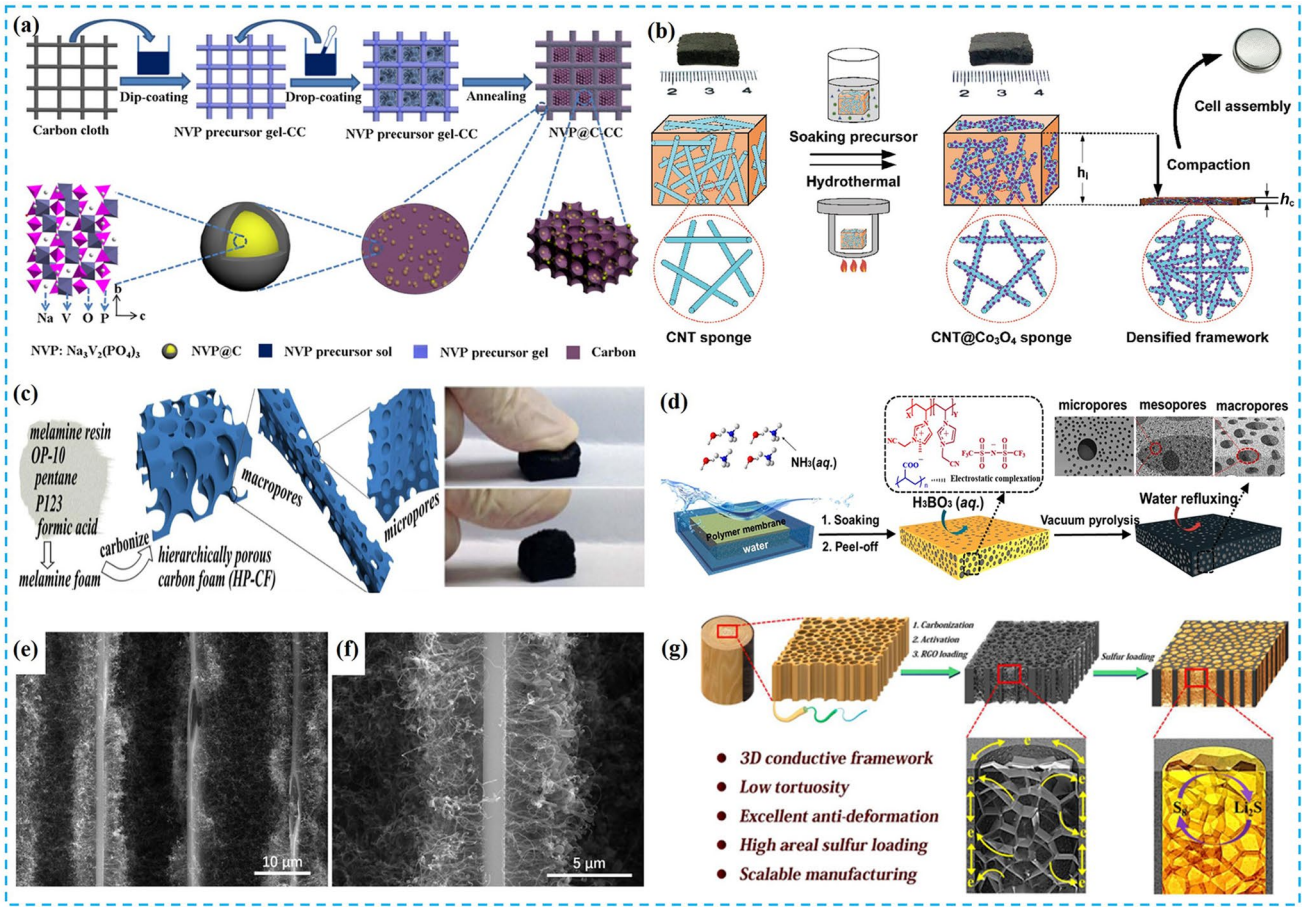

Fig. 8 **a** Schematic of the synthesis of HMLEs by coating $Na_3V_2(PO_4)_3$/C onto carbon cloth. Reprinted with permission from Ref. [135]. Copyright © 2017, Elsevier. **b** CNT sponge as a conductive scaffold loaded with Co_3O_4 that can be densified. Reprinted with permission from Ref. [136]. Copyright © 2018, Wiley–VCH. **c** Preparation process of melamine resin-derived compressible carbon foam. Reprinted with permission from Ref. [137]. Copyright © 2016, Elsevier. **d** Synthesis of the poly(ionic liquid)-derived nanoporous carbon monolith through phase separation. Reprinted with permission from Ref. [138]. Copyright © 2019, American Chemical Society. **e**, **f** Growing CNTs into wood-derived carbon. Reprinted with permission from Ref. [139]. Copyright © 2019, Elsevier. **g** Filling graphene into wood carbon as sulfur hosts for Li–S batteries. Reprinted with permission from Ref. [140]. Copyright © 2017, American Chemical Society

gaps and void spaces between CC fibers to accommodate increased AM loading can improve the overall mass loading of electrodes [135]. For example, the incorporation of additional components into CC voids to bridge surrounding gaps can improve CC electrode mass loading to enable well-defined 3D porous conductive networks to fulfill gaps and void spaces among fibers. The introduction of multilevel pores into carbon fiber backbones can also improve utilization efficiency because these structures can not only provide more surface area to storage active components, but also ensure electrolyte penetration within thick active layers [142]. Despite this, the internal mechanical strength of corresponding carbon fibers will inevitably be reduced under highly porous conditions and therefore, a balance between structural porosity and mechanical stability needs to be carefully optimized.

CNT sponge is another promising conductive scaffold that possesses large inner spacing to accommodate high AM loading as well as structural integrity with high compression tolerance to enable densified thick electrodes with high packing density (Fig. 8b). Here, the use of conductive scaffolds with highly deformable features (elastic, compressible, bendable, stretchable, etc.) to construct hybrid structures can provide novel opportunities to engineer advanced HMLEs with dense but porous structures that can be extended to graphene sponge, graphene foam and carbon aerogels.

Polymers can also be directly processed into carbon monoliths as a facile, scalable and sustainable method to fabricate integrated HMLEs in which melamine foam (MF) as a typical commercial polymer foam possesses a highly elastic and interconnected network structure. Based on this, MF obtained monolithic carbon materials

possess ultralow densities of 5 mg cm^{-3} that are comparable to CNT sponge (5–10 mg cm^{-3}) and graphene foam (~ 5 mg cm^{-3}), demonstrating potential as an ultralight carbon support for hybrid electrodes [143]. In addition, these MF polymers possess combined advantages including macroporous structures favorable for rapid mass diffusion and MF frameworks with nitrogen-enriched components that can induce abundant active defects to enhance energy storage capacity. Unfortunately, the presence of ultra-large and inactive pores in MF backbones can also lead to low volumetric performance. Alternatively, polymers assembled through molecular precursors can provide pore/composition tunable routes to engineer monolithic carbon electrodes because of maneuverable synthesis processes through the dedicated selection of appropriate molecules and rational reaction mechanisms. For example, He et al. [144] fabricated a monolithic carbon electrode based on chemically cross-linked molecules including lignin as the central crosslinking sites, a copolymer template (Pluronic P123) as the mesopore-forming agent and a hard template (KIT6) as the macropore-forming agent. Wong et al. [137] also conducted molecular engineering based on strong cross-linking interactions between melamine and paraformaldehyde to produce a hierarchical N-doped carbon electrode (H-NC) using P123 as a micropore forming agent and pentane as a macropore forming agent (Fig. 8c). Poly(ionic liquid) (PIL) membrane-derived nanoporous carbon materials have also attracted intensive attention recently for application [145, 146]. PIL polymers are composed of two polymerized IL molecules through electrostatic crosslinking in which Zhao et al. [138] used phase separation to obtain a N/B-doped porous carbon monolith based on PIL (Fig. 8d) that possessed an interconnected hierarchical pore structure. Despite this, these PIL-derived carbon membranes remain in early investigation stages and extended application in batteries requires further exploration.

In recent years, natural wood has further been presented as a promising platform to engineer integrated HMLEs due to a naturally hierarchical porous structure, low tortuosity, aligned channels and moderate mechanical strength [21]. In addition, the unique microstructure of wood-derived carbon materials allowed for the investigation of structure-performance relationships between mass loading and parallel/vertical aligned electrode structures to clearly demonstrate the better areal capacity of VAN electrodes as compared with parallel electrodes [147]. Nevertheless, the existence of inactive void spaces in wood carbon structures will lead to low electrode utilization efficiency and poor volumetric performance. To address this, Chen et al. [139] incorporated CNTs into CW inner walls through nickel assisted CVD to enhance SSAs and electron/ion transfer (Fig. 8e, f). Hu et al. [140] also directly filled rGO into an ultrathick wood carbon framework to obtain a stable 3D framework host and achieved high sulfur loading (Fig. 8g). Overall, wood-derived ultrathick and integrated electrodes are efficient and cost-effective candidates for commercial batteries; however, the intrinsically rigid structure and permanent composition of wood carbon result in difficult structural regulation or functionalization. In addition, the physical–chemical properties of wood are greatly influenced by factors such as climate, soil condition and tree types and require more in-depth research.

3.3.2 Integrated Composite Network-Based Electrodes

Although 3D-CSE designs can promote the development of HMLEs, most are rigid structures that are unsuitable in flexible electronics applications. Alternatively, integrated composite network-based electrodes (ICNEs) fabricated from intrinsically flexible, bendable and stretchable components possess great potential for application in flexible and wearable devices. In terms of synthesis, CNTs have been widely used to fabricate freestanding ICNEs through mechanical interlocking due to excellent conductivity and high mechanical properties as a result of large length-to-diameter ratios. In addition, 3D CNT frameworks can provide adequate mechanical strength to suppress structural distortion, sufficient inner spacing for high mass loading and highly porous and conductive channels for efficient ions diffusion [148]. 2D MXene or graphene with high aspect ratios of nanosheets has also been applied to fabricate high-mass-loading ICNEs due to favorable mechanical stability and outstanding electronic/ionic conductivity in which the large 2D structure and high mechanical strength of rGO nanosheets can allow for advanced flexible batteries that can function well after folding and bending (Fig. 9a) [149], whereas graphene can wrap irregular particles into densely compact integrated structures because its large sheet-like morphology can strongly overlap each other to function as "peels" for packaging. For example, Yang et al. [150] fabricated an ICNE with graphene-packed ACs through a capillary process (Fig. 9b) that possessed high intercontact and a dense and compact structure but with ion channels. These researchers further reported that their highly dense but porous AC/graphene electrode can minimize the thickness of conventional thick AC electrodes [151], highlighting the benefits of this thickness-matching strategy in terms of unimpeded electron/ion conductive pathways built by 3D graphene networks.

Despite great success in the development of HMLEs based on ICNE achieved through CNTs, graphene and MXene, high production costs and complex fabrication processes make them less competitive than conventional commercial electrodes. Alternatively, the cellulose

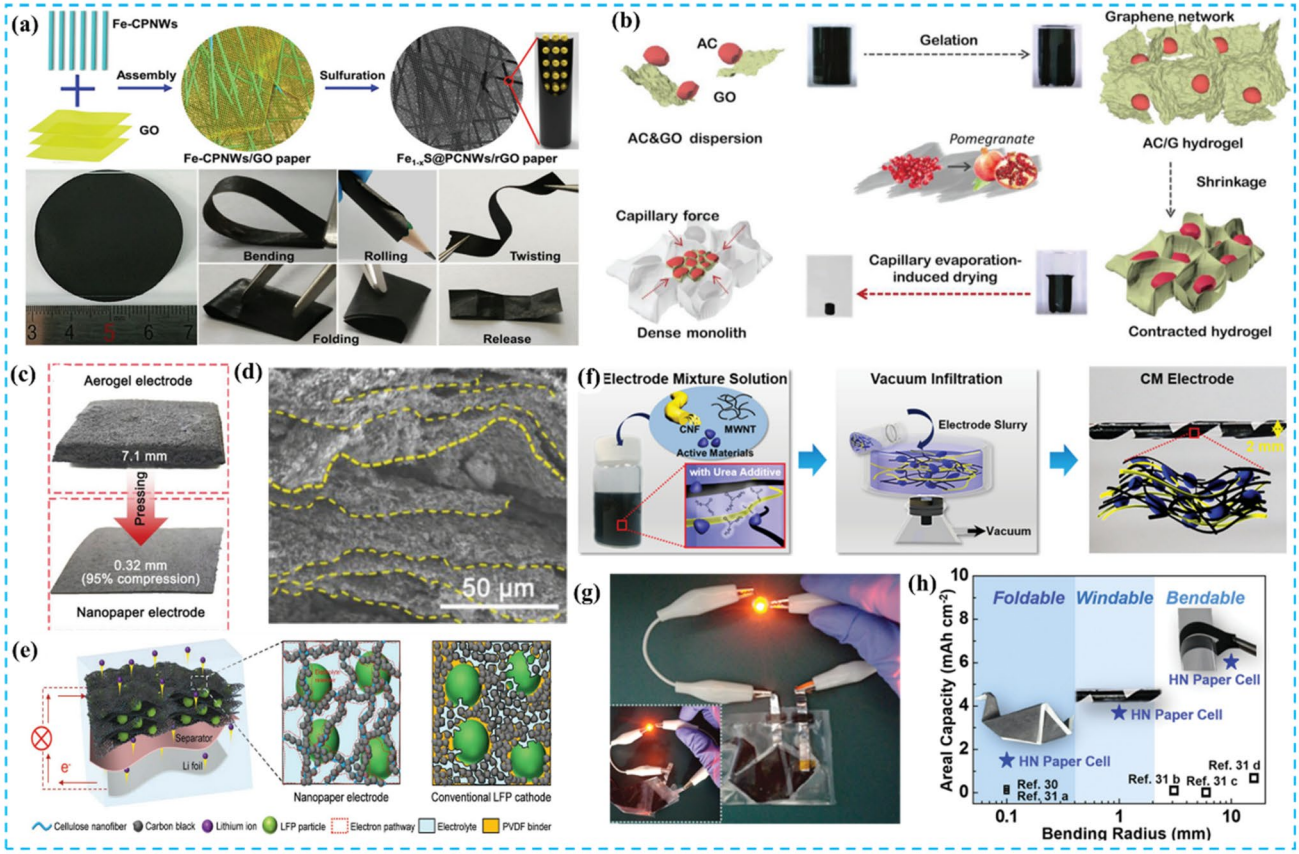

Fig. 9 **a** Fabrication of flexible ternary $Fe_{1-x}S$@porous carbon nanowires/rGO hybrid film electrodes and their bending/rolling/twisting/folding properties. Reprinted with permission from Ref. [149]. Copyright © 2019, Wiley–VCH. **b** Fabrication of packed ACs into dense graphene networks. Reprinted with permission from Ref. [150]. Copyright © 2019, Wiley–VCH. **c** Photograph and **d** SEM image of a compact and freestanding electrode as enabled by the conductive cellulose nanofiber and corresponding microstructure and **e** schematics illustrating ion/electron conductive pathways. Reprinted with permission from Ref. [60]. Copyright © 2018, Wiley–VCH. (**f**–**h**) Paper electrode derived from vacuum infiltration and its bending performance. Reprinted with permission from Ref. [152]. Copyright © 2015, Wiley–VCH

nanofiber (CNF) as an emerging biomass-derived material that is able to fabricate freestanding and flexible electrodes due to a nanofiber-like structure and high mechanical strength has been reported to be promising in the synthesis of highly conductive 3D networks through combination with conducting agents as effective scaffolds to establish ICNEs. For example, Hu et al. [60] engineered a flexible ICNE based on LFP up to 60 mg cm^{-2} with abundant electron/ion transfer pathways through the spontaneous electrostatic self-assembly of negatively charged CNFs and conductive CB particles and reported that the obtained ICNE possessed many desirable characteristics including: (1) a mechanically robust CNF backbone that contributed to compact electrodes after post-densification (Fig. 9c, d); (2) the essential electrolyte affinity of the CNF and an interconnected network structure that resulted in continuous electron/ion transport pathways (Fig. 9e); and (3) the naturally abundant CNF and low-cost CB that allowed the composite electrode to be attractive for practical application.

Aside from ICNEs based on singular CNTs, graphene, MXene and CNFs, corresponding composite networks can also provide promising performances due to synergetic effects. For example, Lee et al. [153] fabricated an ICNE by coupling 1D nano-building blocks of polyacrylonittrle nanofibers with MWCNTs through electrospraying and electrospinning as well as a hetero-nanonet paper electrode using CNFs as 1D building blocks to incorporate with MWCNTs through vacuum infiltration (Fig. 9f) that was able to provide an LFP cathode material loading of over 90 mg cm^{-2} at an electrode thickness of 1400 μm [152]. These hybrid paper electrodes also exhibited flexibility and high mechanical robustness (Fig. 9g, h), indicating practical significance in the building of flexible, wearable, and portable electronics.

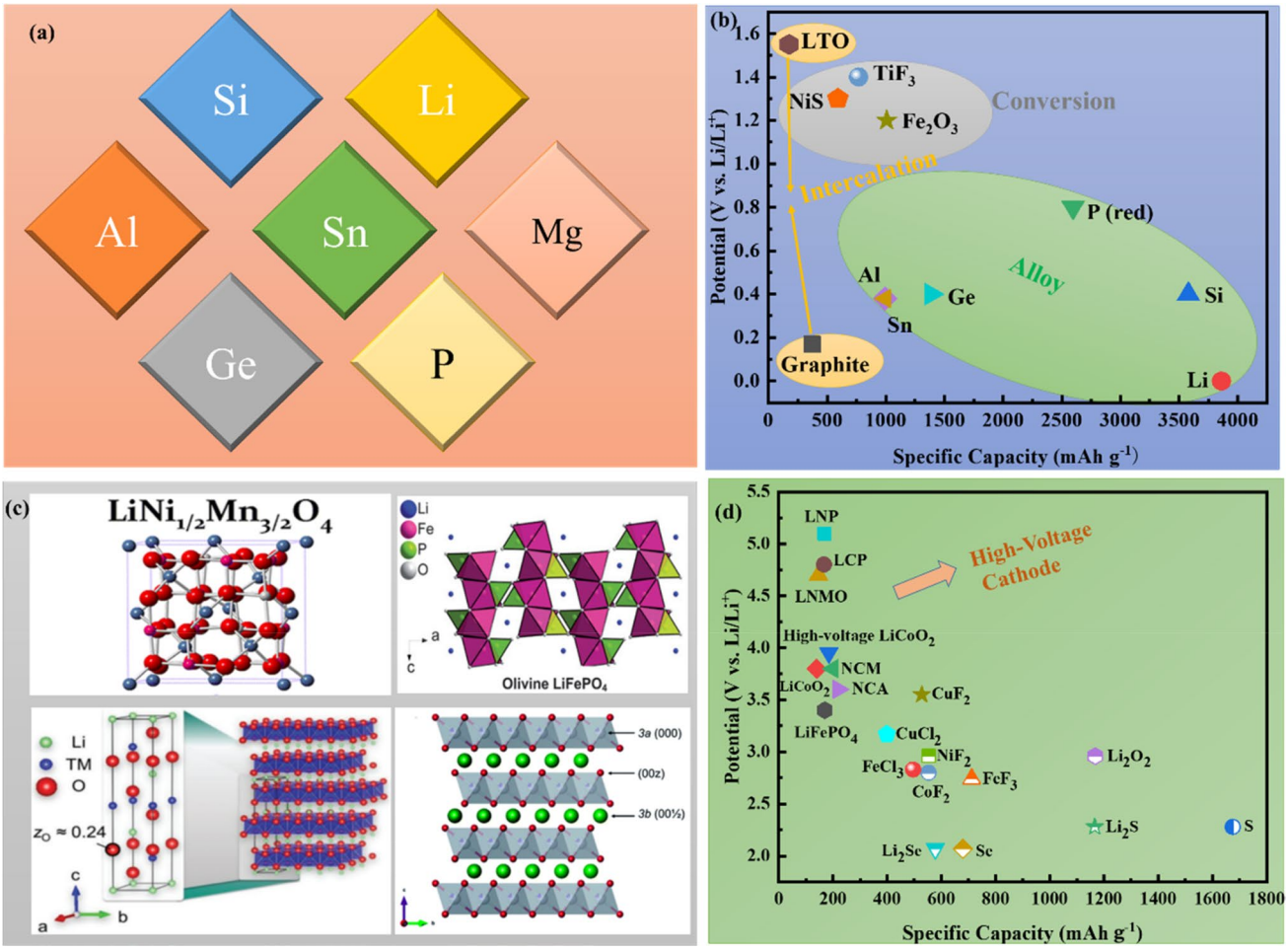

Fig. 10 **a** Representative anode materials for LIBs. **b** Theoretical gravimetric capacities of selected anode materials. **c** Crystal structures of $LiNi_{1/2}Mn_{3/2}O_4$, $LiFePO_4$, NCM and NCA. They are Reprinted with permission from Ref. [154], Copyright © 2012, American Chemical Society; Ref. [155], Copyright © 2017, American Chemical Society; and Ref. [156], Copyright © 2020, The Royal Society of Chemistry. **d** Gravimetric capacities of selected cathode materials. Reprinted with permission from Ref. [7]. Copyright © 2020, The Royal Society of Chemistry

4 Recent Progress of HMLEs in Advanced Secondary Batteries and Supercapacitors

4.1 Lithium-Ion Batteries

Lithium-ion batteries (LIBs) have been successfully commercialized and are integral to our daily life for portable electronic devices and electric vehicles. However, current commercial LIBs have encountered a bottleneck in terms of limited energy density due to the fundamental capacity limits of intercalation-type cathodes and graphite anodes, and great efforts have been devoted to the exploration of high voltage cathodes [177, 178], high capacity anodes and electrolyte engineering [7, 179]. Figure 10 displays representative commercial and high voltage cathode materials and state-of-the-art anode materials as well as corresponding gravimetric capacities. Based on this, the intensive research into HMLEs based on these electrode materials is ongoing and in this section, a summary of the recent advancement in HMLEs based on these cathode and anode materials along with their advantages and bottlenecks will be provided. Table 1 lists the electrochemical performances of select HMLEs for LIBs.

4.1.1 Anode Modification

Based on lithium storage mechanisms, LIB anodes can be divided into intercalation-type [such as graphite and $Li_4Ti_5O_{12}$ (LTO)] [180, 181], conversion-type (such as NiS and Fe_2O_3) [182] and alloy-type (such as Ge, Sn, red P and Si) [183] anodes with different theoretical capacities and lithiation potentials [184]. Among these, lithium intercalated graphite (LIG) has been extensively commercialized due to common advantages of low and flat working

Table 1 Electrochemical performances of representative HMLEs for LIBs

Materials	Mass loading (mg cm^{-2})	Electrode thickness (μm)	Gravimetric capacitance (mAh g^{-1})	Areal capacitance (mAh cm^{-2})	Volumetric capacitance (mAh cm^{-3})	Rate performance (mAh cm^{-2})	Reference
MXene	50	352	97 at 30 mA g^{-1}	5.9 at 30 mA g^{-1}	–	1.58 at 243 mA g^{-1}	[157]
$Li_4Ti_5O_{12}$	32.3	820	147 at 0.2 C	4.8 at 0.2 C	–	3.6 at 2 C	[158]
TiO_2 film	21	135	–	4.8 at 0.5 C	355 at 0.5 C	3.7 at 1 C	[159]
$LiCoO_2$	138	600	–	16.7 at 0.38 mA cm^{-2}	–	–	[160]
$LiMO_2$	60	322	120 at 0.2 C	6 at 0.2 C	–	–	[79]
$Li_4Ti_5O_{12}$	110	550	148 at C/24	13.3 at C/24	340 at C/24	112 mAh g^{-1} at C/12	[161]
$Li_4Ti_5O_{12}$	30	1500	–	4.74 at 0.2 C	31.6 at 0.2 C	–	[162]
$LiFePO_4$	50	1500	–	7.5 at 0.1 C	–	–	[163]
FeS_2/CNT	14.4	–	696 at 0.5 mA cm^{-2}	10 at 0.5 mA cm^{-2}	–	–	[164]
HPCO/NC	10	–	–	7.1 at 0.2 C	–	–	[165]
TNO_{-x}/C	11	–	–	2.35 at 0.5 C	–	0.35 at 6 C	[166]
$LiFePO_4$	108	1000	133 at 0.2 mA cm^{-2}	14.5 at 0.2 mA cm^{-2}	–	~5 at 2 mA cm^{-2}	[167]
GF/PC/GP	30	–	205.88 at 2 mA cm^{-2}	11.63 at 2 mA cm^{-2}	260.24 at 2 mA cm^{-2}	–	[168]
Graphite	9.1	200	~100 at 1 C	–	–	–	[124]
$LiFePO_4$	85	900	157 at 0.7 mA cm^{-2}	13.2 at 0.7 mA cm^{-2}	–	7.9 at 15 mA cm^{-2}	[169]
$LiFePO_4$	60	800	–	7.6 at 0.5 mA cm^{-2}	95 Ah L^{-1} at 0.5 mA cm^{-2}	0.7 at 20 mA cm^{-2}	[18]
Co_3O_4	14.3	370	842 at 200 mA g^{-1}	14.9 at 200 mA g^{-1}	–	–	[136]
$LiFePO_4$	175	1000	143.7 at 0.05 C	21.3 at 0.05 C	213 Ah L^{-1} at 0.05 C	0.68 at 2 C	[170]
NMC 622	70	300	~18 at 0.02 C	~13 at 0.02 C	–	–	[38]
$LiFePO_4$	20	–	161 at 0.5 mA cm^{-2}	3.2 at 0.5 mA cm^{-2}	208 Ah L^{-1} at 0.5 mA cm^{-2}	1.8 at 5 mA cm^{-2}	[60]
Vanadium nitride (VN)	18.3	–	760 at 100 mA g^{-1}	4 at 100 mA g^{-1}	–	–	[171]
NMC711	45	200	160 at 0.025 C	7.4 at 0.025 C	–	–	[172]
NMC811	155	740	190 at 0.05 C	29.5 at 0.05 C			[69]
Si/CNT	14.3	210	3150 at 0.03 C	45.4 at 0.03 C	–	–	[69]
Si/MXene	5.43	83	2240 at 0.05 C	12.2 at 0.05 C	–	–	[72]
Si nanowire	12.8	–	~1172 at 0.1 mA cm^{-2}	15 at 0.1 mA cm^{-2}	–	–	[173]
$LiFePO_4$	72	400	117 at 0.2 C	8.4 at 0.2 C	–	–	[174]
$LiFePO_4$	60	600	117 at 1 mA cm^{-2}	8.8 at 1 mA cm^{-2}	–	–	[87]
$LiFePO_4$	–	500	–	13.7 at 0.1 C	–	–	[175]
$Li_4Ti_5O_{12}$	140	500	–	15.2 at 1/24 C	319 at 1/24 C	–	[176]

GF/PC/GP refers to graphite fibers bonded with pyrolytic carbon and graphite nanoplatelets

potentials, cost-effectiveness, an outstanding cycling life and environmental friendliness, but is limited by low specific capacities [180]. In addition, the low Li-ion transport rate (10^{-12}–10^{-14} cm^2 s^{-1}) of LIGs as well as the high charge carriers and extremely anisotropic insertion/extraction kinetics of lithium in graphite particles also negatively influence lithium storage behaviors in terms of energy and power density as well as rate performance [124, 180]. Moreover, serious concentration polarization under high charge rates can lead to more negative electrochemical potentials for anode regions than that of Li metal, which can lead to the thermodynamically favorable formation of metallic Li dendrites

[185]. These issues are magnified in HMLE designs and therefore require rational structural modification. Based on this, Studart et al. [124] proposed an ingenious strategy to design thick-graphite anodes with an out-of-plane aligned structure controllably guided through the use of low external magnetic fields, in which their resulting magnetically assisted VAN electrode was composed of superparamagnetic Fe_3O_4 nanoparticle-functionalized graphite that was magnetically responsive towards a rotating magnetic field (H_{rot}). Here, the graphite platelets became an oriented structure along the planes of the applied rotating magnetic field and aligned perpendicular to the current collector surface, which reduced the tortuosity of Li-ion transport pathways across the thick electrode by a factor of four to enhance capacity at high rates. As a result, a corresponding LIB using the thick graphite anode (200 μm) under a high mass loading of 9.1 mg cm^{-2} showed a reversible capacity of over 100 mAh g^{-1} at 1 C, which was larger than the capacities of electrodes consisting of random slurry coatings. Dasgupta et al. [185] also developed a thick-graphite anode through structural modification involving the precise manufacturing of a highly ordered laser-patterned electrode structure (HOLE) with uniform and close-packed hexagonal arrays of vertical pore channels through the electrode thickness. Here, these researchers reported that the vertical channels can function as linear diffusion pathways for rapid mass

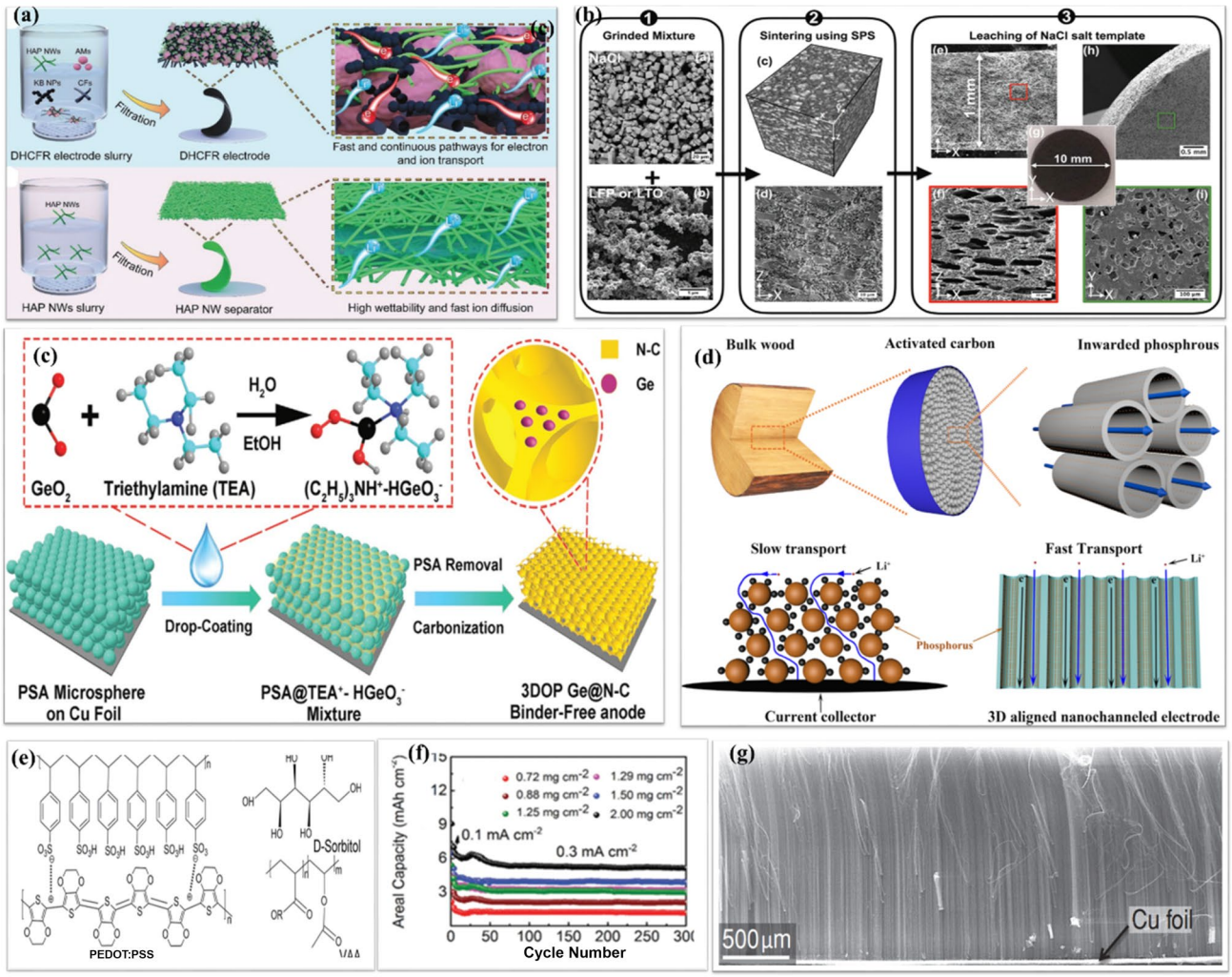

Fig. 11 **a** Preparation of a paper electrode based on inorganic hydroxyapatite nanowires. Reprinted with permission from Ref. [187]. Copyright © 2019, Wiley–VCH. **b** NaCl template-assisted SPS of thick electrodes. Reprinted with permission from Ref. [170]. Copyright © 2018, Wiley–VCH. **c** Preparation process of 3D ordered Ge encapsulated in a carbon framework. Reprinted with permission from Ref. [188]. Copyright © 2020, Wiley–VCH. **d** Illustration of red phosphorus loaded into a wood carbon framework showing rapid mass transport. Reprinted with permission from Ref. [189]. Copyright © 2019, Elsevier. **e** Molecular structures of binder components and **f** corresponding electrochemical performances. Reprinted with permission from Ref. [190]. Copyright © 2018, Wiley–VCH. **g** SEM image and a schematic of a thick sandwiched vertical-aligned Si electrode. Reprinted with permission from Ref. [191]. Copyright © 2012, Wiley–VCH

transport throughout the electrode, allowing the high-loading graphite anode to achieve capacities over 3 mAh cm^{-2} (9.48 mg cm^{-2}) as well as industrial pouch cells with capacities larger than 2 Ah. More importantly, corresponding morphological studies of the pouch cells after 6 C fast-charging for 100 cycles showed the lack of Li plating on the electrode surface or inner pore channels as well as the retention of a clean interconnect surface, indicating that the corresponding HOLE-graphite design was conducive to long-term and rapid-charge cycling in LIBs. Overall, the introduction of aligned and interconnected macropores or extra voids into thick-graphite electrodes can effectively improve ion transport efficiency. However, effective techniques to precisely control the inner pore structure of thick graphite anodes to balance volumetric energy density in corresponding cells remain lacking.

LTO is another prominent commercial LIB anode that was first reported in 1983 by Murphy et al. [186] and possesses attractive advantages such as facile fabrication, high safety and cycling stability due to a unique "zero-strain" structure. However, a low theoretical capacity of 175 mAh g^{-1} severely hinders overall energy density in corresponding LIBs. In addition, intrinsic kinetic issues involving low electrical conductivity (10^{-16}–10^{-9} S cm^{-1}) and poor Li-ion diffusion efficiency (10^{-16}–10^{-9} cm^2 s^{-1}) also result in poor rate capability and therefore, integrated electrode designs with continuous electronic/ionic conducting networks are promising in the synthesis of thick-LTO-based anodes. For example, Li et al. [187] used 1D inorganic hydroxyapatite nanowires as a self-supported basic skeleton for incorporation with individual building blocks (i.e., electroactive LTO, conductive ketjen black and carbon fibers as conductivity and mechanical strength reinforcements respectively) through self-assembly to obtain a porous and integrated network-like hybrid monolithic electrode (Fig. 11a). It reported that the paper-like electrode with the interconnected porous structure possessed continuous pathways for rapid electron and ion transport, which allowed for the development of a high mass loading LTO anode (10 mg cm^{-2}) to match with a high mass loading AC cathode (20 mg cm^{-2}) in a lithium-ion capacitor to deliver a high areal energy density of 1.58 mWh cm^{-2} as well as excellent thermal durability from room temperature to 150 °C. Spark plasma sintering (SPS) has been demonstrated to be an effective method to fabricate dense electrodes with low particle/grain coarsening during densification which combined with cost-effective and easily removable salt templates as pore optimization additives. Seznec et al. [170] fabricated a 1000-µm-thick monolithic LTO anode with homogenously distributed macroporous channels (Fig. 11b) to achieve an areal capacity of 25.5 mAh cm^{-2} at 0.05 C and high capacity retention of 94% after 10 cycles, demonstrating that combining novel controllable templates with SPS is promising in the further fine-tuning of porosity in low-tortuosity HMLEs.

The limited Li-ion diffusion rates of conventional graphite and LTP anodes have further triggered the development of high-power anodes that can retain high levels of charge storage at high rates in which charge storage behavior is based on surface-controlled kinetics rather than diffusion-controlled battery types. The construction of advanced HMLEs based on high-power anode materials can also allow for superior batteries with both high energy/power densities. For example, orthorhombic phase Nb_2O_5 (T-Nb_2O_5) has been reported to be a high-power anode material with rapid Li-ion storage due to a typical pseudocapacitive intercalation reaction process [192]. Despite this, the low electronic conductivity (3×10^{-6} S cm^{-1}) of T-Nb_2O_5 restricts application in high-rate HMLE designs [193]. Here, nanostructured and carbon-incorporated hybrid structures can improve the rate capability of T-Nb_2O_5 electrodes in which nanowire-structured T-Nb_2O_5 and core–shell Nb_2O_5/C composites have been proposed [192, 194]. For example, Duan et al. [195] fabricated a 3D holey-graphene/Nb_2O_5 electrode with interpenetrating electron and ion transport networks as well as a hierarchical porous structure and reported stable reversible lithium storage and high rate performances with a mass loading increase from 1 to 11 mg cm^{-2} at 10 C as well as a high mass loading of 22 mg cm^{-2} with an areal capacity of 3.9 mAh cm^{-2}.

Compared with low-capacity intercalation-type anode materials, conversion and alloy-based anodes with higher theoretical capacities such as Fe_2O_3 with 1007 mAh g^{-1}, Si with 3579 mAh g^{-1}, Ge with 1384 mAh g^{-1} and red P with 2596 mAh g^{-1} have also been developed to address the growing demands of high-energy–density LIBs [7]. However, severe volume expansion and unstable SEI formation hinder development from laboratory to industry application and corresponding solutions should be based on considerations in terms of practical application, especially in HMLE design. Here, verified conversion and alloy anode materials as well as electrochemical features such as the coating or encapsulation of nanostructures with robust carbon matrixes are regarded to be general solutions to mitigate these challenges, resulting in the development of materials such as 3D-structured Sn/C electrodes with 20 vol% Sn loading [196], 2D ZnO anchored onto 3D interconnected carbon foam with a ZnO loading of 3–4 mg cm^{-2} [197], micronized Ge_3N_4/C with a mass loading of 3.5 mg cm^{-2} [198], 3D holey graphene/SnO_2 with a mass loading of 12 mg cm^{-2} and areal capacities up to 14.5 mAh cm^{-2} [199], and folded graphene/SnO_2 with a mass loading of 5 mg cm^{-2} [109]. Here, encapsulated nanoparticles within carbon matrixes can aggregate during cycling and lead to the insufficient utilization of inner-located active materials, particularly under high charge rates [188]. These unfavorable interactions between

active nanoparticles and carbon supports can further result in low mass loading and therefore, structural tailoring to achieve the uniform distribution, high mass loading and nanostructuring of active particles into carbon matrixes is necessary. Based on this, Wu et al. [188] encapsulated Ge quantum dots evenly into a 3D ordered carbon framework through a template-assisted method (Fig. 11c) and reported that the well-ordered porous architecture with its honeycomb-like thin walls enabled the well-dispersion of ultrafine Ge quantum dots (2–5 nm) with an ultrahigh loading ratio of 82.9%. As a result, a high mass loading of 8 mg cm^{-2} was achieved for a Ge-based anode to combine with an LFP cathode, allowing a corresponding full cell to display a high discharge capacity of 800 mAh g^{-1} even after 200 cycles at 100 mA g^{-1}. Zheng et al. [189] further fabricated a high-loading phosphorus anode by wrapping phosphorus within rGO followed by confinement into a 3D wood-derived micro-channeled carbon framework (Fig. 11d) and reported that the resulting electrode achieved a high phosphorus loading of 16.6 mg cm^{-2} and a highly stable cycling performance of 9.5 Ah cm^{-2} at 1 mA cm^{-2}, which these researchers attributed to the unique 3D conductive carbon network that can provide adequate spacing to tolerate volume change and the highly conductive pathways to enhance electron/ion transport.

Silicon has also attracted great interest as the most promising candidate to replace graphite in future LIBs due to a high theoretical capacity, natural abundance and a low lithiation voltage plateau. However, extremely large volume expansions up to 400% during lithiation/delithiation greatly limit further application. In addition, silicon anodes are often tested at low Si mass loadings of less than 1 mg cm^{-2}, which makes them less attractive in practical applications that require high areal capacities over 4 mAh cm^{-2} [200]. To address these issues, great attention has been paid in recent years to the surface and interface engineering of nanostructured silicon hybrids through rational coating to enhance cycling stability and areal mass loading. These coatings include silicon oxide coatings, metal or metal oxide coatings, carbon coatings, conducting polymer coatings and multifunctional coatings [201], in which carbon coatings are the most attractive due to carbon possessing multiple advantages of cost-effectiveness, high electrical conductivity, facile fabrication, structural flexibility with various dimensionalities and nanostructures and high mechanical strength to buffer volume expansion. For example, Cui et al. [104] proposed a pomegranate-inspired nanoscale design to achieve a hierarchical composite structured silicon anode through the complete and individual encapsulation of silicon inside coating carbon frameworks in which the formation of initial well-defined void spaces built by SiO_2 templates provided adequate room to buffer volume expansion. As a result, a high areal capacity of 3.67 mAh cm^{-2} at 0.03 mA cm^{-2} was obtained for a 3.12 mg cm^{-2} mass-loading Si anode as well as high capacity retention of 94% after 100 cycles at 0.7 mA cm^{-2}. Graphene and CNTs are also representative carbon matrixes that can be incorporated with nanoscale silicon to provide continuous networks for electron and ion transport and serve as buffers to accommodate volume change as a result of their large surface areas, excellent mechanical flexibility and high electrical conductivity. For example, Nicolosi et al. [69] developed a general and scalable method to produce ultra-thick electrodes compatible with various AMs involving an innovative materials-science-based strategy using specifically segregated network structured CNTs as carbon matrixes. These researchers highlighted that segregated CNT networks can enable the construction of extremely thick electrodes with largely increased toughness that were over 500 times tougher than traditional electrodes as well as favorable electrical conductivities of 10^4 S m^{-1} and low charge-transfer resistances. As a result, ultrathick silicon anodes can be obtained with maximum mass loadings of 15 mg cm^{-2} (210 μm thick) as well as remarkable areal capacities of 45 mAh cm^{-2} at 1/30 C. A correspondingly optimized full cell with a total mass loading of 167 mg cm^{-2} further displayed a state-of-the-art areal capacity of 29 mAh cm^{-2} and gravimetric/volumetric energy densities of 480 Wh kg^{-1} and 1600 Wh L^{-1} respectively. Zhi et al. [202] further developed a freestanding electrode involving nanoscale silicon impregnated assembly of template carbon-bridged oriented graphene networks that successfully delivered a reversible areal capacity of 6 mAh cm^{-2} at 3 mA cm^{-2}. These researchers also reported that their flexible graphene/Si structure enabled stable cycling performances in which 4 mAh cm^{-2} was maintained after 100 cycles at 15 mA cm^{-2}. Similarly, Nicolosi et al. [72] reported that MXene conducting frameworks can ensure high silicon-loadings up to 13 mg cm^{-2} in a 450-μm-thick anode to deliver a remarkable areal capacity of 23 mAh cm^{-2} in which the unique layered structures of graphene and MXene can allow for interlayer sliding upon the volume expansion of silicon and the conductive framework can allow for enhanced storage capacity at high rates.

Binder systems are vital to ensure electrode integrity during deep charging/discharging. However, traditional binders such as PVDF are not suitable for silicon anodes because of intrinsically low elasticities [203]. To address this, traditional singular binders can be replaced with multifunctionalized polymer binders in which efficient binders should possess good adhesion with silicon through hydrogen bonding as well as reversible deformation properties to match with silicon microstructural variations. Based on this, poly(acrylic acid) (PAA) as a typical water soluble binder containing abundant carbonyl groups, low swelling and good elasticity can be coupled with poly(vinyl alcohol) (PVA) to allow a composite binder (PAA@PVA) to steady silicon

loadings of over 2.4 mg cm^{-2} in corresponding LIB anodes and achieve a high areal capacity of 4.3 mAh cm^{-2} as well as high coulombic efficiency even at 4 A g^{-1} [200]. The deformable interpenetrated polymer network and enriched functional groups of PAA@PVA can allow for good rate performance and long cycling stability in silicon anodes. To improve binding between silicon and PAA, Liu et al. [204] further wrapped polydopamine (PDA) onto silicon surfaces to allow imino groups to react with the carboxyl groups of PAA and form a stronger binding system. As a result, an obtained 2.0 mg cm^{-2} mass loading Si@PDA/PAA electrode was able to display an areal capacitance of 3.69 mAh cm^{-2} and operation stability for over 80 cycles. The repeated expansion and contraction of silicon will inevitably lead to the isolation and aggregation of powdered additives, but resulting in electric disconnection and electrode collapse. These challenges can be rationally resolved, however, through the use of conducting polymer binders that can serve as both binders and conductive additives. For example, Huo et al. [190] fabricated a highly stretchable conductive glue with high electrical conductivity and excellent stretchability from the crosslinking of D-sorbitol and vinyl acetate-acrylic (VAA) onto a PEDOT:PSS conducting polymer (Fig. 11e) and reported that this conductive binder system was able to support high silicon loadings of up to 90% at 2 mg cm^{-2} to produce an areal capacity of 5.13 mAh cm^{-2} (Fig. 11f).

The structural engineering of silicon-based materials such as hollow nanostructures, porous silicon, and silicon nanowires has further been developed to tolerate mechanical strain from volume expansion. Nanostructured silicon can also improve specific surface area, shorten ionic transport length and enhance electrical conductance [201]. Based on this, several nanostructured silicon materials have been proposed to enable stable HMLEs, including 1.9 mg cm^{-2} mass-loading silicon nanorods that can provide an areal loading capacity of 2.7 mAh cm^{-2} [205], 4.1 mg cm^{-2} mass-loading watermelon-inspired Si/C microspheres that can provide an areal loading capacity of 2.54 mAh cm^{-2} [206], silicon nanowires with high areal loading capacities ranging from 3 to 15 mAh cm^{-2} [173] and 8.5 mg cm^{-2} mass-loading 3D conducting Si/C networks that can provide an areal loading capacity of 4 mAh cm^{-2} [207]. Another effective method to design ultrathick electrodes involves the use of aligned CNTs as supporting matrixes to coat Si/C composites in which the vertically straight CNTs of the resulting sandwich-like core–shell structure can produce 1000-μm-thick Si/C anodes through vapor deposition, allowing for the uniform and precise control of AM coatings (Fig. 11g) [191]. Here, the aligned conducting tubes with vertically oriented channels can contribute to rapid electron/ion transport and allow the Si anode to possess a high capacity of 3000 mAh g^{-1}. The pre-forming of meso/macropores inside bulk Si materials to buffer large volume expansion is also promising. For example, Liu et al. [208] proposed large-sized mesoporous Si sponge with a highly porous structure comprising of thin Si walls surrounding 50-nm large pores and reported that this structure decreased volume expansion to only 30% during charge/discharge. It contributed to more than 80% capacity retention over 1000 cycles as well as high areal capacities of up to 3–4 mAh cm^{-2} under mass loadings of 3.5–4 mg cm^{-2} and over 4 mAh cm^{-2} at a mass loading of 5.3 mg cm^{-2}. Alternatively, nanostructured Si materials inevitably expose more active surfaces with high reactivities to electrolytes, which will result in electrolyte decomposition and unstable SEI formation, and therefore, the rational combination of structural engineering with interfacial modification is necessary.

4.1.2 Cathode Modification

To improve battery energy density based on cathode materials, researchers have focused on the exploration of high capacity and high voltage cathode materials [209]. Here, LCO and LFP are two representative commercial cathode materials with low working potentials (< 3.8 V vs. Li^+/Li) and theoretical capacities of 140 and 170 mAh g^{-1} respectively that were first reported by Goodenough et al. [209, 210]. Corresponding advantages continue to attract intense research after 30 years in development in which LFP electrodes display superior thermal stability, cycling stability and reversibility [210], whereas LCO electrodes possess high electrical/Li^+ conductivity and high volumetric performance [209]. Because of this, the development of high loading cathodes for LIBs usually involves LCO/LTP as model systems in which the most common method to obtain high-performance LCO/LTP-based HMLEs is the introduction of rational pores/channels for rapid mass diffusion. And aside from widely used 3D-printing and ice-template freeze drying methods to design orientated porous structures, this section will mainly focus on relatively facile and cost-effective structure-templated strategies to fabricate HMLEs based on LCO/LTP.

The use of naturally abundant or commercially available structural templates is more attractive in the construction of well-ordered channels in high loading cathodes. For example, Hu et al. [18] used an anisotropic wood carbon framework (WCF) with an enriched vertical multichannel structure to fabricate ultrathick LFP cathodes up to 800 μm thick with a high areal loading of 60 mg cm^{-2} (Fig. 12a) in which the freestanding LFP/WCF anode showed highly conductive properties (6.75 S cm^{-1} for electrical conductivity and 5.2×10^{-11} cm^2 s^{-1} for the Li-ion diffusion coefficient) due to the continuous connected network and well-developed vertically aligned pores/channels (Fig. 12b). As a result, the LFP/WCF electrode delivered a high areal capacity of 7.6 mAh cm^{-2} at 0.5 mA cm^{-2} and 1.7 mAh cm^{-2} at

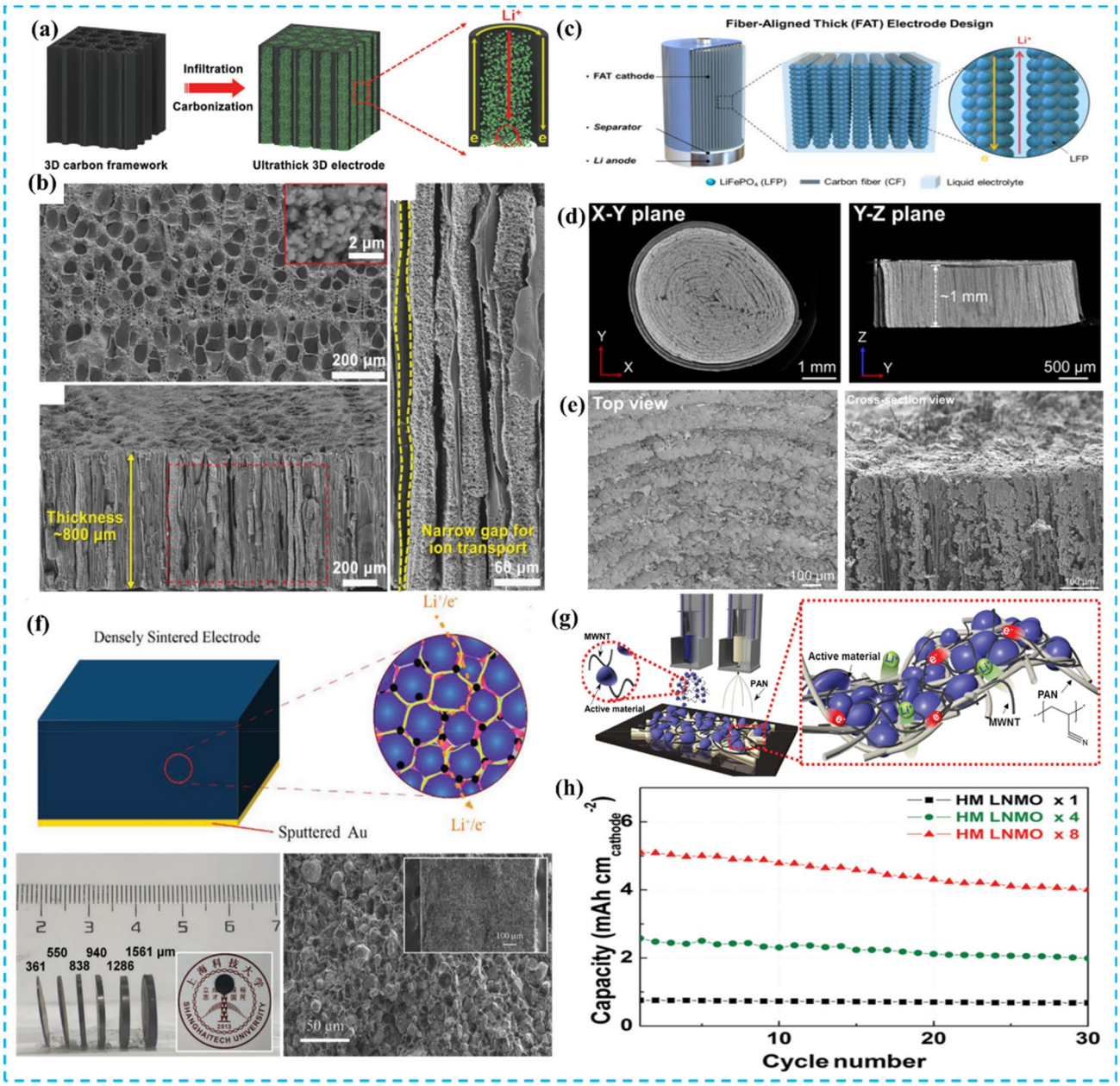

Fig. 12 **a** Schematic of WC as 3D current collectors filled with LFP and **b** corresponding SEM images. Reprinted with permission from Ref. [18]. Copyright © 2017, Wiley–VCH. **c** Schematic of a thick electrode-based aligned carbon fiber, **d** 3D reconstructed X-ray–CT images of the thick electrode and **e** top-view and cross-view SEM images. Reprinted with permission from Ref. [212]. Copyright © 2020, American Chemical Society. **f** Fabrication of densely sintered HMLEs and their photographs and SEM images. Reprinted with permission from Ref. [213]. Copyright © 2019, Wiley–VCH. **g** Fabrication of PAN-nanofiber and MNCNTs based flexible electrodes through electrospraying/electrospinning, **h** cycling performances of LNMO electrodes with different loadings. Reprinted with permission from Ref. [153]. Copyright © 2016, Wiley–VCH

10 mA cm^{-2}, indicating good rate performances. Similarly, Cui et al. [17] used wood as a sacrificial template combined with the sol–gel process to fabricate a 1000-μm-thick LCO cathode with a mass loading of 206 mg cm^{-2} and obtained remarkable capacities as high as 22.7 mAh cm^{-2}. Biomass-templating is also a feasible method to fabricate cathode materials with varying morphology. For example, Park et al. [211] developed three bio-template derived LCO particles including cotton-derived fiber-like porous LCO, wood-derived honeycomb-like LCO and grass pollen-derived hollow LCO spheres. Shi et al. [212] recently obtained a carbon-fiber-aligned thick electrode by rolling LFP-loaded

carbon fiber membranes into a cylindrical shape, followed by cutting perpendicular to the axial direction to form ultrathick electrodes with through-thickness fiber alignment (Fig. 12c). Here, these researchers reported that the resulting structure with low-tortuosity, a vertically aligned fiber matrix and an interconnect carbon framework enabled efficient electron and ion delivery (Fig. 12d, e) and that the flexible carbon fiber matrix contributed to highly compressive features for the LFP cathode with compression strength of 2.8 MPa and a compression modulus of 36.8 MPa, indicating significant structural stability during cycling. As a result, a 1000-μm-thick LFP cathode with a total mass loading of 128 mg cm^{-2} achieved stable areal capacities of 19.8 and 15.8 mAh cm^{-2} at 0.5 and 5 mA cm^{-2} respectively. This roll-and-cut method is also promising in the fabrication of other electrode materials to facilely design HMLEs as well as batteries. However, thick and dense electrodes need to be designed to overcome inevitable capacity loss due to extra pores as introduced by the templates. For example, Liu et al. [213] used the cold sintering process (CSP) to fabricate a 450-μm-thick LCO cathode with a high mass loading of 110 mg cm^{-2} and a 1300-μm-thick electrode with a high mass loading of 368 mg cm^{-2} to provide an areal capacity of 28.6 mAh cm^{-2}. Here, the CSP was able to co-sinter the inorganic materials and the polymer into a dense structure in which high ion-conductive Ga-doped $Li_7La_3Zr_2O_{12}$ (LLZGO) nanoparticles serving as rapid ion pathways were applied at the grain boundaries of LCO particles to compensate for poor electrolyte diffusion in the HMLE (Fig. 12f).

High-voltage cathode materials such as $LiNi_{0.8}Co_{0.1}Mn_{0.1}O_2$ (NCM), $LiNi_{0.8}Co_{0.15}Al_{0.05}O_2$ (NCA), $LiNi_{0.5}Mn_{1.5}O_4$ (LNMO), $LiNiPO_4$ and $LiCoPO_4$ possess higher average working potentials generally larger than 3.8 V vs. Li^+/Li and HMLEs based on these high-voltage, high-capacity cathode materials are promising in high-energy–density LIBs. For example, Lee et al. [153] developed integrated paper electrodes comprised of 1D nanofibers interwoven with MWCNTs as a conductive matrix to accommodate high LNMO loading in which the nanofibers functioned as mechanical reinforcement and structured binders and MWCNTs served as conductive networks to produce a highly dense but porous conductive heteronanomat embedded with LNMO (Fig. 12g). Here, these researchers reported that the intermingled structure with uniformly formed interstitial void channels across the thickness direction contributed to 3D bicontinuous conducting frameworks for electron/ion transport (4.3 S cm^{-1} for electrical conductivity) and that the LNMO cathodes can be multi-stacked in series up to 420 μm thick to deliver a high areal capacity of 5.4 mAh cm^{-2} with 78.5% capacity retention after 30 cycles (Fig. 12h).

4.2 Sodium-Ion Batteries

Although LIBs have been widely commercialized, increasing energy demands for grid-scale EESSs inevitably raise

Table 2 Electrochemical performances of representative HMLEs for SIBs

Materials	Mass loading (mg cm^{-2})	Electrode thickness (μm)	Gravimetric capacitance (mAh g^{-1})	Areal capacitance (mAh cm^{-2})	Volumetric capacitance (mAh cm^{-3})	Rate performance (mAh cm^{-2})	Reference
$Na_3V_2(PO_4)_3$	3.5	–	116.6 at 1 C	–	–	70 mAh g^{-1} at 200 C	[135]
TiO_2/G	10.5	408	130 mAh g^{-1} at 100 mA cm^{-2}	2.27 at 0.53 mA cm^{-2}	–	–	[217]
Sn/C	20	–	76.3 at 100 mA g^{-1}	4.1 at 0.2 mA cm^{-2}	–	1 at 3 mA cm^{-2}	[106]
NNM	6	–	83 at 0.1 C	–	–	65 at 2 C	[218]
HC	17	195	267.5 at 0.02 A g^{-1}	4.3 at 0.02 A g^{-1}	–	139 mAh g^{-1} at 10 A g^{-1}	[219]
HC	5.1	–	> 250 at 50 mA g^{-1}	2.9 at 50 mA g^{-1}	–	–	[220]
HC	8.3	–	–	1.07 at 100 mA g^{-1}	–	–	[221]
$Na_3V_2(PO_4)_3$	7.5	130	114 at 0.05 C	–	–	80 mAh g^{-1} at 50 C	[222]
$Fe_{1-x}S$/rGO	11.2	98.5	89 at 0.1 A g^{-1}	–	107 at 0.1 A g^{-1}	–	[149]
CNTs/$FeSe_2$/C	16.9	–	–	5.06 at 100 mA g^{-1}	–	1.33 at 800 mA g^{-1}	[223]
$MoSe_2$/CNTs	13.9	–	–	4 at 100 mA g^{-1}	267 at 100 mA g^{-1}	–	[148]
MoS_2/CNTs	15	90	~420 at 0.2 mA cm^{-2}	6 at 0.2 mA cm^{-2}	> 650 at 0.2 mA cm^{-2}	–	[224]
$NaTi_2(PO_4)_3$	80	–	109 at 20 mA cm^{-2}	8.7 at 20 mA cm^{-2}	–	7.36 at 100 mA cm^{-2}	[225]

HC: hard carbon, NNM: $Na_{0.66}Ni_{0.33}Mn_{0.67}O_2$

concerns over the long-term availability of LIBs due to the low abundance (20 μmol mol^{-1}) and uneven distribution of lithium on the Earth [214]. These impediments of LIBs have triggered and necessitated further research into novel and alternative metal-ion batteries that are inexpensive and based on resource abundant elements. Here, sodium as an adjacent element to lithium in the periodic table represents a promising candidate to replace lithium in next-generation metal-ion batteries due to a highly adequate supply (23600 μmol mol^{-1}) and cost-effective features [215]. In addition, Al foil can be applied as lightweight current collectors in both the anode and the cathode of sodium-ion batteries (SIBs) and is conducive to cost reduction and energy density improvement [216]. Due to the similar electrochemical characteristics of SIBs to LIBs, the successful experiences and advanced strategies of LIBs can also be applied in the development of SIBs. Based on this, this section will provide a summary of the electrochemical performances of select HMLEs in SIBs as listed in Table 2.

4.2.1 Anode Modification

Electrode materials are vital components in high-performance SIBs and considerable efforts have been devoted to the exploration of anode materials for SIBs, which generally involve metals/alloys [226], metal oxides/sulfides/phosphides [227, 228], carbon materials and their composites [216]. Here, carbon materials represent the most promising anode materials for commercialization in the short-term due to low costs, natural abundance and excellent structural and chemical stability [229]. And of the various carbon materials, graphite as an industrial anode material in LIBs is not suitable for use in SIBs because sodium–graphite intercalation compounds (Na-GICs) are unstable based on density functional theory calculations in which the successful interaction of alkali metal ions such as K^+, Rb^+ and Cs^+ into graphite indicates the complex and unclear fundamental origins of metal-graphite intercalation chemistry [230]. Alternatively, hard carbon materials with disordered and non-graphitic carbon structure can deliver excellent sodium storage capacities approaching those of graphite anodes in LIBs as first evidenced by Dahn et al. [231] using glucose or cellulose as hard carbon precursors. In recent years, hard carbon has become a popular electrode material for SIBs that can impart high performances with capacities pushing beyond 300 mAh g^{-1} [232]. Unfortunately, corresponding drawbacks in terms of low initial coulombic efficiency (ICE) as a result of serious electrolyte decomposition and thick SEI formation can lead to metal dendrite generation and safety concerns [233]. Low ICEs will also lead to the consumption of large amounts of Na^+ extracted from cathodes to compensate for irreversible metal ion loss in side reactions, which will reduce overall energy density and cycling stability in full cells [234]. And because the basic challenges of hard carbon anodes will become more complex and difficult to tackle in HMLEs, research should directly address observable issues.

Hard carbon materials are always prepared from the pyrolysis of biomass or biomass derivates and organic molecules in which the final microstructure, composition and the surface state of hard carbon materials vary significantly based on carbon precursors and thus possess distinct sodium storage performances [238]. As compared with biomass derivates such as cellulose and lignin peeled from wood, the use of wood blocks to fabricate hard carbon materials is potentially more cost-effective and faster. For example, Hu et al. [147] used a wood derived carbon framework as freestanding and ultrathick hard carbon anodes and reported that the unique vertically aligned channels allowed for efficient electrolyte penetration in which control experiments demonstrated that the parallel cutting of WC with a low-tortuosity porous structure resulted in a superior capacity of 13.5 mAh cm^{-2} at 0.55 mA cm^{-2} as compared with the vertical cutting of WC with high tortuosity under a high mass loading of 55 mg cm^{-2} at a thickness of 850 μm (Fig. 13a). These researchers also reported that a full cell constructed by using the WC-anode and a $Na_3V_2(PO_4)_3$ cathode achieved a specific capacity of 117 mAh g^{-1}. Zheng et al. [108] also built a full SIB using a WC anode and a $Na(Cu_{1/9}Ni_{2/9}Fe_{1/3}Mn_{1/3})O_2$ cathode with mass loadings of 7 and 20.5 mg cm^{-2} respectively to achieved a matched areal capacity of 2 mAh cm^{-2}. In addition, the application of freestanding electrodes may be beneficial for the in-depth investigation of sodium storage mechanisms because of the lack of additional signals from binders/conductive additives during data collection. For example, Ghimbeu et al. [253] developed a freestanding hard carbon electrode derived from filter paper impregnated with phenolic resin involving mechanical pressing and carbonization in which the resulting electrode with a mass loading of 5.2 mg cm^{-2} showed a specific capacity of 300 mAh g^{-1} at 37.2 mA g^{-1}, with *operando* XRD results supporting an "adsorption-intercalation" storage mechanism in the hard carbon electrode. In addition to the regulation of material structures, the tailoring of basic properties and the formation of SEIs are also important. For example, Xu et al. [219] proposed a compatible strategy involving the matching of hard carbon anodes with ether-based electrolytes in which the ether-based electrolyte contributed to the creation of a thinner but more sustainable SEI layer with high ionic conductivity and faster Na^+ ion diffusion than those of ester-based electrolytes (Fig. 13b), allowing this matching concept of compatibility between the ether-based electrolyte and the hard carbon electrode to enable a high mass loading of 17 mg cm^{-2} and an excellent areal capacity of 4.3 mAh cm^{-2} with ICE of 85.9%. Ether-based electrolytes can also stabilize hard carbon anodes with

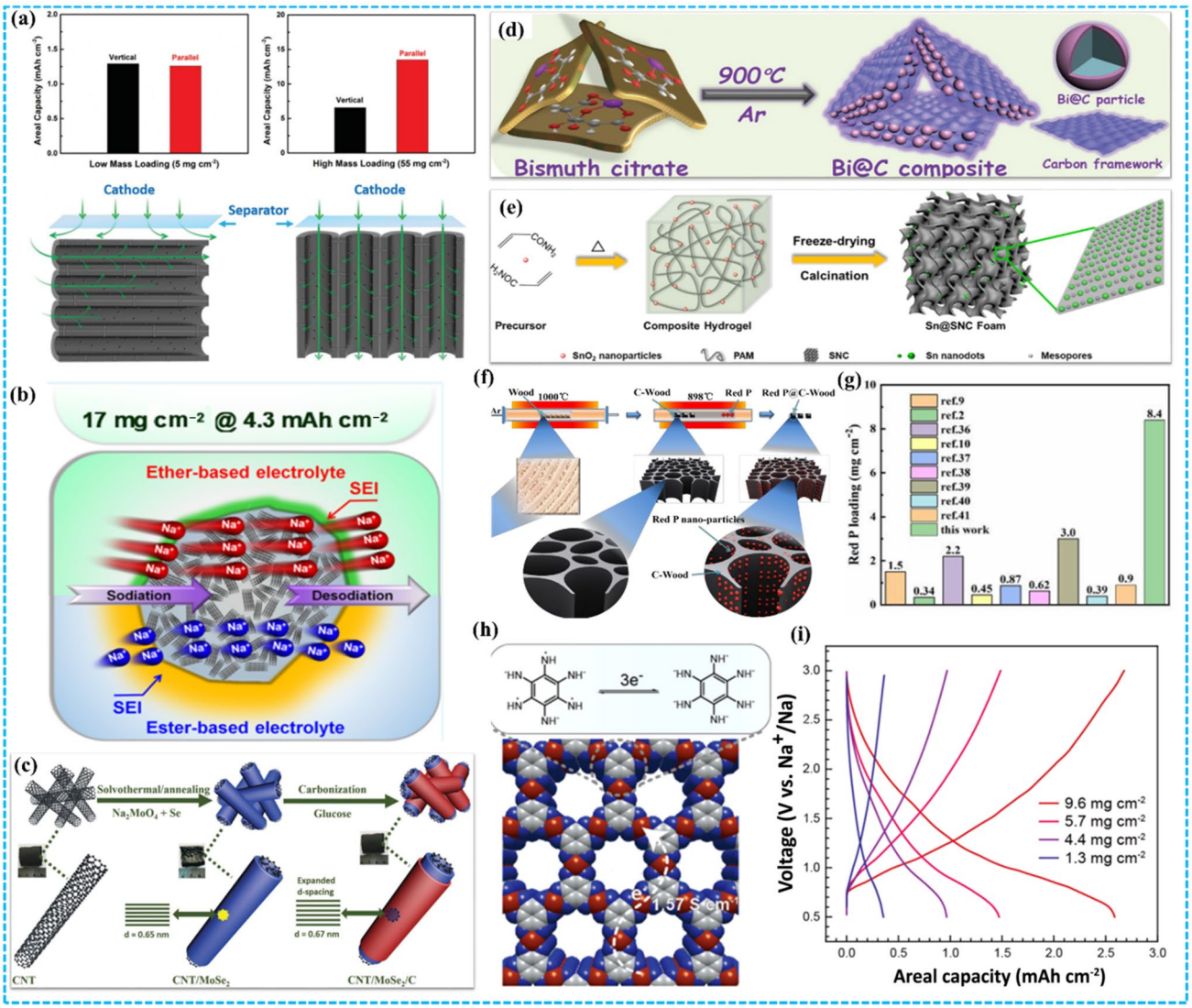

Fig. 13 **a** Sodium storage capacities of wood-derived hard carbon anodes with different cutting conditions. Reprinted with permission from Ref. [147]. Copyright © 2016, Wiley–VCH. **b** HMLE design and areal capacities based on hard carbons with different matching electrolytes, ether-based electrolytes and ester-based electrolytes. Reprinted with permission from Ref. [219]. Copyright © 2018, American Chemical Society. **c** Fabrication process of trilayered CNT/$MoSe_2$/C composite electrodes. Reprinted with permission from Ref. [148]. Copyright © 2019, Wiley–VCH. **d** One-pot synthesis of Bi@C composites. Reprinted with permission from Ref. [235]. Copyright © 2019, Wiley–VCH. **e** Illustration of the synthesis of porous Sn/C foam. Reprinted with permission from Ref. [106]. Copyright © 2019, Elsevier. **f**, **g** Phosphorus/WC composite electrodes and its mass loading. Reprinted with permission from Ref. [236]. Copyright © 2020, The Royal Society of Chemistry. **h** HMLE based on conductive HAB-MOFs for SIBs and **i** their areal capacities with different mass loadings. Reprinted with permission from Ref. [237]. Copyright © 2018, American Chemical Society

optimized electrode/electrolyte interfacial properties to further improve the cycling performance of high mass loading hard carbon anodes [219, 239].

Metals/alloys involving alloying reactions and metal oxides/sulfides/phosphides involving conversion reactions possess relatively high specific capacities and high energy densities [228, 240]. As a result, 2D transition metal dichalcogenides such as MoS_2 and $MoSe_2$ have attracted much attention due to layered structures with favorable electronic/chemical properties and mechanical stability [241]. And although MoS_2 electrodes usually show low sodium storage capacities, low mass loadings and poor cycling lifespans as a result of low conductivity and small interlayer spacing, $MoSe_2$ electrodes possess a higher theoretical capacity (~422 mAh g^{-1}) because of higher electrical conductivities and larger interlayer distances. Despite this, $MoSe_2$ electrodes also suffer from severe volume change. To mitigate these issues, percolating carbon networks with MoS_2/$MoSe_2$ to create hybrid heterostructures are promising (Fig. 13c). Using CNTs as an example, incorporated MoS_2/

CNTs or $MoSe_2$/CNTs hybrids generally possess multiple advantages, including: (1) heterostructures that possess free-standing, porous and interconnected networks that can provide mechanical strength to buffer volume variation during cycling and serve as highly conductive pathways for electron transfer and electrolyte penetration; (2) uniformly distributed MoS_2/$MoSe_2$ into carbon frameworks that can prevent the agglomeration and restacking of 2D layered structures; (3) protected carbon layers that can contribute to indirect contact between electrolytes and inner active materials; (4) hybrid MoS_2/CNTs or $MoSe_2$/CNTs structures that can enlarge the interlayer distance of the (002) planes of MoS_2/$MoSe_2$ to improve the bulk diffusivity of Na^+ ions; and (5) easy introduction of additional multilayered or monolayered carbon coatings that can further protect MoS_2/$MoSe_2$ [148, 224]. As a result of these combined effects, MoS_2/CNTs and $MoSe_2$/CNTs electrodes can enable advanced SIB performances to deliver areal capacities exceeding 6 mAh cm^{-2} at a mass loading of 15 mg cm^{-2} and 4 mAh cm^{-2} at a mass loading of 13.9 mg cm^{-2}. Other HMLEs based on metals/alloys such as Bi/C composites through the one-pot carbonization of bismuth citrate (Fig. 13d) that can deliver an areal capacity 280 mAh g^{-1} at a mass loading of 11.5 mg cm^{-2} [235], 3D Sn/C foam-like electrodes (Fig. 13e) that can deliver a reversible capacity of 1 mAh cm^{-2} at a mass loading of 20 mg cm^{-2} [106] and ultrathick electrodes based on red phosphorus encapsulated into WC (Fig. 13f) that can deliver a remarkable areal capacity of 18 mAh cm^{-2} at a mass loading of 8.4 mg cm^{-2} (Fig. 13g) [236] have also been reported.

Organic compounds with redox activity are also potential candidate electrode materials for next-generation batteries in which metal–organic frameworks (MOFs) are versatile and feasible platforms to store metal ions through electrochemical reactions provided by built-in active sites. Conductive MOFs are also promising electrode materials due to high electrical conductivities that can afford redox capability and stable cycling and have shown moderate activities in LIBs and SIBs [242, 243]. Despite this, conductive MOFs possess low redox-active center densities, which limit development in high energy and density electrodes. To address this, Bao et al. [237] prepared a unique 2D conductive MOF with cobalt ion nodes crosslinked by redox-active hexaaminobenzene (HAB) (Fig. 13h) and reported that the resulting optimized Co-HAB showed favorable electrical conductivities up to 1.57 S cm^{-1} and that the resulting electrode stored nearly three Na^+ ions per HAB in organic electrolytes, indicating high active center densities. As a result, the Co-HAB anode demonstrated both high rate responses and a high areal capacity of 2.6 mAh cm^{-2} under a high mass loading of 9.6 mg cm^{-2} (Fig. 13i). Despite this, many organic electrodes suffer from dissolution in electrolytes, inferior reaction kinetics, weak stability and low electrical conductivity, all of which hinder storage capacity and cycling stability, and therefore, the realization of practical organic electrode application requires significant effort.

4.2.2 Cathode Modification

Na-based metal oxides, Na_xMO_2 (M = Co, Mn, Fe, etc.), are also promising cathode materials for reversible Na^+ ion intercalation and possess high redox potentials and high theoretical capacities [248]. Based on this, layered Na_xCoO_2 has been widely studied because of the referenced success of its analogue $LiCoO_2$ in LIBs. However, Na_xCoO_2 cathodes suffer from serious structural deterioration and capacity fading due to complex phase transitions during cycling related to the intercalation of large Na^+ ions and Na^+/vacancy ordering [249], which can lead to unfavorable performances in HMLEs in which most studies on SIB cathodes have reported low mass loadings between 0.5 and 2 mg cm^{-2} [245]. Here, Yang et al. [244, 245] proposed the fabrication of self-supported Na_xCoO_2 with an open arrayed nanostructure through direct growth onto a conductive nickel foam substrate (Fig. 14a, b) in which the binder-free feature can allow for improved electrical conductivity whereas the open framework can provide adequate spacing to accommodate volume expansion, allowing for the high mass loading of Na_xCoO_2 cathodes ranging from 8 to 10 mg cm^{-2} and corresponding areal capacities of 1.16–1.66 mAh cm^{-2}. And although Na_xMO_2 cathode materials are further impeded by irreversible structural collapse and capacity degradation due to multiple phase/structural variations, they can sustain Na extraction without phase transition [250]. Based on this, improvements to $NaMnO_2$ cathodes are focused on promoting capacity to achieve high energy density. Here, structural modifications of chemical composition and lattice structure through the partial substitution of elements or metal doping have been demonstrated to be effective [251]. Mai et al. [246] developed a composite structured $xNa_4Mn_2O_5{\cdot}(1-x)Na_{0.7}MnO_2$ cathode that possessed synergistic advantages based on varying phases/composition (Fig. 14c) to show improved sodium storage performances in which an optimized $0.44Na_4Mn_2O_5{\cdot}0.56Na_{0.7}MnO_2$ cathode featured a stable crystal skeleton structure and a high capacity of 1.3 mAh cm^{-2} at a mass loading of 8.19 mg cm^{-2} (Fig. 14d) as well as high capacity retention of 85% at 500 mA g^{-1} after 200 cycles in a full SIB.

Polyanionic compounds such as $NaFePO_4$ and $Na_3V_2(PO_4)_3$ are also fascinating cathode materials due to high structural stability and high operating voltages [252, 253]. However, low intrinsic electronic conductivities as a result of electrically insulating phosphate components isolating transition metal valence electrons hinder rate performance in corresponding HMLEs [247]. To address this, researchers have proposed the construction of highly conductive and porous networks to couple with these materials

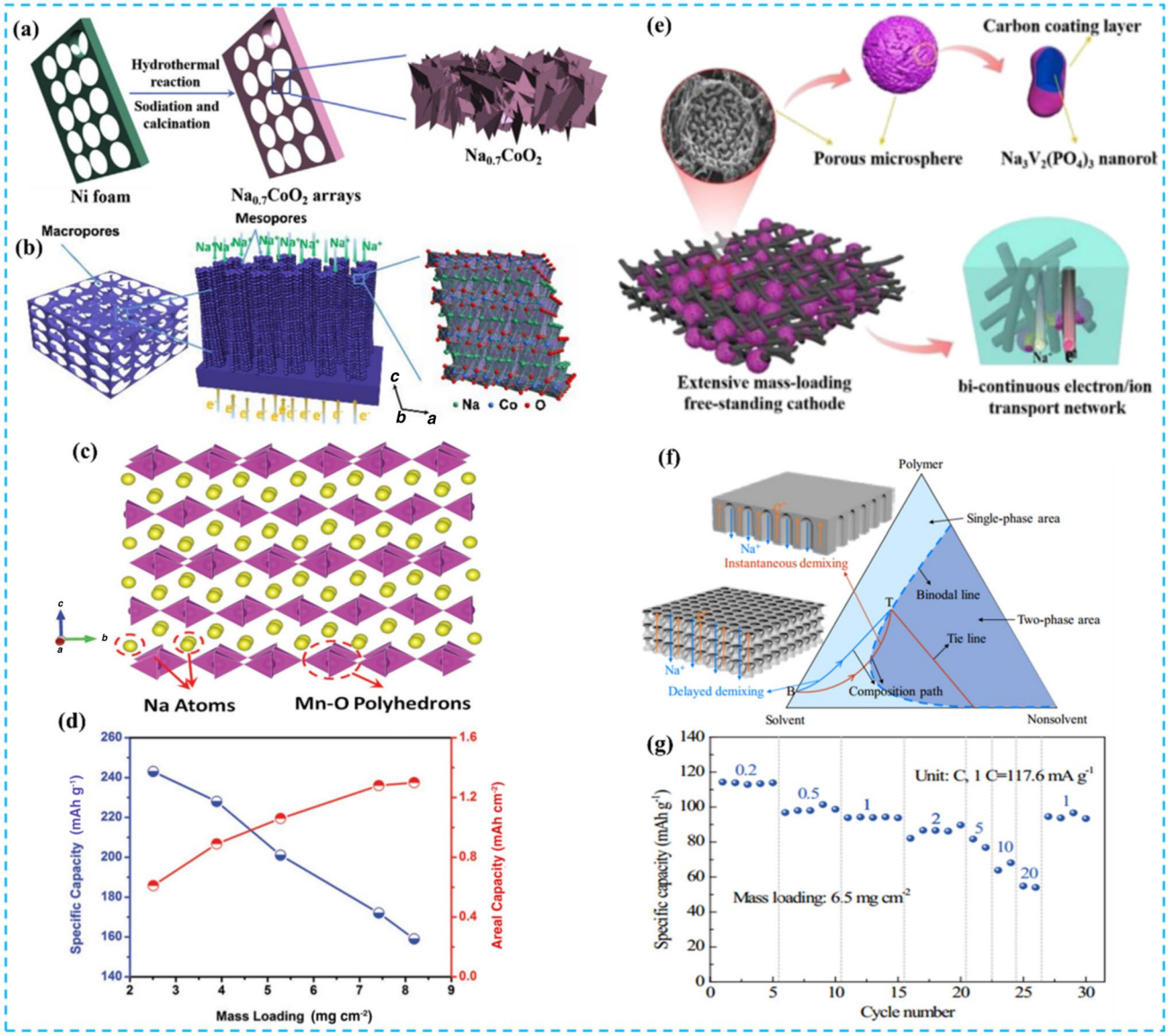

Fig. 14 **a**, **b** Fabrication process of Na_xCoO_2 arrays. Reprinted with permission from Ref. [244], Copyright © 2018, Elsevier; and Ref. [245], Copyright © 2019, Wiley–VCH. **c** Crystal structure of a Na-Mn–O composite and **d** the specific capacities and areal capacities of $0.44Na_4Mn_2O_5{\cdot}0.56Na_{0.7}MnO_2$ electrodes with various mass loadings. Reprinted with permission from Ref. [246]. Copyright © 2018, Wiley–VCH. **e** Preparation of an NVP/CNF composite network electrode. Reprinted with permission from Ref. [247]. Copyright © 2020, American Chemical Society. **f** Phase separation in the fabrication of vertical-aligned porous NVP/C composite electrodes and **g** corresponding rate capability. Reprinted with permission from Ref. [52]. Copyright © 2019, The Royal Society of Chemistry

to provide smooth electron/ion conduction at the electrode scale [254]. For example, Li et al. [247] designed freestanding electrodes consisting of 3D interwoven carbon nanofibers encapsulated with porous NVP/C microspheres (Fig. 14e) that provided high electrical conductivity and easy electrolyte penetration as a result of the interconnected and porous network structure in which the corresponding electrode delivered a specific capacity of 62.2 mAh g^{-1} at 40 C under a mass loading of 8 mg cm^{-2}. Li et al. [52] also prepared a freestanding electrode by loading NVP into a carbon matrix with vertically aligned pores through phase separation in which phase separation is a flexible and simple method to engineer carbon framework pore structures through the addition of suitable salts or regulation solvent systems (Fig. 14f). In this study, these researchers comprehensively studied the influences of three non-solvent components (water, ethanol and water vapor) in the polymer–solvent–nonsolvent system on the microstructure of the obtained carbon membranes with different porous structures and reported that among these, only the ethanol phase

separation-derived samples showed sponge-like cross sections and porous structures in both top and bottom surfaces to form a completely open structure that can improve ion diffusion efficiency. As a result, a self-standing 500-μm-thick NVP cathode delivered specific capacities of 113.7 mAh g^{-1} at 0.2 C and 54.4 mAh g^{-1} at 20 C under a mass loading of 6.5 mg cm^{-2} (Fig. 14g). These simple yet effective strategies for pore structure engineering are attracting increasing attention and can be applied to various carbon electrodes for diverse batteries.

4.3 Potassium-Ion Batteries

Potassium-ion batteries (PIBs) are another alternative to LIBs in next-generation EESSs because of the inexpensive and abundant resource of potassium (17000 μmol mol^{-1}). Moreover, the low redox potential of K^+/K (− 2.93 V vs. standard hydrogen potential) that is close to Li^+/Li (− 3.04 V vs. standard hydrogen potential) suggests that PIBs can operate at high potentials and possess high energy densities [255]. K^+ ions can also insert into commercial graphite to form graphite intercalation compounds (KC_8) at a relatively high insertion potential to allow for a theoretical capacity of 279 mAh g^{-1} [256]. However, PIBs are hindered by the large ionic radius of K^+ (1.38 Å), which can lead to the insufficient intercalation of ions in crystal structures and large volume expansion during operation. These issues worsen in HMLEs due to undesirable charge kinetics and poor structural stability. Here, the construction of stable SEI layers onto electrodes is an effective method to improve PIB performance [257]. Lu et al. [258] constructed high performance PIBs based on HMLEs through electrolyte engineering and optimization. Based on this, these researchers reported that although traditional low concentration hexafluorophosphate-based electrolytes generally result in solvent decomposition to form organic-rich SEI layers and low electrode protection efficiency [259], the innovative use of the concentrated $KN(SO_2F)_2$/ethyl methyl carbonate (with a molar ratio of KFSI:EMC = 1:2.5) electrolyte as a substitute can establish highly effective inorganic-rich SEI layers on graphite electrodes to suppress the structural change of graphite during charge/discharge. Comprehensive experiments also showed that SEI formation mainly occurred at high potentials in KFSI concentrated electrolytes rather than

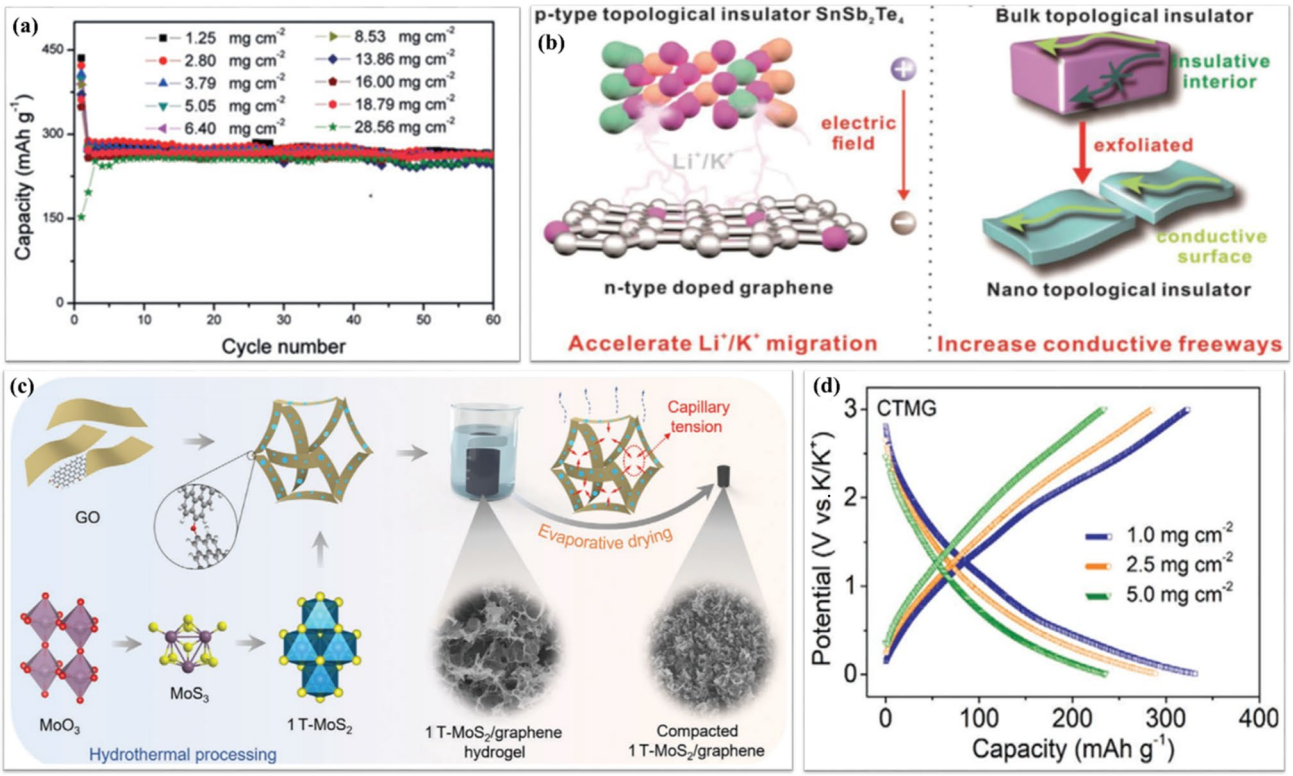

Fig. 15 **a** Cycling performances of high mass loading graphite anodes with different mass loadings for PIBs. Reprinted with permission from Ref. [258]. Copyright © 2019, Wiley–VCH. **b** Schematic for accelerated Li^+/K^+ migration kinetics in $SnSb_2Te_4$/graphene electrodes as a result of the construction of an interface electric field and **c** conductive topological surfaces from bulk to nano. Reprinted with permission from Ref. [260]. Copyright © 2020, Wiley–VCH. **c** Preparation process of a densely compacted 1 T-MoS_2/graphene electrode and **d** its specific capacities at different mass loadings. Reprinted with permission from Ref. [261]. Copyright © 2020, Wiley–VCH

at low potentials for KPF_6 traditional electrolytes, allowing the graphite anodes of PIBs to operate stably for over 2000 cycles and deliver a high areal capacity of 7.36 mAh cm^{-2} at 1/14 C with over 90% capacity retention after 60 cycles at a high mass loading of 28.56 mg cm^{-2} (Fig. 15a). A full cell assembled with an annealed perylene-3,4,9,10-tetracarboxylic dianhydride (PTCDA) cathode with a mass loading of 4.0 mg cm^{-2} and a graphite anode with a mass loading of 2.3 mg cm^{-2} further achieved a capacity of 80 mAh g^{-1} at 30 mA g^{-1} and 92.9% capacity retention after 50 cycles.

The materials-science concept of exploring novel AMs to improve HMLE performance is also efficient. For example, Guo et al. [260] rationally designed hybrid heterostructured materials composed of p-type topological insulator $SnSb_2$ nanodots anchored onto few-layered graphene (denoted as $SnSb_2Te_4$/G) and reported synergistic effects including: (1) highly doped few-layer graphene that can provide ultrafast surface pseudocapacitance and acted as buffer layers to accommodate volume expansion; (2) $SnSb_2Te_4$ that can create abundantly exposed conductive topological surfaces to improve electron delivery; and (3) strong coupling effects between $SnSb_2Te_4$ and graphene that can establish localized built-in electrical fields to promote directional ion migration at the interface (Fig. 15b). Despite these results, this study only pioneered this ideal electrode for HMLEs in LIBs. However, such hybrid electrodes with efficient synergetic effects are also beneficial to HMLEs in PIBs and should be explored in the near future. Alternatively, Huang et al. [261] synthesized a 3D hydrogel through the assembly of 1 T-MoS_2 and graphene oxide that was tightened into compact electrodes by capillary drying (Fig. 15c) and reported that the densely compact yet porous 3D network structure of the 1 T-MoS_2/GO electrode enabled a high potassium capacity of 235 mAh g^{-1} at a high mass loading of 5 mg cm^{-2} (Fig. 15d) as well as a high volumetric capacity of 467 mAh cm^{-3} at 0.1 A g^{-1} under a mass loading of 2.5 mg cm^{-2}. Overall, many advanced HMLEs strategies of LIBs are valid for PIBs due to similar functional mechanisms.

4.4 Lithium Metal Batteries

4.4.1 Lithium Metal Anodes

Over the past decades, lithium metal anodes (LMAs) have gained intensive interest with the growing need for large-scale, high energy storage devices because LMAs possess an extremely large theoretical capacity of 3860 mAh g^{-1} and a low reduction potential of − 3.04 V versus SHE [266]. Despite this, LMAs experience serious obstacles including: (1) Li dendrite formation that can result in internal short circuiting along with poor battery safety; and (2) "dead" Li generation and constant SEI layer buildup/breakdown due to significant dimensional change and unstable Li/electrolyte interfacial chemistry that can lead to additional Li consumption and poor coulombic efficiency [267, 268]. To address these issues, strategies to obtain dendrite-free LMAs have been extensively explored, with examples including electrolyte engineering [269], polymer separator surface modification [270], the use of 3D current collectors [271], the coating of protective layers onto Li metal surfaces or current collectors [272, 273] and the use of highly concentrated salt or fluorinated solvents [274]. Among these hybrid LMAs through the incorporation of metallic Li into 3D porous conductive scaffolds are promising, particularly to eliminate LMA volume change. However, conventional 3D conductive metal current collectors (e.g., Cu or Ni foam) are generally too heavy to achieve high energy density in corresponding batteries due to low metallic Li mass loadings [262]. To this end, the development of LMAs with high metallic Li mass loading into low-weight-ratio and conductive 3D hosts is vital.

As an example of an LMA, nanowire-based metal current collectors (NMCCs) are alternative 3D Li-hosts that are lightweight and highly conductive. However, NMCC surfaces are usually lithiophobic, which can lead to high Li nucleation barriers and cause uneven Li deposition. Here, the surface modification of NMCCs with molecules such as Si, ZnO, CuO, and Sn is an effective strategy to introduce low nucleation barriers for uniform Li deposition [275, 276]. More importantly, the electronic/ionic conductivity of NMCCs can be carefully tuned through surface modification. For example, Kang et al. [262] fabricated a copper nanowire-phosphide (CuNW-P) host with high electrical conductivity through modification with Cu_3P gradients along the cross section of the current collector (Fig. 16a) and reported that the strong interactions between lithiophilic Cu_3P and metallic Li can induce a desirable hybrid electrode with a high Li ion conductivity of 10^{-4} S cm^{-1} that allowed for homogeneous Li ion flux on the electrode surface. As a result, the CuNW-P host enabled dense and stable Li deposition not only on the outside conductive fields of its surface, but also in the inner pores with a perpendicularly oriented coverage texture throughout the current collector. In addition, a corresponding CuNW-P/Li half-cell exhibited stable cycling performances at 1 mA cm^{-2} and 1 mAh cm^{-2} for over 1000 cycles and a composite electrode with a high Li mass loading of 44% resulted in a capacity of 3 mAh cm^{-2} at 1 mA cm^{-2}, which corresponded to high gravimetric and volumetric capacities of 1703 mAh g^{-1} and 1582 mAh cm^{-3} respectively. Further morphological evaluations after cycling revealed that the surface and cross section of the CuNW-P/Li anode possessed a perpendicularly oriented texture of Li metal and that the bottom of the anode possessed a flat and dense surface, thus indicating the good reversibility of dense Li nucleation and the full utilization of CuNW-P

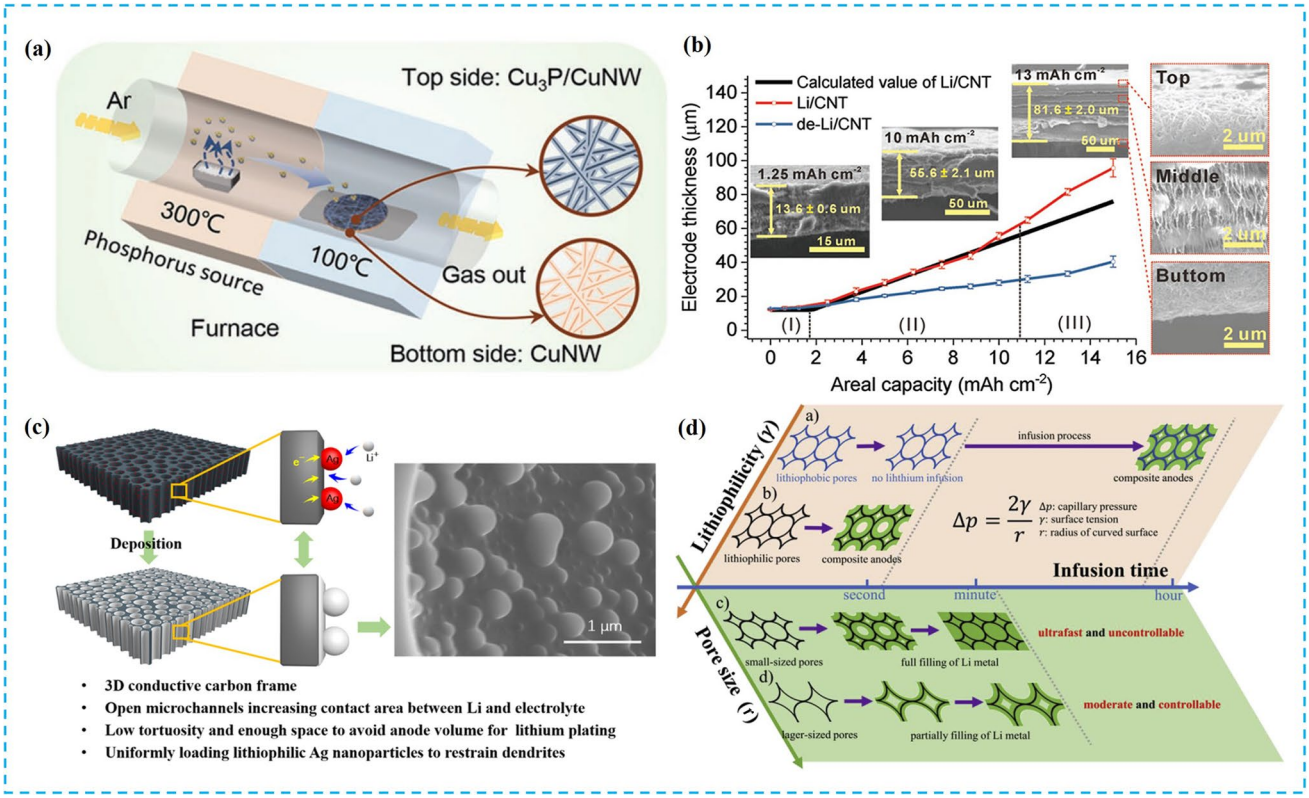

Fig. 16 **a** Schematic of the formation and phosphidation of Cu nanowire current collectors. Reprinted with permission from Ref. [262]. Copyright © 2018, Wiley–VCH. **b** Electrochemical performances of Li/CNT anodes with different thicknesses using expandable CNT scaffolds; the inset shows SEM images of cross sections of Li/CNT anodes with different Li loadings. Reprinted with permission from Ref. [263]. Copyright © 2018, Wiley–VCH. **c** Wood derived carbon scaffold for dendrite-free LMAs. Reprinted with permission from Ref. [264]. Copyright © 2019, American Chemical Society. **d** Regulating capillary pressure to achieve the controllable Li-content in composite LMAs. Reprinted with permission from Ref. [265]. Copyright © 2019, Elsevier

inner spacing and allowing a full cell based on the CuNW-P/Li anode and an LFP cathode at a high mass loading of 10 mg cm^{-2} to possess stable cycling performances.

Porous carbon skeletons are another lightweight host that can accommodate more Li metal than metal current collectors in which to improve Li loading and utilization, Ji et al. [263] used ultralight yet mechanically robust CNT paper to host Li metal at an extremely large mass fraction of 80.7%, which was achieved by the highly porous structure of the CNT paper with ~73 vol% void spacing to accommodate Li metal. Moreover, CNT paper possesses an excellent electrical conductivity of 1.1×10^5 S m^{-1} that can contribute to lowered local current densities for Li-plating/stripping in which a resulting Li/CNT electrode demonstrated a maximum areal capacity of 13 mAh cm^{-2} and a remarkable Li utilization of 90.9% over 1000 cycles (Fig. 16b). Here, these researchers attributed such outstanding cycling performances to the expandable and robust CNT paper with adequate void spacing that can buffer large volume expansion. Biomass-derived 3D porous frameworks are also promising hosts due to their cost-effectiveness and natural abundance. Based on this, Hu et al. [277] used carbonized wood (CW) decorated with a lithiophilic ZnO layer to load metallic Li and reported that due to high porosity and well-aligned channels, Li plating/stripping can be effectively processed into directional channels with uniform Li nucleation and growth. In addition, adequate void spacing in the material can hinder volume change during cycling, allowing a 500-μm-ultrathick Li/CW electrode at a Li-metal mass loading of 28 mg cm^{-2} to deliver a low overpotential of 90 mV at 3 mA cm^{-2} and long cycling performances of 150 h at 3 mA cm^{-2}. Liao et al. [264] also used a CW frame decorated with Ag nanoparticle seeds to obtain an 800-μm-thick Li/CW-Ag composite anode (Fig. 16c) that stably operated for over 450 h at 1 mA cm^{-2} with 1 mAh cm^{-2} and 300 h at 3 mA cm^{-2} with 3 mAh cm^{-2}, demonstrating that the use of naturally lightweight and porous wood precursors to fabricate CW frames can allow for the high mass Li metal loadings. However, CWs such as balsawood (one of the lightest wood materials in the world) have yet to be investigated [264].

Alternatively, Li metal loadings that are much higher than required can jeopardize cell energy density and therefore

Li loading in composites needs to be precisely controlled, but faces great challenges. Based on this, Liu et al. [265] analyzed parameters related to capillary pressure on molten Li using the Young–Laplace equation (Fig. 16d) and found that the regulation of pore size and surface properties of 3D hosts can allow for appropriate capillary pressure to control the Li metal content in which 3D hosts with relatively large-sized pores can decrease capillary pressure to slow

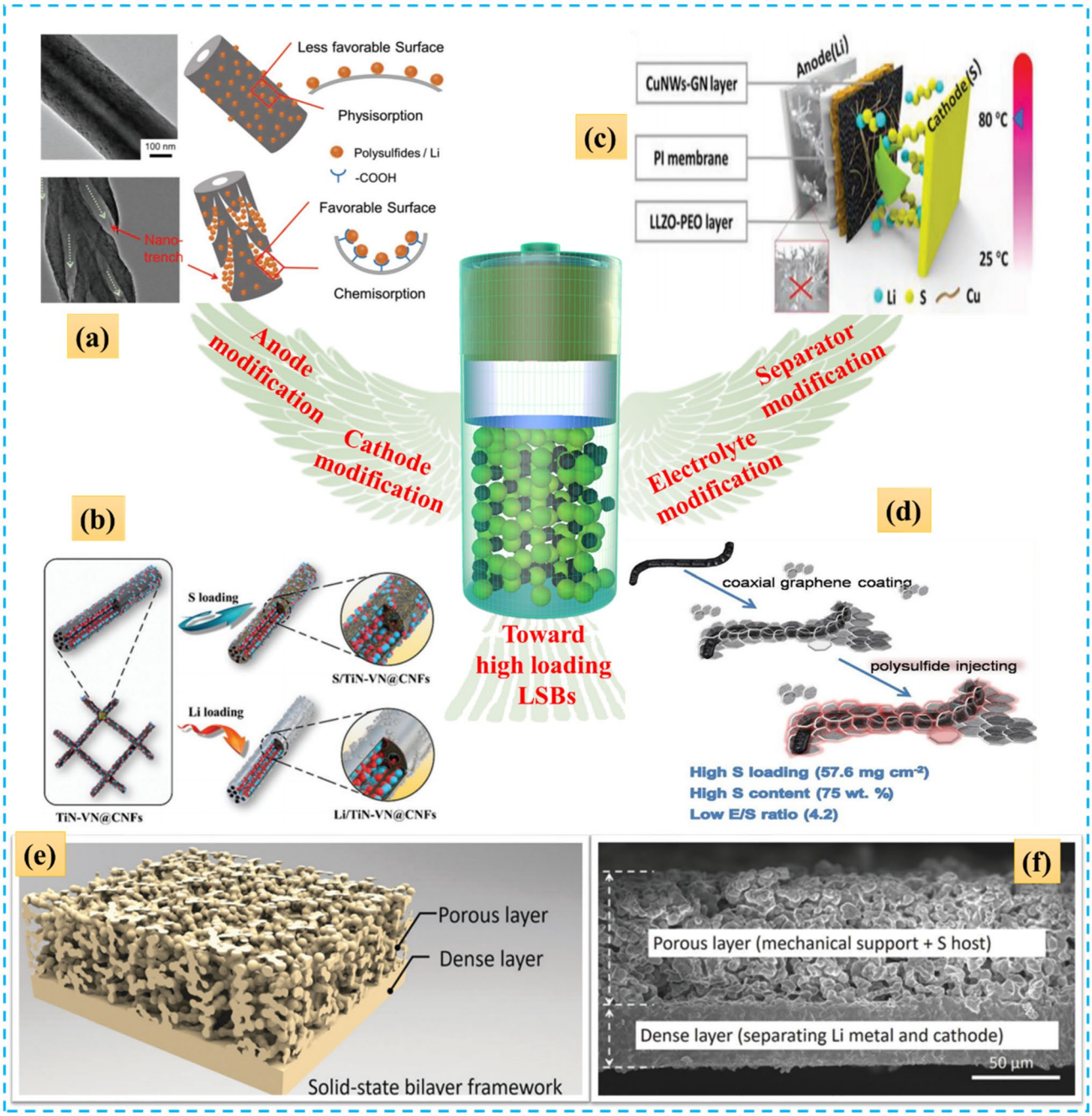

Fig. 17 **a** CNT sponge with a trench-wall structure that can act as a reactor to host polysulfides and lithium. Reprinted with permission from Ref. [278]. Copyright © 2018, Wiley–VCH. **b** Synthesis of flexible carbon nanofibers with embedded TiN-VN heterostructures as hosts for S cathodes and Li anodes. Reprinted with permission from Ref. [279]. Copyright © 2020, Wiley–VCH. **c** LSB configuration based on a multifunctional separator. Reprinted with permission from Ref. [280]. Copyright © 2020, Wiley–VCH. **d** Electrolyte optimization: the high S-loading LSB with a low electrolyte/sulfur ratio. Reprinted with permission from Ref. [281]. Copyright © 2018, Elsevier. **e** 3D bilayer garnet solid electrolyte enabling high sulfur loading for all-solid-state Li–S batteries, and **f** corresponding SEM image. Reprinted with permission from Ref. [282]. Copyright © 2017, The Royal Society of Chemistry

down Li infusion and allow for the careful regulation of the Li loading content and Li coverage. Based on this, these researchers used ultralight 3D graphene foam with lithiophilic ZnO nanoparticles (3D-G@ZnO) as a Li host due to its lightweight, easy modification and large-sized pores for molten Li infusion control and were able to quantitatively load Li metal from 1.8 to 9 mg cm^{-2} by changing the decoration amount of ZnO in which the areal capacities of 3D-G@ZnO/Li increased from 5.17 to 24.63 mAh cm^{-2} with increasing ZnO decoration. This composite anode can also be successfully paired with many cathodes under high mass loadings (10 mg cm^{-2}) to construct full cells with stable cycling performances.

4.4.2 Li–S Batteries

Li–S batteries (LSBs) represent one of the most promising alternatives for next generation high-energy EESSs due to a unique electrochemical mechanism involving multi-electron conversion electrochemistry through the combination of LMAs and sulfur cathodes with high gravimetric capacities of 1672 and 3860 mAh g^{-1} respectively [283]. However, these promising systems are limited by intrinsic drawbacks such as electronically insulating cathode materials, soluble lithium polysulfide (LiPS) intermediates, severe cathode volumetric change, uncontrollable lithium dendrite formation and unstable SEI layers [284]. In addition, low areal sulfur mass loadings (< 2.0 mg cm^{-2}) severely hinder the practical application of LSBs [283]. To obtain high-loading LSBs with high areal capacities, tremendous efforts have been devoted to the modification and optimization of anodes, cathodes, separators and electrolytes (Fig. 17).

Among various LSB anode materials, LMAs represent the most promising choice due to advantages as mentioned above. However, corresponding dendrite growth, unstable SEI formation, serious lithium metal corrosion and electrolyte decomposition all restrict the application of pure LMAs for LSBs in which for S cathodes, unavoidable volume expansion and huge compression force from cell packing will lead to structural instability as well as capacity fading and poor cycling performance [285]. One proposed solution to address this involves the use of 3D Li hosts and sulfur hosts to construct high-loading full LSBs with stable electrochemical performances in which the fabrication of 3D hosts that can match with both Li and S is more promising because of simplified and cost-effective processes. For example, Yu et al. [278] fabricated a CNT sponge host with unique spiral trenches on the CNT surface to simultaneously provide favorable polysulfide-philic surfaces for cathodes and lithiophilic surfaces for anodes (Fig. 17a) in which the abundant nanotrenches on the CNT walls can impede polysulfide shuttling and improve lithium deposition/stripping to decrease both interfacial and charge transfer resistances. As a result, an LSB constructed with high S loadings up to 10 mg cm^{-2} can produce a remarkable areal capacity of 13.3 mAh cm^{-2} at 1.6 mA cm^{-2} as well as good rate performances with 11 mAh cm^{-2} being maintained at 16 mA cm^{-2}. Luo et al. [279] also developed a dual-functional carbon nanofiber host embedded with TiN-VN heterostructures (CNF@TiN-VN) to simultaneously load sulfur and regulate lithium deposition/stripping (Fig. 17b) in which the well dispersed TiN-VN nanoparticles can result in good conductivity and surface polarization in the CNF@TiN-VN to contribute to strong adsorption and high conductivity, thus hindering shuttling effects and enhancing electrochemical conversion. The lithiophilic surface of CNF@TiN-VN can also allow for homogenous Li deposition and dendrite suppression, resulting in a corresponding full LSB with a high sulfur loading of 5.6 mg cm^{-2} to deliver a high areal capacity of 5.5 mAh cm^{-2} at 0.1 C and stable cycling performances for 100 cycles. Despite these results, full LSBs involving LMAs and high-loading S cathodes as 3D hosts remain underdeveloped, which encourages future efforts to resolve key issues.

Separators are generally applied to separate anodes from cathodes to prevent cell short circuiting in which ideal separators should possess more functionalities to meet the requirements of stable LSBs with long cycling lifespans such as the suppression of the shuttling effect, good compatibility and contact with anodes/cathodes and being intrinsically electrochemically inert [283]. Here, the coating of separators with additional functional layers is an effective method to achieve these requirements. For example, Zhao et al. [280] engineered a sandwich structured multifunctional separator that included an inner layer of polyimide (PI) membrane coated with copper nanowire-graphene nanosheets (CuNWs-GN) and rigid lithium lanthanum zirconium oxide-polyethylene oxide(LLZO-PEO) films on the opposite side (Fig. 17c) in which the CuNWs-GN layer can block LiPS through physical confinement and chemical anchoring/transformation whereas LLZO-PEO can suppress Li dendrite formation, allowing the core PI layer to possess strong dimensional stability, flame-retardant ability and outstanding electrolyte affinity. As a result, a full LSB with a pure sulfur loading of 3 mg cm^{-2} showed stable cycling performances in which reversible capacities of 817.8 and 353.9 mAh g^{-1} at 0.5 A g^{-1} were achieved after 50 and 300 cycles respectively. This system also performed well at an elevated temperature of 80 °C with an initial capacity of 1402.1 mAh g^{-1} at 0.1 A g^{-1}, demonstrating potential for practical application.

Electrolyte modification is also important in the development of high performance LSBs because of the corresponding dissolution of polysulfides and the availability of ionic media for working cells [285]. However, electrolyte modifications also require a high electrolyte content (a high E/S ratio) in LSBs to compensate for the decreased conductivity

and uncontrolled physicochemical deterioration of electrolytes resulting from dissolved polysulfides in which high E/S ratios can impede the high energy density of LSBs. Because of this, the control of the electrolyte content in LSBs to balance energy/power density and cycling capability is important. For example, Manthiram et al. [281] comprehensively studied the influences of E/S ratios on LSB cell performance at an ultrahigh S loading of 57.6 mg cm^{-2} as a result of the use of a coaxial-graphene-coated cotton-carbon cathode substrate with open channels combined with an electroactive polysulfide catholyte (Fig. 17d) through controlled E/S ratio experiments (6, 5.4, 4.8 and 4.2 μL mg^{-1}) and reported that a high mass-loading LSB can display high initial gravimetric, volumetric and areal capacities of 408 mAh g^{-1}, 523 mAh cm^{-3} and 31 mAh cm^{-2} respectively and a good cycling retention capacity of 20.5 mAh cm^{-2} after 200 cycles. Apart from electrolyte ratio optimizations, the modification of Li salts and solvents in electrolytes can also effectively achieve long-term cycling performance in which an –OH functionalized cellulose polymer electrolyte contributed to a high areal capacity of 5.1 mAh cm^{-2} for an LSB due to the –OH groups acting as a polysulfide binder through polar–polar interactions [286]. These aspects have already been systematically reviewed in literature [285, 287], therefore, this review will only provide a brief introduction.

To avoid short-circuiting and fire in conventional batteries based on aqueous electrolytes, non-flammable solid-state electrolytes (SSEs) have attracted tremendous attention [288, 289]. Here, SSEs can be divided into inorganic solid electrolytes (ISEs) with high ionic conductivity and excellent mechanical rigidity as well as solid polymer electrolytes (SPEs) with compatible interfacial contact but weak mechanical strength [290] in which ideal SSEs should possess: (1) appropriate mechanical moduli to suppress Li dendrite growth; (2) high ionic conductivity for efficient ion migration [291]; (3) good compatibility with electrodes for low interfacial resistance; and (4) rational structures to inhibit liquid electrolyte leakage [292]. For example, Yan et al. [293] addressed a core concern involving interfacial connections between electrolytes and electrodes by designing a functional gradient SPE that was integrated with a ceramic-rich phase with a high modulus of 6.67 GPa and a polymer-rich phase with good interfacial compatibility in which the ceramic-rich phase can act as a physical barrier to suppress Li dendrite formation whereas the polymer-rich phase can improve cathode/electrolyte interfacial affinity. Garnet type electrolytes (GTEs) are also a type of ISEs with high ionic conductivity, adequate mechanical strength and high chemical/electrochemical stability in which to improve the mass loading and full utilization of GTEs. Hu et al. [282] meticulously designed a 3D bilayer solid state electrolyte framework with a thin but dense layer in the bottom and a porous thick layer on the top (Fig. 17e). Here, the thin layer can serve as a separator with a high elastic modulus for anode/cathode partition and Li dendrite suppression whereas the thick layer can provide adequate spacing to confine electrode volume change and high sulfur mass loadings of up to 7.5 mg cm^{-2} to completely form an "all-in-one" integrated battery design (Fig. 17f) that can improve interfacial interconnections between dense and porous layers to provide sufficient electronic and ionic conductive highways, allowing a full cell to deliver a device-level energy density of 248.2 Wh kg^{-1} and superior average coulombic efficiency larger than 99% for each subsequent cycle. Promisingly, this "all-in-one" integrated structure can also be extended to other electrode materials to obtain advanced HMLEs.

4.4.3 Lithium-Air Batteries

Lithium-air batteries (LABs) using LMAs and O_2 or CO_2 cathodes are promising half-open EESSs with high theoretical energy densities in which aside from key issues involving LMAs, the major bottlenecks of LABs stem from sluggish electrochemical kinetics in air cathodes and the adverse accumulation of insoluble discharge products on cathode surfaces that can block Li^+ and air diffusion [294]. Based on this, current research is mainly focused on the enhancement of LAB performance through AM design and electrode structural engineering in which although numerous cathode materials possess high gravimetric performances, corresponding mass loadings are rarely larger than 1 mg cm^{-2} [295]. Here, electrode structural regulation is a promising method to improve LAB performance based on the practical demands of HMLEs and the necessity for efficient Li^+/air diffusivity through electrodes as well as adequate void spacing to host solid discharge products [296].

3D frameworks with abundant macro-/mesopores and large volume sizes are advanced conductive scaffolds for AM loading that can facilitate oxygen diffusion and provide sufficient cavities to accommodate Li_2O_2 [296]. Based on this, 3D CNT monoliths and holey graphene are interesting candidates to enhance performance due to well-designed open structures and high conductivities. For example, Lee et al. [297] prepared separator-CNT-based monolithic electrodes to achieve mass loadings of 14–15 mg cm^{-2} (Fig. 18a) in which the electrodes allowed for highly effective contact between the separator and the active layers as well as highly conductive and porous networks for efficient charge transport, allowing a monolith electrode without catalyst decoration to display a high discharge areal capacity of 102.48 mAh cm^{-2} at 0.5 mA cm^{-2} with a voltage cutoff of 2.3 V (Fig. 18b). Decoration with a RuO_2/MnO_2 bifunctional catalyst further facilitated the decomposition of Li_2O_2 and the completely removal of Li_2CO_3 and LiOH byproducts to contribute to excellent cycling stability. Holey graphene (HG) as a unique porous material with atomic thickness

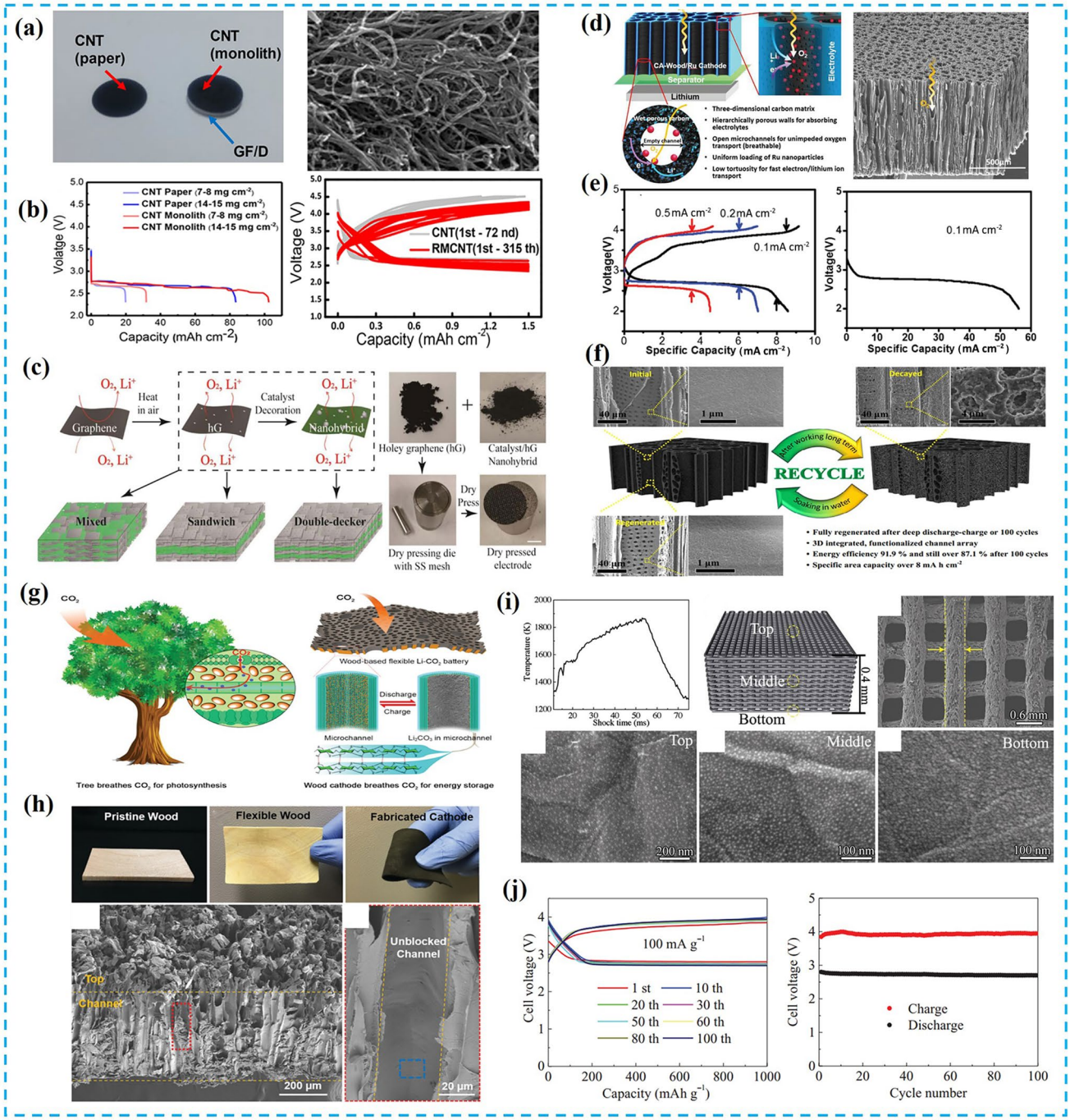

Fig. 18 **a** Photographs of CNT paper and the separator-CNT monolith, **b** full galvanostatic discharge profiles of CNT-paper and separator-CNT monolith electrodes with different mass loadings and their voltage profiles for cycling tests. Reprinted with permission from Ref. [297]. Copyright © 2018, American Chemical Society. **c** Dry press method to create ultrathick HG-based electrodes with distinct structures for Li-O_2 batteries. Reprinted with permission from Ref. [298]. Copyright © 2017, Elsevier. **d** Schematic of thick cathodes based on wood carbon decorated Ru for Li-O_2 batteries and **e** charge/discharge curves. Reprinted with permission from Ref. [296]. Copyright © 2018, Wiley–VCH. **f** Schematic of a RuO_2/wood carbon cathode for Li-O_2 batteries. Reprinted with permission from Ref. [299]. Copyright © 2018, The Royal Society of Chemistry. **g** Schematics showing a natural wood-inspired Li-CO_2 battery design. **h** Morphology and microstructure of a flexible wood cathode structure. Reprinted with permission from Ref. [300]. Copyright © 2018, The Royal Society of Chemistry. **i** Microstructure of a 3D-printed graphene electrode with ultrafine Ni nanoparticle encapsulation for a Li-CO_2 battery and **j** corresponding battery performance. Reprinted with permission from Ref. [301]. Copyright © 2018, Wiley–VCH

in-plane hole arrays distributed evenly across lateral graphene sheets can also facilitate ion transport through electrodes. For example, Hu et al. [298] used HG as a catalyst-decorated freestanding air cathode in Li-O_2 batteries and reported that nanosized through-holes and the layered configuration allowed for the compression of HG sheets into ultrathick electrodes with high mass loadings (Fig. 18c) in which novel mixed and stacked HG cathodes were successfully cycled at 0.2 mA cm^{-2} to achieve areal capacities of 23.8, 28.9 and 42 mAh cm^{-2} for different mass loadings of 11, 17, and 28 mg cm^{-2}, respectively.

Inspired by natural wood with a 3D hierarchical porous structure and elongated microchannels, Hu et al. [296] further applied wood carbon in LABs in which a 700-μm-thick cathode derived from activated wood carbon (AWC) decorated with Ru nanoparticles was fabricated (Fig. 18d) to deliver a superior areal capacity of 8.58 mAh cm^{-2} at 0.1 mA cm^{-2} and outstanding rate capability with 4.51 mAh cm^{-2} at 0.5 mA cm^{-2} (Fig. 18e). These researchers also reported that due to excellent air permeability, the Ru/AWC electrode showed a remarkable areal capacity of 56 mAh cm^{-2} at 0.1 mA cm^{-2} as the Ru coating thickness increased to 3.4 nm, demonstrating the positive influences of the advanced AWC cathode structure, including: (1) open and low-tortuosity microchannels that can contribute to efficient oxygen gas diffusion within the ultrathick electrode; and (2) a porous structure that can trap electrolytes to establish stable and continuous electrolyte layers for rapid Li ion transfer without the blocking of oxygen gas to form large amounts of well-balanced triple-phase active sites for enhanced electrochemical reactions. Song et al. [299] extended this strategy to further enhance the cycling performance and energy efficiency of Li-O_2 batteries through the modification of AWC with RuO_2 (Fig. 18f) in which the resulting 650 μm thick RuO_2/AWC electrode provided an areal capacity of 8.38 mAh cm^{-2} at 0.1 mA cm^{-2} and improved energy efficiency greater than 87.1% for 100 cycles.

Hu et al. [300] also prepared an HMLE for Li-CO_2 batteries involving chemically treated, ultralight and mechanically flexible balsa wood (Fig. 18g) that were incorporated with CNTs to load Ru catalysts in which the wood open microstructure can be perfectly preserved to provide microchannels for CO_2 gas flow and electrolyte penetration (Fig. 18h). These directional channels can also enable the rapid transfer of products from Li_2CO_3 decomposition, allowing a resulting 2000-μm-thick wood/CNT/Ru electrode to demonstrate a high areal capacity of 11 mAh cm^{-2} at a high mass loading of 200 mg cm^{-2}. These researchers also reported that a flexible Li-CO_2 pouch cell was able to maintain constant open circuit voltage (OCV) during cycling under folding/rolling/bending conditions, demonstrating the potential of the flexible wood scaffold in the design of flexible HMLEs for various EESS applications. Overall, improvements to overall performance in Li-CO_2 batteries require the challenging design of HMLEs with 3D open and interconnected structures that can be decorated with uniform and ultrafine electrocatalysts. To address this, Hu et al. [301] developed a reasonable route involving 3D-printing combined with rapid and high-temperature thermal shocking to obtain ultrafine Ni nanoparticles (5 nm) anchored onto a 3D porous rGO framework (Fig. 18i) in which a 400-μm-ultrathick electrode achieved a high areal capacity of 14.6 mAh cm^{-2} at 0.1 mA cm^{-2} and stable cycling performances at 100 mA g^{-1} with a specific capacity limited to 1000 mAh g^{-1} (Fig. 18j).

4.5 Other Advanced Secondary Batteries

4.5.1 Zinc Batteries

Compared with LIBs using toxic and flammable electrolytes [307], aqueous zinc batteries (ZBs) are much cheaper and safer due to the use of low-cost Zn metal and nonflammable aqueous electrolytes as well as the avoidance of protective package required to prevent electrolyte leakage [308]. Despite this, ZBs face low energy densities in which the construction of HMLEs is of great significance, particularly for flexible ZBs. In addition, key issues need to be carefully considered, including: (1) flexible substrates that need to be electronically/ionically conductive, mechanically flexible and stable, open structured to allow for electrolyte infiltration and high mass loading as well as inexpensive and scalable; (2) nanostructured AMs that should possess hierarchical structures to prevent self-agglomeration and enable rapid charge delivery in which desirable AMs can provide more exposed active sites for charge storage; and (3) good interfacial interactions between AMs and substrates that can contribute to enhanced capacity and cycling performance. Based on this, Deng et al. [302] used a conductive commercial textile as a 3D scaffold to in situ grow hierarchical and self-branching structured NiCo-hydroxide and MnO_2 nanosheets (Fig. 19a) and allow for adequate voids spacing to accommodate electrolyte penetration and high mass loading in which mass loadings of 9.15 mg cm^{-2} and 6 mg cm^{-2} can be achieved for MnO_2 and NiCo-hydroxide electrodes respectively. As a result, corresponding solid-state Zn-Ni and Zn-MnO_2 batteries based on NiCo and MnO_2 cathodes achieved volumetric energy densities of 15 mWh cm^{-3} at a power density of 15 mW cm^{-3} and 12 mWh cm^{-3} at 13 mW cm^{-3} respectively. Moreover, the open circuit voltage of a Zn–Ni battery after four-times cutting remained at 97% in which the CV profiles of the cutting cell remained at well-defined redox potentials, indicating high reliability.

Attention has also been paid to the exploration of novel ZB cathodes such as manganese oxides, Prussian blue analogues, cobalt-based composites and vanadium-based

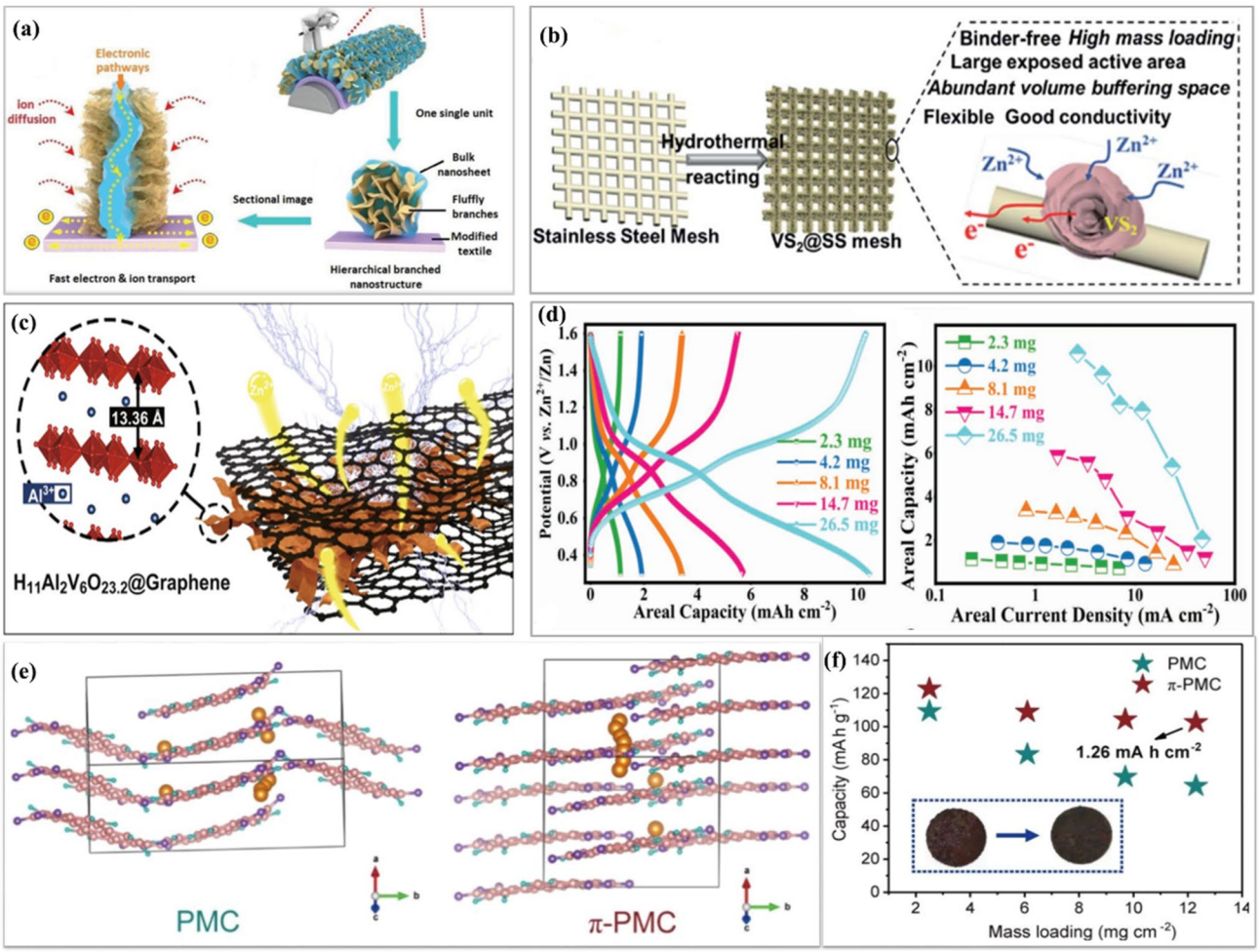

Fig. 19 **a** Schematic of building textile electrodes with hierarchical branched structures. Reprinted with permission from Ref. [302]. Copyright © 2018, Wiley–VCH. **b** Schematic of the preparation of binder-free hierarchical VS_2 electrodes. Reprinted with permission from Ref. [303]. Copyright © 2019, The Royal Society of Chemistry. **c** Graphene-wrapped aluminum vanadate nanobelts for HMLEs. Reprinted with permission from Ref. [304]. Copyright © 2020, Springer Nature. **d** Performance of an aqueous zinc battery enabled by pseudo-Zn-Air and Zn-ion intercalation dual mechanisms. Reprinted with permission from Ref. [305]. Copyright © 2019, Wiley–VCH. **e** Diffusion paths of Zn ions in PMC and π-PMC. **f** Gravimetric capacity at different mass loadings of PMC and π-PMC cathodes. Reprinted with permission from Ref. [306]. Copyright © 2020, The Royal Society of Chemistry

materials [309]. For example, various vanadium materials such as V_2O_5, $Na_2V_6O_{16}$, VS_2, V_5O_{12} and $H_{11}Al_2V_6O_{23.2}$ have been successfully developed in which Zhang et al. [303] fabricated a freestanding electrode with open-structured VS_2 flowers directly grown on stainless steel (Fig. 19b) that possessed a well-defined nanostructure with high electrical conductivity and enlarged contact area between the electrolyte and the electrodes, allowing for a high capacity of 198 mAh g^{-1} at 50 mA g^{-1} with a high mass loading of 11.3 mg cm^{-2} as well as a stable areal capacity of 1.8 mAh cm^{-2} with 92% capacity retention after 200 cycles. Zhou et al. [304] also fabricated a core–shell structured $H_{11}Al_2V_6O_{23.2}$/graphene electrode (Fig. 19c) that delivered an ideal reversible capacity of 131.7 mAh g^{-1} at 2 A g^{-1} after 400 cycles even at a high mass loading of 15.7 mg cm^{-2}. Wang et al. [305] further fabricated a $V_5O_{12}{\cdot}6H_2O$/graphene oxide (VO@GO) (Fig. 19d) cathode that displayed a maximum specific capacity of 496 mAh g^{-1} at 100 mA g^{-1} through the simple regulation of GO surface states and attributed the enhanced performances to the well-defined working mechanism combining reversible Zn ion insertion/extraction with electrochemical redox reactions on GO surface functional groups. These researchers also reported that this hybrid working mechanism allowed the VO@GO electrode to provide high areal capacities up to 10.6 mAh cm^{-2} under a mass loading of 26.5 mg cm^{-2} as well as high cycling stability with 84.7% capacity retention over 10000 cycles at 10 A g^{-1}.

Despite this, most cathodes based on transition metals suffer from slow Zn-ion insertion/extraction kinetics to

result in poor rate performances. However, organic molecular crystals (OMCs) with large conjugated systems can overcome intermolecular forces during ion insertion/extraction due to their ability to lower repulsion for ion diffusion, making OMCs potential cathodes in high rate ZIBs. Based on this, Lu et al. [306] used organic solid power 3,4,9,10-perylenetetracarboxylic dianhydride (PMC) with 1-D molecular tunnels surrounded by carbonyl oxygen from anhydride as a model cathode to enable rapid Zn-ion insertion/extraction and diffusion. A temperature gradient sublimation method was applied to enhance the electrical conductivity of PMC via improved π-π stacking interactions, which contributed to enhanced electron transport between molecular layers and form abundant negative charge in the 1-D tunnel walls to facilitate ion diffusion (Fig. 19e). As a result, the PMC cathode showed excellent rate performances with 62.6% capacity retention from 1.6 to 260.4 C as well as a high areal capacity of 1.26 mAh cm^{-2} (102.7 mAh g^{-1}) at a mass loading of 12.3 mg cm^{-2} (Fig. 19f). Wang et al. [310] further developed a novel Zn-organic battery using sulfur heterocyclic quinone dibenzo-[b,i]thianthrene-5,7,12,14-tetraone (DTT) as the cathode to suppress the unstable nature of organic molecules in which the DTT cathode simultaneously accommodated protons (H^+) and Zn^{2+} ions with the formation of discharge products of $DTT_2(H^+)_4(Zn^{2+})$. As a result, the working mechanism allowed a DTT//Zn full battery to demonstrate unprecedented cycling performances of 23000 cycles with capacity retention of 83.3% and a highly reversible capacity of 210.9 mAh g^{-1} at 50 mA g^{-1} at a mass loading of 5 mg cm^{-2}.

4.5.2 Aluminum-Ion Batteries

Aluminum-ion batteries (AIBs) are also promising post-lithium energy storage technologies because aluminum metal can offer a high theoretical gravimetric capacity of 2980 mAh g^{-1} and a volumetric capacity of 8040 mAh cm^{-3} [311]. In addition, the nonflammable room temperature ionic liquid (RTIL) electrolytes [312], low-cost Al metal and enhanced handling safety due to the inert reactivity of

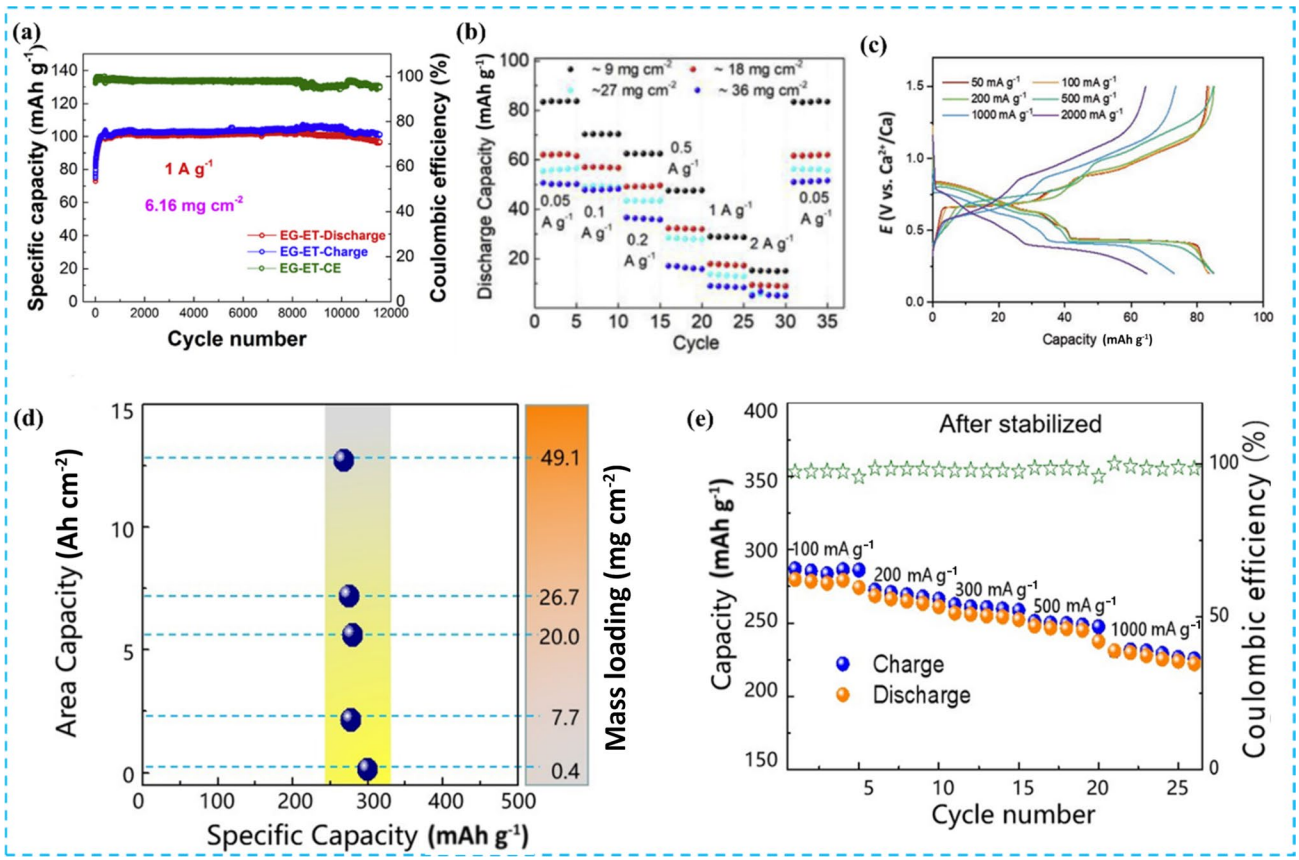

Fig. 20 **a** Cycling stability of commercially expanded graphite electrodes for AIBs. Reprinted with permission from Ref. [317]. Copyright © 2019, Elsevier. **b** Rate performances of HMLEs for AIBs. Reprinted with permission from Ref. [26]. Copyright © 2019, Elsevier. **c** Capacities of Ca-ion batteries through calcium intercalation into graphite. Reprinted with permission from Ref. [319]. Copyright © 2020, Wiley–VCH. **d** Areal capacities and **e** rate performances of MBs mediated by cuprous charge carriers. Reprinted with permission from Ref. [320]. Copyright © 2020, Wiley–VCH

Al metal make AIB systems promising for next-generation EESSs [313]. Based on this, our group conducted research into favorable cathodes for AIBs to reveal the importance of efficient, cost-effective and reliable cathode materials in AIBs [314–316]. And although achievements have been made, research focused on AIB HMLEs remains lacking in which only graphite has been used as AIB HMLEs due to relatively fast electrochemical kinetics, low costs and natural abundance. For example, Gao et al. [317] fabricated an AIB using commercially expanded graphite (EG) as a cost-effective cathode and low-cost $AlCl_3$-triethylamine hydrochloride ($AlCl_3$-ET) as the electrolyte in which EG possessed a hierarchical pore structure that can enhance electrolyte infiltration and intercalated ion diffusion, allowing an assembled coin cell with a mass loading of 6.16 mg cm^{-2} to display a gravimetric capacity of 101 mAh g^{-1} (207 mAh cm^{-3}) at 1 A g^{-1} and high capacity retention of 95.5% after 11500 cycles (Fig. 20a). Marcilla et al. [318] also comprehensively studied the influences of the graphitic degree, particle size and mass loading in several commercial carbon cathodes on AIB performance and reported that highly graphitic, low particle-sized and porous carbon cathodes such as synthetic graphite flakes (SGFs) provided optimal AIB performances in which an SGF-based HMLE was able to deliver a specific capacity of 85 mAh g^{-1} at a mass loading of 10 mg cm^{-2} and an impressive areal capacity of 5.5 mAh cm^{-2} at 100 mg cm^{-2} loading. AIB performances under HMLE conditions can further be improved based on the optimization of current collectors in which conventional metal current collectors can be damaged by corrosive electrolytes containing acidic RTIL with $Al_2Cl^-_7$, whereas the large anionic radius of $AlCl^-_4$ can result in severe volume expansion in both current collectors and electrodes [84]. Here, Fang et al. [26] fabricated an ultralight carbon current collector with sufficient chemical and mechanical stability derived from biomass cotton that possessed a 3D network structure for effective electrical/ionic transportation and reported that electrodes constructed through the casting of smaller-sized graphite (4000 mesh) on one side of the current collector can enhance battery performance, allowing for an electrode with a mass loading of 36 mg cm^{-2} to provide an areal capacity of 2.01 mAh cm^{-2} (49 mAh g^{-1}) at 50 mA g^{-1} (Fig. 20b) in which the improved performances were attributed to enhanced material utilization efficiency due to the porous current collector as well as the small-sized graphite powder.

4.5.3 Calcium-Ion Batteries

Calcium-ion batteries (CIBs) are also promising multi-electron battery systems because of the low standard electrode potential of Ca/Ca^{2+} (i.e., − 2.87 V vs. SHE) and the corresponding natural abundance, lightweight and stable multivalent states of calcium [321]. In addition, metallic calcium anodes can produce a high gravimetric capacity of 1337 mAh g^{-1} and a volumetric capacity of 2027 mAh cm^{-3}. Despite this, several fundamental challenges stall CIB development, including sluggish ion diffusion kinetics in host materials, large electrode/electrolyte interfacial resistances and high energy requirements for the solvation breaking of Ca^{2+} ions that form strong solvation structures with solvent molecules in electrolytes [319]. In this respect, the search for suitable calcium host materials and electrolyte engineering strategies can efficiently mitigate these issues. For example, Sakurai et al. [322] investigated the influence of water in electrolytes on Ca^{2+} insertion/extraction in α-V_2O_5 in which a three-electrode system constructed by using V_2O_5 as the working electrode at a mass loading of 30 mg cm^{-2} clearly demonstrated reductions in overpotential with the addition of water in the electrolyte. Cycling performances deteriorated significantly with the excessive water content, however, indicating the need to balance the water addition ratio versus cycling performance. Kant et al. [319] studied the reversible de/intercalation of calcium ions in low-cost graphite hosts in which although studies have demonstrated that graphite can allow for the de/intercalation of Ca^{2+} at relatively high temperatures, the use of graphite in room-temperature CIBs needs further attention. Here, these researchers selected dimethylacetamide (DMAc)-based electrolyte to enable the intercalation of Ca^{2+} into graphite with the formation of $[Ca\text{-}(DMAc)_4]C_{50}$ ternary GIC and reported that co-intercalation with the DMAc solvent enhanced Ca^{2+} intercalation and reversibility in graphite, which resulted in a graphite electrode with a mass loading of 3 mg cm^{-2} showing outstanding rate capabilities with negligible capacity fading even at 2000 mA g^{-1} (Fig. 20c).

4.5.4 Magnesium Batteries

Magnesium batteries (MBs) can deliver an excellent specific capacity of 2205 mAh g^{-1} and a volumetric capacity of 3833 mAh cm^{-3} [323]. In addition, Mg reserves in the earth's crust is 2.9%, which is much higher than those of Li with only 0.002%, suggesting the commercial potential of MBs. Unfortunately, the development of MBs is hindered by a poor cycling life and large polarization due to sluggish Mg^{2+} diffusion kinetics in host materials and difficulties in breaking Mg^{2+} and anion bonds [324]. Here, the incorporation of charge carriers can enhance the co-intercalation or co-conversion of Mg^{2+}. For example, Cui et al. [320] recently proposed a novel charge carrier that can mediate magnesiation with the assistance of Cu^+ in which the rapid Cu^+ equilibrium between the Cu_3Se_2 electrode and the electrolyte can promote reversible chemical magnesiation/demagnesiation between Cu^+ and Mg^{2+} to contribute to rapid

Table 3 Electrochemical performances of representative HMLEs for SCs

Materials	Electrolyte	Mass loading (mg cm^{-2})	Electrode thickness (μm)	Gravimetric capacitance (F g^{-1})	Areal capacitance (F cm^{-2})	Volumetric capacitance (F cm^{-3})	Rate performance (F cm^{-2})	Reference
Graphene	6 M (1 M = 1 mol L^{-1}) KOH	10.5	–	140 at 1 mA cm^{-2}	1 at 1 mA cm^{-2}	38.9 at 1 mA cm^{-2}	–	[328]
CF	$TEABF_4$/AN	10	150	112 at 1 A g^{-1}	–	74 at 1 A g^{-1}	~80 F g^{-1} at 10 A g^{-1}	[329]
AC	1 M NaCl	55	2000	83 at 1 mV s^{-1}	–	–	–	[330]
CB	6 M KOH	10	700	111 at 1 A g^{-1}	1.28 at 1 A g^{-1}	16.1 at 1 A g^{-1}	–	[331]
AC	$TEABF_4$/AN	54.6	800	–	7.4 at 5 mV s^{-1}	–	–	[332]
Holey-G	$EMIMBF_4$/AN	10	150	317 at 1 A g^{-1}	–	212 at 1 A g^{-1}	~240 F g^{-1} at 50 A g^{-1}	[93]
Graphene	1 M H_2SO_4	11.2	70	226 at 1 A g^{-1}	2.53 at 1 A g^{-1}	–	113 F g^{-1} at 10 A g^{-1}	[333]
WC	1 M NaCl	50	1200	87.1 at 1 mV s^{-1}	–	–	–	[21]
Carbon nanosheet	6 M KOH	12.5	125	328 at 1 A g^{-1}	4.102 at 1 A g^{-1}	328 at 1 A g^{-1}	280 F g^{-1} at 16 A g^{-1}	[334]
MnO_x	5 M LiCl	23.1	–	–	4.2 at 5 mV s^{-1}	–	1.26 at 100 mV s^{-1}	[335]
MnO_2	1 M Na_2SO_4	10	–	332 at 1 mA cm^{-2}	3.32 at 1 mA cm^{-2}	–	1.9 at 30 mA cm^{-2}	[336]
Porous carbon	6 M KOH	25	–	–	5.7 at 1 A g^{-1}	–	–	[120]
Graphene monolith	$EMIMBF_4$	–	400	–	–	150 at 0.2 A g^{-1}	> 60 F cm^{-3} at 0.8 A g^{-1}	[337]
Graphene/PEDOT	1 M H_2SO_4	33	260	175 at 0.39 A g^{-1}	5.37 at 33 mA cm^{-2}	203 at 33 mA cm^{-2}	> 125 F g^{-1} at 70 mA cm^{-2}	[338]
MXene/PANI	3 M H_2SO_4	23.8	90	336 at 10 mV s^{-1}	–	888 at 10 mV s^{-1}	–	[339]
MoO_{3-x}	3 M KCl	15.4		282 at 1 mA cm^{-2}	4.43 at 1 mA cm^{-2}	–	~3 at 20 mA cm^{-2}	[340]
MoO_x/G	3 M KCl	13.8	–	240 at 5 mA cm^{-2}	3.3 at 5 mA cm^{-2}	–	1.86 at 100 mA cm^{-2}	[341]
PPy/G	2 M KOH	–	2000	395 at 6 A g^{-1}	1.1 at 0.5 mA cm^{-2}	3.5 at 1 mA cm^{-2}	~0.7 at 5 mA cm^{-2}	[342]
MWCNT	1 M H_2SO_4		500	–	~0.17 at 0.5 mA cm^{-2}	1.71 at 10 mA cm^{-2}	~0.15 at 5 mA cm^{-2}	[343]
Carbon/β-FeOOH	3 M LiCl	10	–	150 at 1 mA cm^{-2}	1.5 at 1 mA cm^{-2}	–	0.87 at 50 mA cm^{-2}	[344]
MnO_2/G	3 M LiCl	182.2	4000	242.19 at 0.5 mA cm^{-2}	44.13 at 0.5 mA cm^{-2}	110 at 0.5 mA cm^{-2}	> 30 at 10 mA cm^{-2}	[345]
WC/CNT	1 M Na_2SO_4	–	500	215.3 at 7 mA cm^{-2}	–	76.5 at 7 mA cm^{-2}	185.9 F g^{-1} at 20 mA cm^{-2}	[139]
WC	1 M Na_2SO_4	30	1000	118.7 at 1 mA cm^{-2}	3.2 at 1 mA cm^{-2}	–	2.8 at 30 mA cm^{-2}	[55]
LCAN	6 M KOH	147	4200	181 at 1 mA cm^{-2}	26.6 at 1 mA cm^{-2}	–	16.4 at 200 mA cm^{-2}	[346]

WC: wood carbon, CF: carbon iber, CC: carbon cloth, G: graphene, AC: activated carbon, CB: carbon black, LCAN: lignin carbon aerogels/nickel

electrochemical reaction kinetics. As a result, corresponding Mg/Cu_3Se_2 batteries showed highly stable areal capacities of 5.2 and 12.52 mAh cm^{-2} for high loading cathodes with 20 and 49.1 mg cm^{-2} respectively (Fig. 20d) as well as stable and excellent rate performances even at a high current density of 1000 mA g^{-1} (Fig. 20e).

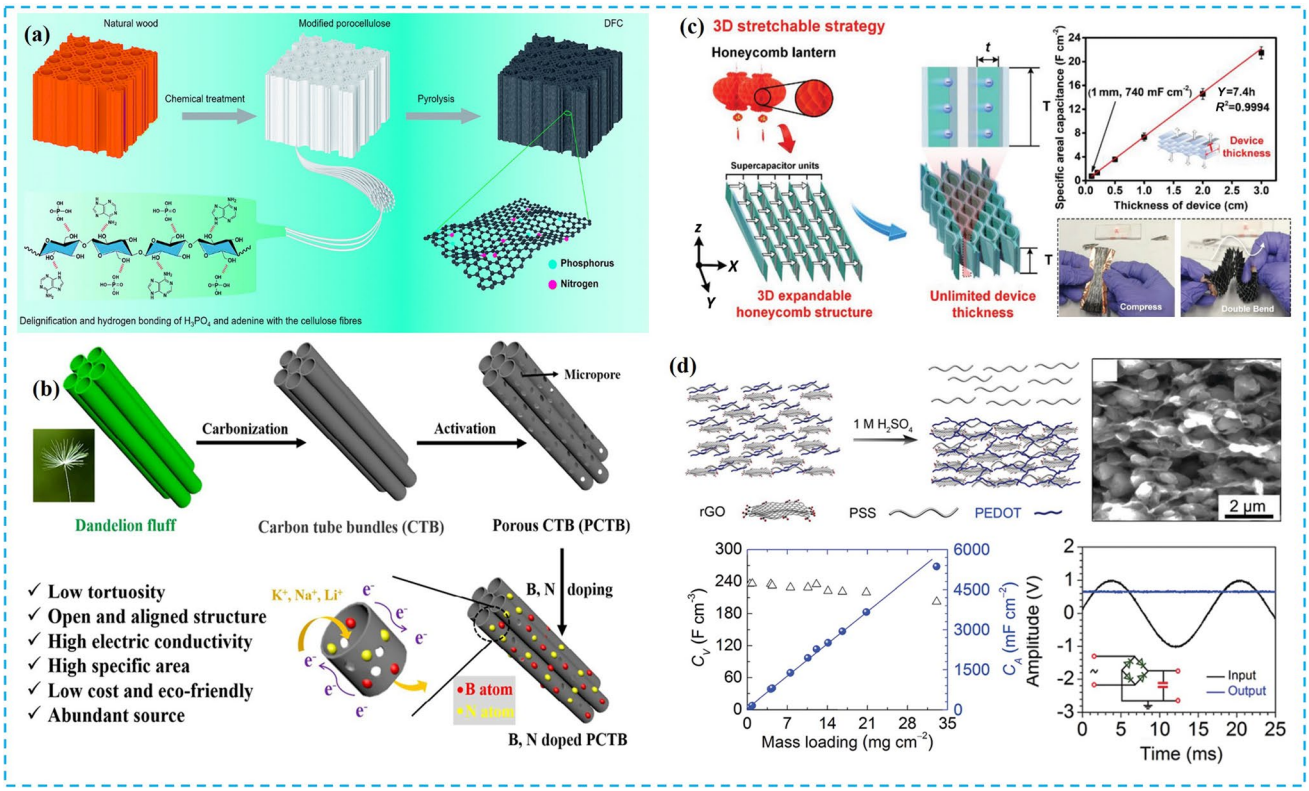

Fig. 21 **a** Schematic of porous carbon derived from wood after chemical treatment. Reprinted with permission from Ref. [347]. Copyright © 2020, The Royal Society of Chemistry. **b** Preparation of N/B co-doped carbon tubes from dandelion fluff. Reprinted with permission from Ref. [348]. Copyright © 2017, The Royal Society of Chemistry. **c** 3D stretchable SCs with expandable honeycomb composite electrodes and their bending stability. Reprinted with permission from Ref. [349]. Copyright © 2018, Wiley–VCH. **d** Formation of the PEDOT:PSS/graphene composite electrode and its application in HMLEs and AC-line filtering. Reprinted with permission from Ref. [338]. Copyright © 2018, The Royal Society of Chemistry

4.6 Supercapacitors

Although supercapacitors (SCs) can be applied in high-power energy devices, they also require enhanced energy density to satisfy requirements in various application fields [12]. Accordingly, hybrid SCs that can combine capacitive-type and battery-type materials as negative and positive electrodes such as Li-ion capacitors [325], Na-ion capacitors and K-ion capacitors [326, 327] have been reported as high-energy SCs in recent years. Based on this, HMLE designs for SCs can effectively improve overall energy density and pioneering reviews on material designs with high mass loadings for SCs have been reported [12, 23]. In this review, a brief summary of HMLE designs mainly based on carbon materials, 2D conducting materials and metal-based redox-active materials for SCs is presented. Table 3 lists the capacitive performances of select HMLEs for SCs.

4.6.1 Porous Carbon

Porous carbon is one of the most progressive electrode materials for commercial SCs [90, 350], particularly biomass-derived carbon in which wood can be applied to prepare carbon materials from bulk [351]. For example, Hu et al. [54] directly prepared all-wood-based SCs using AWC electrodes (800-μm-thick and 30 mg cm^{-2}) as inspired by the low tortuosity and vertical channels of wood. Similarly, Liu et al. [21] studied the capacitive performances of WC (1200-μm-thick and 50 mg cm^{-2}) with further application in capacitive deionization to water treatment. Huang et al. [347] recently obtained ultrathick WC electrodes (up to 2400 μm) from modified porocellulose through the chemical treatment of natural wood (Fig. 21a) in which the resulting WC electrode demonstrated an excellent electrical conductivity of 123.4 S m^{-1} and an impressive capacitance of 2980

mF cm^{-2}. Aside from the unique microstructures of biomass materials, the incorporation of heteroatoms can also effectively improve capacitive performance. For example, Fang et al. [348] prepared low-tortuosity and porous N/B co-doped carbon tubes derived from dandelion fluff (Fig. 21b) with a thin-wall and hollow bundled structure that can effectively enhance mass transport to contribute to a high specific capacity of 216 F g^{-1} under a mass loading of 40 mg cm^{-2} and even a volumetric energy density of 12.15 Wh L^{-1} at a total electrode loading of 80 mg cm^{-2} for a corresponding SC.

4.6.2 Conducting Polymer

Conducting polymers (CPs) have also been widely investigated as electrode materials for SCs due to large theoretical capacitances, high electrical conductivities, low costs and easily scalable production [352]. In addition, CPs are versatile platforms that can be processed into multifunctional, changeable and flexible electrode configurations for novel SCs such as flexible SCs, wearable SCs and stretchable SCs [353, 354]. More importantly, CPs can be combined with or loaded onto other conductive substrates such as graphene aerogels, graphene foam, CNT nanofibers and carbon monoliths as composite SC electrodes. In recent years, researchers have started to investigate multifunctional SC devices to meet the demands of diverse application scenarios. For example, stretchable SCs can be used to power wearable and stretchable electronics in healthcare applications, but corresponding HMLEs are difficult to design due to structural instability during mechanical deformation. To address this, Chen et al. [349] proposed a 3D stretchable SC with an expandable honeycomb structure (Fig. 21c) that addressed the issues faced by HMLE designs intrinsically limited by conventional 2D counterparts, because vertically aligned SC units can provide rapid ionic transfer due to strain distribution during bending that located in the vertical direction matched with the stretching direction, which allowed the stretching of the SC to be independent of device thickness. Specifically, doped polypyrrole as a flexible conducting polymer was used as the active material to form composites with black-phosphorous oxide electrodeposited on CNT films to result in an ultrathick 3D rectangular-shaped SC (1 cm) that delivered a high areal capacitance of 7.34 F cm^{-2} in which an up to 3-cm-thick composite electrode with a maximum mass loading of (453 ± 36) mg cm^{-2} can be achieved.

High rate frequency response SCs are also viable alternatives to conventional aluminum electrolytic capacitors in application as alternating current filtering devices [355]. Based on this and to develop SCs with HMLEs and high rate responses, Shi et al. [338] developed a robust paper electrode

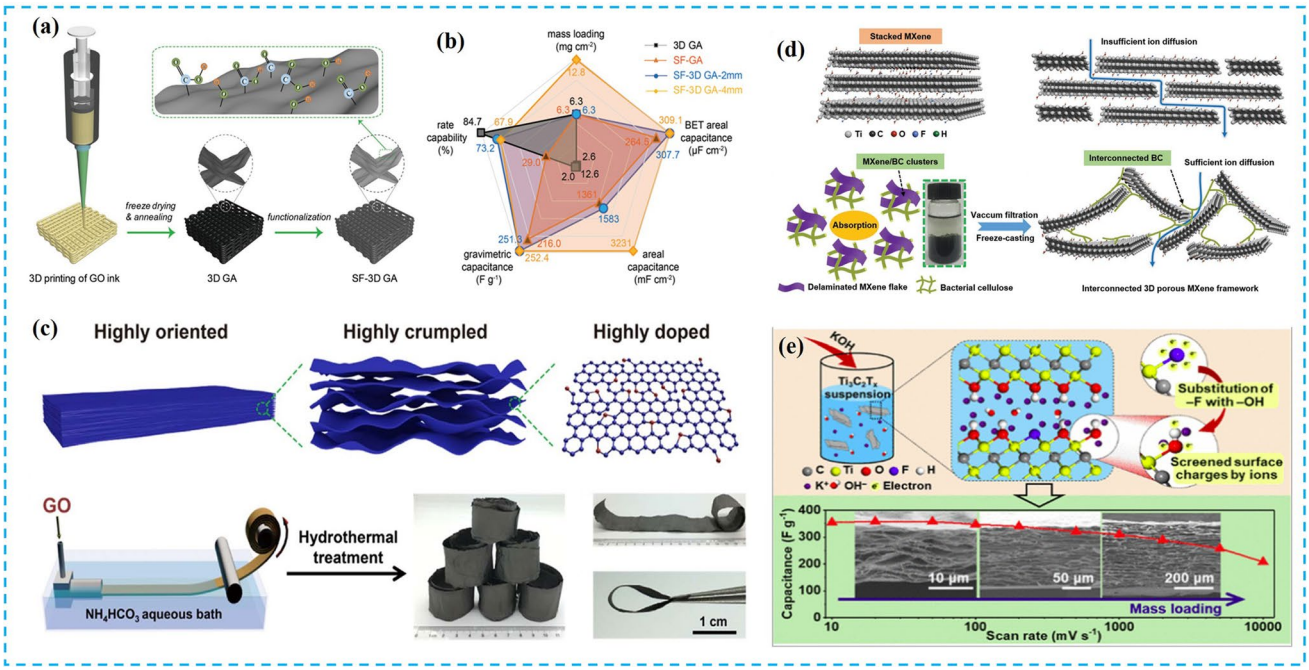

Fig. 22 **a** Illustration of 3D-printed GO aerogels and **b** a radar chart comparing the five merits of 3D-GO electrodes. Reprinted with permission from Ref. [50]. Copyright © 2020, Wiley–VCH. **c** Tri-high designed graphene electrodes. Reprinted with permission from Ref. [333]. Copyright © 2020, Elsevier. **d** Schematic of the design of porous MXene with ion transport channels. Reprinted with permission from Ref. [362]. Copyright © 2019, Wiley–VCH. **e** High-mass-loading porous $Ti_3C_2T_x$ film electrode and corresponding capacitive performance. Reprinted with permission from Ref. [363]. Copyright © 2020, American Chemical Society

with porous graphene inter-bridging using highly conductive PEDOT polymer to obtain a 3D network structure with open channels (Fig. 21d). As a result, a corresponding SC using this paper electrode with a low mass loading of 0.012 mg cm^{-2} showed desirable rate frequency responses with a large phase angle of −81.4° at 120 Hz that can be successfully used in practical AC line-filtering. In addition, an ultrathick electrode with a mass loading of 33 mg cm^{-2} was able to exhibit a remarkable areal capacity of 5365 mF cm^{-2} and a volumetric capacitance of 203 F cm^{-3} at 1 A g^{-1}, demonstrating the viability of this strategy to achieve perfectly integrated SCs for AC line-filtering and HMLEs for compact EESSs in one system and paving the way to practical application.

4.6.3 2D Conductive Materials

2D conductive materials with large-sized ultrathin layered structures, high aspect ratios and short electronic/ionic transfer lengths have attracted tremendous attention for application in miniaturized SCs due to easy processing. Despite this, most 2D conductive materials are expensive and demonstrate favorable capacitance only in sub-micrometer-thick thin films with low mass loadings [356]. However, graphene is an interesting candidate electrode material because of its high conductivity and structural flexibility [357], in which the transformation of 2D graphene into 3D graphene can further enhance performance due to the exposure of active sites and improvement of mass transfer. Based on this, Li et al. [50] fabricated 3D-printed surface-functionalized graphene aerogels (3D-GAs) with an open pore structure using large numbers of cylindrical rods containing folded graphene nanosheets (Fig. 22a) that allowed for efficient charge delivery. As a result, a corresponding 4000-μm-ultrathick electrode with a mass loading of 12.8 mg cm^{-2} provided a benchmark areal capacitance of 3231 mF cm^{-2} at 5 mA cm^{-2} and remarkable capacitance retention with 2195 mF cm^{-2} at 100 mA cm^{-2} (Fig. 22b). Dedicated strategies are required to balance material density, porosity and electrode thickness. For example, Yang et al. [337] used low dimensional graphene assembly to fabricate 3D hierarchical monoliths with high mass density and low tortuosity that can result in desired dense and thick electrodes in which after the precise control of porosity and density in the graphene monoliths by using zinc chloride ($ZnCl_2$) as a pore activator, ultrathick and dense electrodes with densities ranging from 1.58 to 0.65 g cm^{-3} can be obtained to deliver excellent volumetric capacitances of 168, 150, and 82 F cm^{-3} at electrode thicknesses of 100, 400 and 800 μm respectively. This device-level balancing strategy can also be extended to other EESSs and is not limited to SCs. Recently, Gao et al. [333] further generated a "highly oriented, highly crumpled and highly doped" (3H) graphene film (Fig. 22c) as an HMLE with a mass loading of 11.2 mg cm^{-2} for SC application in which the long-range orientation of the 3H design supported high electronic conductivity whereas the short-range highly crumpled/folded structure contributed to rapid ion transfer and N-doping effects can enhance charge accumulation.

Conductive MOFs are also viable SC 2D electrode materials due to tunable structures, high surface areas and abundant built-in redox centers. For example, Bao et al. [356] fabricated a 2D conductive MOF based on ultrasmall hexaaminobenzene (HAB) linkers whose π orbitals can strongly and fully conjugate with the d orbitals of Ni(ii)/Cu(ii) to allow the Ni-HAB and the Cu-HAB to show decent electrical conductivities of (70 ± 15) and (11 ± 3) S m^{-1}, respectively. And due to these high electrical conductivities as well as ultrafine Ni-HAB aggregates and periodic porosity of HAB MOFs, a 360-μm-thick Ni-HAB electrode provided a remarkable areal capacitance of 23 F cm^{-2} at 0.2 mV s^{-1} and good rate responses with 17 F cm^{-2} at 1 mV s^{-1} (460 F cm^{-3}) under a mass loading of 65 mg cm^{-2}. As another 2D conducting material, MXene generally suffers from strong aggregation and restacking that impede ion diffusion pathways and limit application in HMLEs. However, many advanced strategies have been proposed to achieve HMLEs based on MXene, including Ag-decorated MXene films that can provide an areal capacitance of 1173 F cm^{-2} at 15 mg cm^{-2} [358], MXene aerogels that can provide an areal capacitance of 1013 F cm^{-2} at 15 mg cm^{-2} [359] and partially delaminated MXene films that can provide an areal capacitance of 1770 F cm^{-2} under 20 mg cm^{-2} [360]. Gogotsi et al. [361] further conducted the mechanical shearing of a discotic lamellar liquid–crystal $Ti_3C_2T_x$ phase to introduce VANs into 2D MXene nanosheets and reported that the enhanced ion diffusion properties resulted in the thickness-independent capacitive performance of MXene electrodes, which showed slight performance declines as electrode thicknesses increased from 40 to 200 μm and maintained areal capacitances over 0.6 F cm^{-2} in a 200-μm-thick electrode at 2000 mV s^{-1}. Yuan et al. [362] also engineered ion transport channels through the self-assembly of bicontinuous porous MXene from an interconnected bacterial cellulose (BC) network (Fig. 22d) to result in an MXene/BC composite electrode that delivered an areal capacitance of 3410 mF cm^{-2} at 3 mA cm^{-2} with a mass loading of 8 mg cm^{-2}. In addition, Bo et al. [363] developed a porous MXene film through reduced-repulsion freeze-casting assembly (Fig. 22e) that enabled a high areal capacitance of 3731 F cm^{-2} at 10 mV s^{-1} with a mass loading of 16.18 mg cm^{-2}.

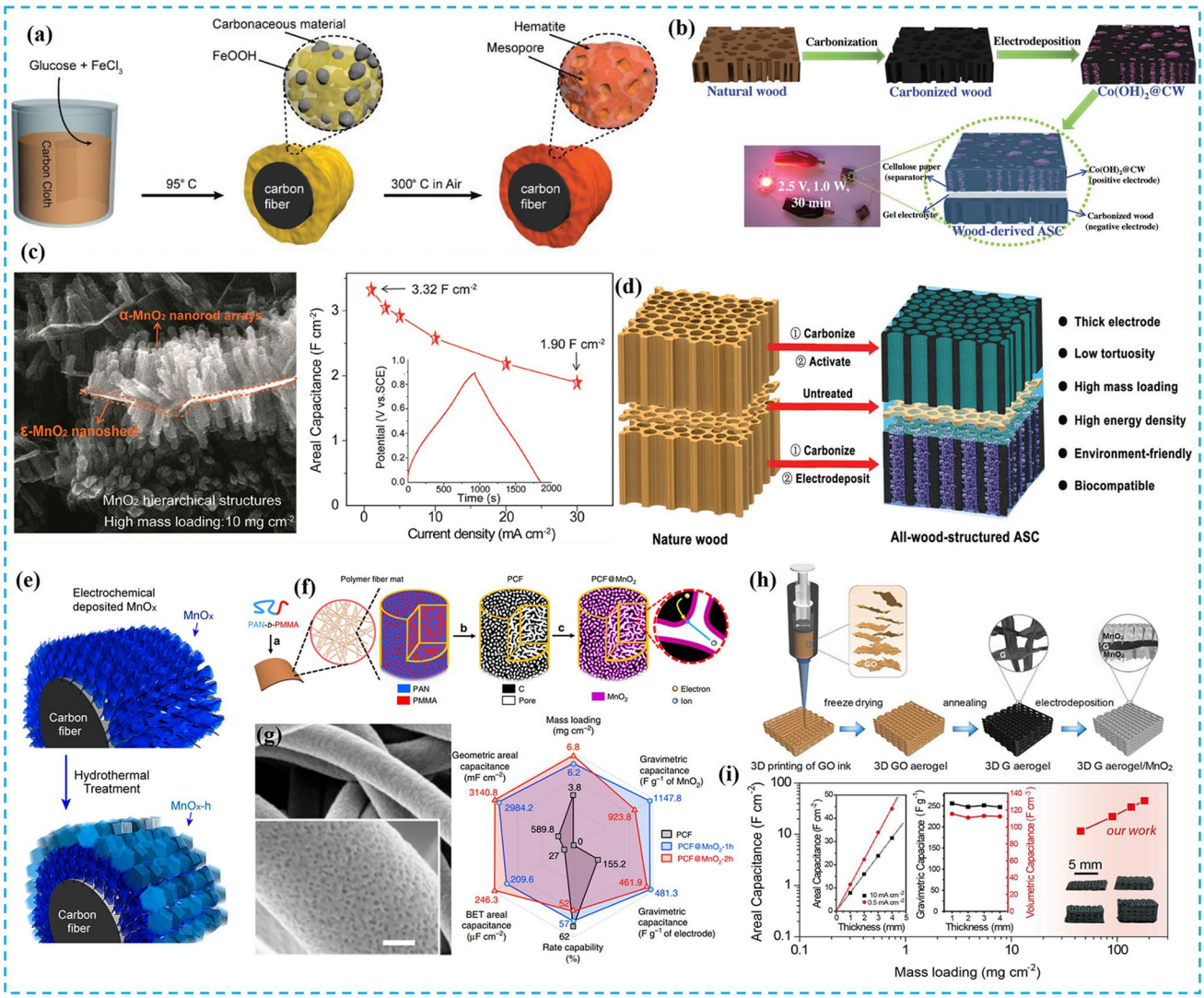

Fig. 23 **a** Fabrication of a mesoporous FeOOH/C composite. Reprinted with permission from Ref. [344]. Copyright © 2018, Wiley–VCH. **b** Ultrathick $Co(OH)_2$/wood-carbon electrode and application in an all-solid-state asymmetric supercapacitor (ASC). Reprinted with permission from Ref. [364]. Copyright © 2018, Wiley–VCH. **c** SEM image and capacitive performance of hierarchical structured MnO_2. Reprinted with permission from Ref. [336]. Copyright © 2018, American Chemical Society. **d** ACW for MnO_2 loading to design ultrathick electrodes and all-wood-based SCs. Reprinted with permission from Ref. [55]. Copyright © 2017, The Royal Society of Chemistry. **e** Structural change of MnO_x during hydrothermal reactions. Reprinted with permission from Ref. [335]. Copyright © 2017, American Chemical Society. **f** Block copolymer-derived porous carbon nanofiber electrode loaded with MnO_2, **g** microstructure of the porous carbon nanofiber and corresponding electrochemical performance. Reprinted with permission from Ref. [142]. Copyright © 2019, Springer Nature. **h** Illustration of the preparation of 3D-printed graphene/MnO_2 aerogels. **i** Areal capacitances of MnO_2/graphene electrodes with different mass loadings. Reprinted with permission from Ref. [345]. Copyright © 2019, Elsevier

4.6.4 Metal-Based Pseudocapacitive Materials

Pseudocapacitors based on redox-active faradic reactions can produce higher capacitances and energy densities than EDLCs and as a result, metal-based pseudocapacitive materials have been extensively studied in which to improve electrochemical performance in corresponding HMLEs, pore structure modification is particularly viable. For example, Li et al. [344] fabricated a mesoporous hematite film through hydrothermal reactions using glucose as an organic polymer template (Fig. 23a) in which during subsequent carbonization, glucose can serve as a sacrificial template to generate large amounts of gas to form mesopores in the final FeOOH/C composite. As a result, an optimized 1-μm-film coated FeOOH/C electrode with an average mesopore size of 3 nm enabled a high areal capacitance of 1.5 F cm^{-2} at 1 mA cm^{-2} and a good rate capability of 0.87 F cm^{-2} at 50 mA cm^{-2} even under a mass loading of 10 mg cm^{-2}, which these researchers attributed to the mesoporous structure with efficient ion diffusion and inner active site

utilization. The incorporation of highly porous conductive matrixes can also enhance performance. For example, Liu et al. [364] developed a wood-derived all-solid-state SC containing a 680-μm-thick CW anode and a $Co(OH)_2$/CW cathode (Fig. 23b) that delivered an outstanding energy density of 0.69 mWh cm^{-2} at a power density of 1.126 W cm^{-2}.

Many efficient strategies have also been applied to enhance the mass loading of MnO_2-based electrodes in pseudocapacitors [365]. These strategies include the electrodeposition of highly porous nanostructured MnO_2 layers onto CCs with a mass loading of 7.02 mg cm^{-2} [366], the morphological and phase-controlled electrodeposition of MnO_2 layers onto hierarchical nanostructures involving primary 2D nanosheets and secondary 1D nanorod arrays (Fig. 23c) with mass loadings of 10 mg cm^{-2} [336], the use of ultra-thick AWC frameworks as supports to greatly improve MnO_2 loadings to nearly 45 mg cm^{-2} (Fig. 23d) [55], the construction of unique sandwich porous structures of CNT film/double-sided carbon tape/CNT films to load MnO_2 with a mass loading of 6.6 mg cm^{-2} [367], and the hydrothermal treatment-assisted electrodeposition of MnO_x films with porous cores and crystal shell structures (Fig. 23e) with a mass loading of 9 mg cm^{-2} [335]. In a further example, Liu et al. [142] synthesized porous carbon fibers (PCFs) derived from block copolymers (Fig. 23f) and reported that the PCFs showed uniformly interconnected networks with porous fiber backbones, a high SSA of 557.8 m^2 g^{-1} and carefully designed mesopores 11.7 nm in the average diameter to provide adequate spacing for MnO_2 loading (Fig. 23g), resulting in the PCFs/MnO_2 electrode demonstrating a total mass loading of nearly 7 mg cm^{-2} to attain a remarkable areal capacitance of 3140.8 mF cm^{-2} (461.9 F g^{-1}) at 10 mV s^{-1}. An ultrahigh mass loading of 182.2 mg cm^{-2} for a graphene aerogel/MnO_2 electrode was also achieved by Yat et al. [345] through 3D printing (Fig. 23h) in which the predominant 5–50 μm macropores within the 3D printed ligaments can enable the uniform deposition of MnO_2 throughout the entire graphene aerogel as well as efficient ion transport, allowing a 4000-μm-thick SC electrode to exhibit a remarkable areal capacitance of 44.13 F cm^{-2} as well as a maximum energy density of 1.56 mWh cm^{-2} in a corresponding SC (Fig. 23i). This 3D-printed composite electrode further provided a versatile platform to well-balance the gravimetric, areal and volumetric performances of the SC, demonstrating potential in other electrode materials.

5 Challenges and Perspective

Current research into HMLEs is focused on tackling key challenges including sluggish charge kinetics, poor electrode structural stability and lack of cost-effective production processes. And although significant progress has been made towards addressing these challenges, large gaps still exist between academic experimentation and industrial application in terms of vital issues that are often overlooked.

In addition to the electrochemical performance of HMLEs, thermal safety is another critical issue that hinders the practical application of batteries in which internal heat distribution and accumulation is a common issue that can affect the stability, safety, reliability and efficiency of battery systems. For example, heat generation and thermal variation across electrodes and electrolytes can lead to nonuniform electrochemical reactions that significantly affect metal deposition and dendrite formation [383]. In addition, dense and thick HMLE structures are not conducive to heat dispersion and conduction, which will result in the rapid accumulation of heat to generate unexpected metal dendrite growth, short-circuiting and low cycling stability. Based on this, Wang et al. [384] systematically investigated the effects of electrode design parameters (electrode thickness, AM volume fractions and particle size) on vital battery performances (energy density, power density and thermal behavior) by establishing an electrochemical-thermal coupling model and reported that temperature distribution increased with increasing electrode thickness from 35 to 65 μm with cell polarization increasing simultaneously at high charge rates. Mukherjee et al. [368] further provided a comprehensive analysis of the role of electrode microstructure on LIB thermal behavior (Fig. 24a) and found that internal temperatures increased faster for batteries with low porosity and high tortuosity cathodes in terms of various heat generation sources (Joule heat, reaction heat and reversible heat) in which Joule heat represented the major heating source for temperature generation in HMLEs because low porosity and high tortuosity HMLEs possess increased internal charge transport resistance that results in steep concentration and potential gradients to produce uneven Joule heat. In terms of SIBs, the representative thermal runway process (Fig. 24b) generally contains three stages, including a pre-stage initiated by excessive heating from electrochemical reactions and ambient temperature, a heat accumulation stage caused by exothermic chemical chain reactions from SEI decomposition, anode/electrolyte reactions, separator meltdown and cathode breakdown and a thermal abuse stage in which heat and oxygen accumulate to limit the oxygen index. Based on all of this, heat accumulation clearly relies on electrode structures with proper morphology, porosity and current density distributions and therefore, innovative strategies to homogenize heat generation and conduction are needed to improve uniform and stable electrochemical reaction kinetics. Unfortunately, comprehensive research into both the theoretical understanding and experimental

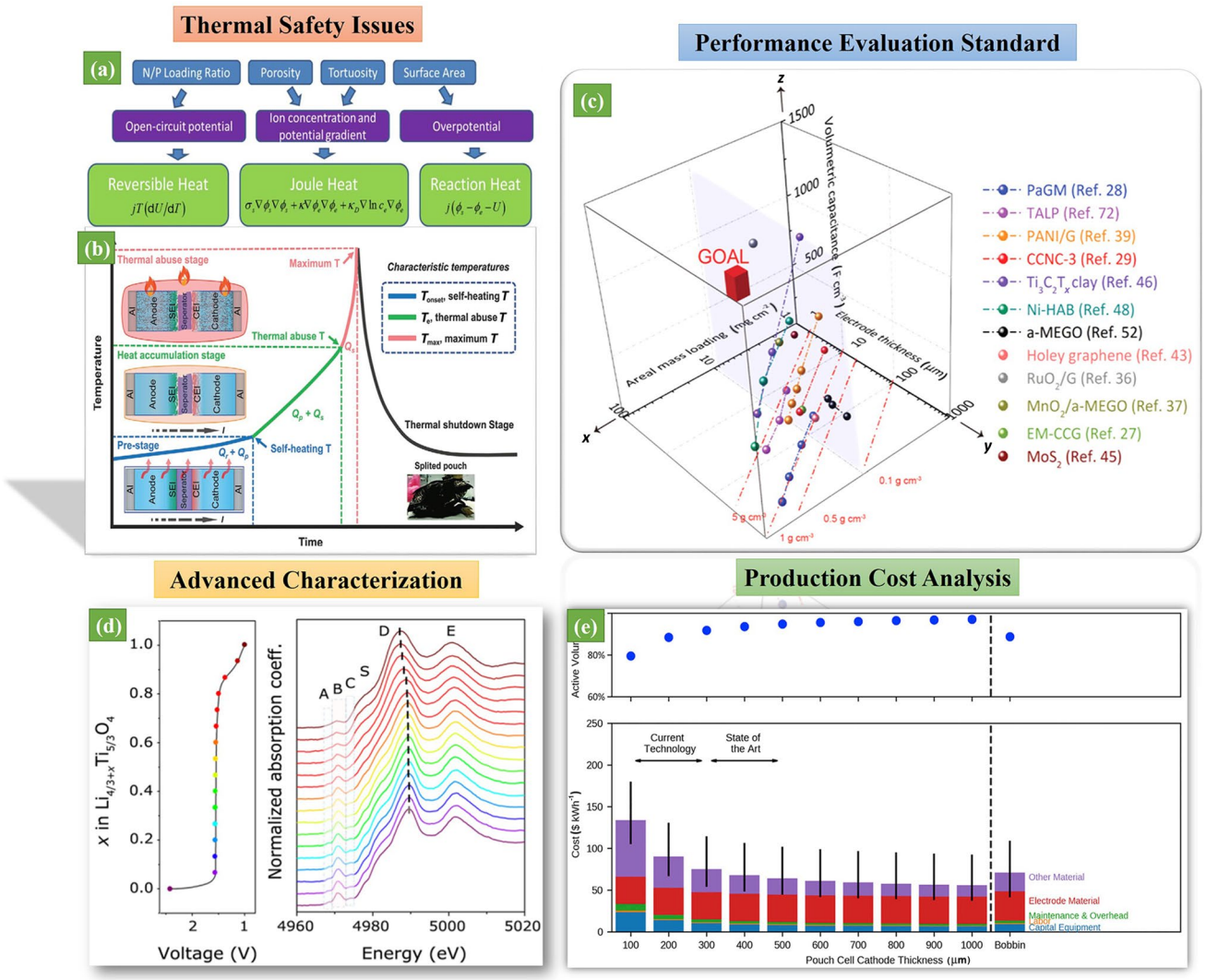

Fig. 24 Key challenges of HMLEs hindering commercial application and corresponding strategies. **a** Internal heat generation behaviors under different electrode parameters. Reprinted with permission from Ref. [368]. Copyright 2017 © IOP Publishing. **b** Thermal runaway in SIBs. Reprinted with permission from Ref. [369]. Copyright © 2020, Wiley–VCH. **c** 3D comparison of volumetric capacitance based on mass loading, thickness and electrode density. Reproduced with permission [337, 356, 370–380]. This figure is Reprinted with permission from Ref. [370]. Copyright © 2019, Wiley–VCH. **d** In situ XAS measurement as an example of an advanced characterization method. Reprinted with permission from Ref. [381]. Copyright © 2017, American Chemical Society. **e** Production cost analysis for cells with different cathode thicknesses. Reprinted with permission from Ref. [382]. Copyright © 2020, Elsevier

investigation of internal temperature generation in HMLEs remains lacking.

Batteries should also possess stable cycling over a wide temperature range. However, this is extremely difficult despite extensive research in which general reasons include metal plating at extremely low temperatures due to the undesirable battery polarization of SEI layers, charge-transfer resistances and low solid-state diffusion [385], which worsen in HMLEs as well as SEI compositional change, strong exothermic reactions involving intercalated metals with electrolytes and irreversible electrolyte consumption at elevated temperatures, all of which will result in accelerated capacity attenuation and lifetime decay as well as battery self-heating and cell combustion [386]. And although considerable efforts have been made to improve the thermal properties of battery components involving flame-retardant electrolyte additives [387], fire-resistant separators [388], nonflammable liquid electrolytes [389], solid-state electrolytes [390] and fire-resistant integrated electrodes [56], less attention has been paid to these issues in HMLEs. And therefore, the development of novel rational strategies to obtain

HMLEs that can cycle stably in a wide temperature window is needed.

Many correlating factors in HMLEs can further influence performance calculation accuracy and therefore require a more reasonable evaluation standard in which volumetric performance (VP) has recently gained attention as rating criteria to provide reliable performance evaluation and comparison [9, 14]. Currently, three levels of VP standards exist, including AM-VP, electrode-VP and whole device-VP [370]. Here, AM-VP may sometimes be overestimated due to the arbitrary selection of material density as determined by electrode processing due to inevitable material aggregation leading to inaccurate material volume. As for electrode-VP, the evaluation and comparison of electrode-VP are more accurate due to the ability to more precisely measure electrode volume and density. In addition, electrode-VP can take into account inactive components and is therefore a more feasible method for performance evaluation. Despite this, limitations in these two rating criteria hinder practical application. Alternatively, device-VP based on entire devices including inactive current collectors, separators and package materials is more useful in the assessment of HMLEs for practical use. However, VP can be affected by many mutually linked factors such as electrode thickness, porosity and areal mass loading in which current reports on high VP are always based on optimized factors such as highly porous electrodes with high density or ultrathin electrodes with low mass loading, leading to values that rarely reflect actual performance [14, 391]. Based on this, Yang et al. [370] provided an in-depth understanding of device-VP in SCs and reported the importance of thicker electrode designs to achieve high volumetric energy density EESSs at the device level. More importantly, these researchers proposed novel, reliable and universal rating formula based on comprehensive considerations of electrode porosity, areal mass loading and thickness to guide the evaluation of device level volumetric energy density ($E_{\text{v-device}}$):

$$E_{\text{v-device}} = \frac{25}{36}\frac{C_{\text{g-e}}aU^2}{2h + h_{\text{nonactive}}} \quad (2)$$

in which $C_{\text{g-e}}$ (F g^{-1}) is the gravimetric capacitance of the electrode, U (V) is the working potential window, a (mg cm^{-2}) is the areal mass loading, h (μm) is the electrode thickness and $h_{\text{nonactive}}$ (μm) is the thickness of the inactive components (detailed derivations can be found in their report in the supporting information section). Based on this rating principle (Fig. 24c), EESS development should concentrate on the rational design of thick electrodes with low porosity and high mass loading to obtain high device-VP. This study also suggested that future performance assessments of HMLEs can be revised based on the rating formula.

Electrode porosity and density are also important factors that can be used to evaluate the VP of HMLEs [15] in which highly porous electrode structures can provide adequate void spacing to accommodate efficient mass transfer, but will lead to the inevitable sacrifice of VP due to the existence of "death pores". For example, wood-derived scaffolds possess porosity of 60% whereas ice-template-derived electrodes possess porosity ranging from 30% to 50% [16], which strongly highlights the trade-off between electrode porosity and thickness that needs to be optimized. Highly porous electrode structures also sacrifice mechanical strength, especially compressive strength and therefore, a balance must be achieved between porosity and mechanical robustness to ensure minimum AM loading strength, electrical contact, and cycling stability.

Overall, electrode performance is influenced by various factors such as processing parameters (mixing time, foil velocity, coating volume, drying time, drying temperature, roller gap, etc.), AM structural parameters (particle size, porosity, tortuosity, density, adhesion strength, etc.) and other battery parameters (electrode conductivity, active specific surface area, diffusion coefficients, etc.) [392]. These factors become more intricate in HMLEs and therefore, universal guidelines to rationally fabricate AMs for HMLEs are difficult to propose but extremely important for industrial application. Here, machine learning represents an important technique to accelerate the discovery and design of new electrode materials in which over the past decades, computational simulations such as molecular dynamics, first-principle calculations, quantum mechanics and finite element simulations have been carried out in diverse application fields [108, 393]. In this regard, the establishment of versatile material discovery and design platforms based on machine learning strategies is meaningful to comprehensively accommodate emerging battery chemistry, materials composition, structures and interfacial information through the use of artificial intelligence to integrate and orchestrate data. This multi-functional platform is composed of smart components such as machine learning modules for automated analysis, novel battery materials and interfaces, multiscale simulations and physical models, databases and common data-infrastructure in which "self-driving" laboratories with the successful incorporation of computational material designs can enable the autonomous discovery of AMs that can meet HMLE requirements in the future.

Fundamental challenges including the real-time transformation of electrode/electrolyte interfaces during SEI dissolution/formation, the dynamic in situ characterization of mass transport within multiple time and length scales and the timely observation of relationships between electrode structure and battery performance also exist that require deeper understandings and further explorations. To address this, novel and advanced characterization methods need to be

introduced to *operando* observe battery working states and electrode structural changes in which in situ X-ray absorption spectroscopy (Fig. 24d) [381], in situ NMR spectroscopy [394], in situ high-resolution TEM [395], cryo-electron microscopy [396] and transmission X-ray microscopy are all applicable [397]. In addition, the integration of smart sensing technologies in battery systems can allow for the time-resolved monitoring of the battery functional status. The *operando* probing of electrochemical reaction processes using visible parameter changes in experimental methods is also viable. Overall, the combination of dynamic experimental methods with advanced computational modeling for the in situ quantitative measurement of electrochemical reaction parameters will come a reality in the near future.

The production cost analysis of battery systems is also essential in the design of reasonable AMs, electrode structures and cell configurations in the effort to reduce costs in which well-known LIB cost analyses based on the Argonne National Laboratory (ANL) "BatPaC" model and the TIAX model were proposed to comprehensively examine the manufacturing costs of overall cell production processes [398]. Specific steps have further been extensively analyzed such as NMP solvent dispersion chemistry, electrode coating thickness and different cell configurations (cylindrical cells, pouch cells, bobbin cells, etc.) to reveal that large cells with thick electrodes and low ratios of inactive current collectors and separators can reduce costs [399]. Despite this, the in-depth investigation of the effects of thick electrodes on cell production costs remains insufficient. However, Steingart et al. [382] recently conducted a cost analysis of LIBs with various electrode thicknesses in which for pouch cells, total costs including manufacturing and materials decreased as electrode thicknesses increased from 100 μm (Fig. 24e). These researchers also reported that marginal costs significantly decreased as active volumes increased and cell hardware costs decreased, demonstrating that manufacturing costs can reach less than \$100 kWh^{-1} by minimizing cell hardware costs and employing cost-effective AMs. The application of high capacity electrode materials to improve energy density at the cell level can also reduce production costs.

6 Conclusion

In conclusion, this review has demonstrated the importance of HMLE design in the future development of advanced EESSs. This review has also provided a comprehensive summary of current challenges in HMLEs as well as corresponding resolution strategies. The importance of HMLE design in diverse emerging battery systems was further highlighted in which fundamental understandings indicate complex physical and chemical factors towards desirable HMLE designs that require extensive research. And despite some achievements being made, HMLE designs experience significant gaps between laboratory performance and industrial application due to great challenges. However, the development of HMLE designs is the most promising strategy to obtain high-energy EESSs, especially for space-limited power devices. Overall, ideal HMLE-based EESSs will eventually be achieved in the near future based on an endless stream of novel and effective strategies.

Acknowledgements This work was supported by the National Basic Research Program of China (Grant No. 2015CB251100), the National Natural Science Foundation of China (Grant No. 21975026) and the Beijing Natural Science Foundation (Grant No. L182056).

References

1. Dunn, B., Kamath, H., Tarascon, J.M.: Electrical energy storage for the grid: a battery of choices. Science **334**, 928–935 (2011). https://doi.org/10.1126/science.1212741
2. Goodenough, J.B., Park, K.S.: The Li-ion rechargeable battery: a perspective. J. Am. Chem. Soc. **135**, 1167–1176 (2013). https://doi.org/10.1021/ja3091438
3. McCloskey, B.D.: Expanding the ragone plot: pushing the limits of energy storage. J. Phys. Chem. Lett. **6**, 3592–3593 (2015). https://doi.org/10.1021/acs.jpclett.5b01813
4. Wu, F., Yang, H.Y., Bai, Y., et al.: Multi-electron reaction concept for the universal battery design. J. Energy Chem. **51**, 416–417 (2020). https://doi.org/10.1016/j.jechem.2019.11.026
5. Huang, M.F., Zhen, S., Ren, X.L., et al.: High-voltage hydrous electrolytes for electrochemical energy storage. J. Power Sources **465**, 228265 (2020). https://doi.org/10.1016/j.jpowsour.2020.228265
6. Kuang, Y.D., Chen, C.J., Kirsch, D., et al.: Thick electrode batteries: principles, opportunities, and challenges. Adv. Energy Mater. **9**, 1901457 (2019). https://doi.org/10.1002/aenm.201901457
7. Wu, F., Maier, J., Yu, Y.: Guidelines and trends for next-generation rechargeable lithium and lithium-ion batteries. Chem. Soc. Rev. **49**, 1569–1614 (2020). https://doi.org/10.1039/c7cs00863e
8. Wang, L., Chen, B., Ma, J., et al.: Reviving lithium cobalt oxide-based lithium secondary batteries-toward a higher energy density. Chem. Soc. Rev. **47**, 6505–6602 (2018). https://doi.org/10.1039/c8cs00322j
9. Wang, Q., Yan, J., Fan, Z.J.: Carbon materials for high volumetric performance supercapacitors: design, progress, challenges and opportunities. Energy Environ. Sci. **9**, 729–762 (2016). https://doi.org/10.1039/C5EE03109E
10. Geng, H.Y., Peng, Y., Qu, L.T., et al.: Structure design and composition engineering of carbon-based nanomaterials for lithium energy storage. Adv. Energy Mater. **10**, 1903030 (2020). https://doi.org/10.1002/aenm.201903030
11. Manthiram, A., Vadivel Murugan, A., Sarkar, A., et al.: Nanostructured electrode materials for electrochemical energy storage and conversion. Energy Environ. Sci. **1**, 621–638 (2008). https://doi.org/10.1039/b811802g
12. Sun, H.T., Zhu, J., Baumann, D., et al.: Hierarchical 3D electrodes for electrochemical energy storage. Nat. Rev. Mater. **4**, 45–60 (2019). https://doi.org/10.1038/s41578-018-0069-9
13. Gogotsi, Y., Simon, P.: True performance metrics in electrochemical energy storage. Science **334**, 917–918 (2011). https://doi.org/10.1126/science.1213003

14. Zhang, C., Lv, W., Tao, Y., et al.: Towards superior volumetric performance: design and preparation of novel carbon materials for energy storage. Energy Environ. Sci. **8**, 1390–1403 (2015). https://doi.org/10.1039/c5ee00389j
15. Liu, C.C., Yan, X.J., Hu, F., et al.: Toward superior capacitive energy storage: recent advances in pore engineering for dense electrodes. Adv. Mater. **30**, 1705713 (2018). https://doi.org/10.1002/adma.201705713
16. Wang, X., Wang, T.Y., Borovilas, J., et al.: Vertically-aligned nanostructures for electrochemical energy storage. Nano Res. **12**, 2002–2017 (2019). https://doi.org/10.1007/s12274-019-2392-x
17. Lu, L.L., Lu, Y.Y., Xiao, Z.J., et al.: Wood-inspired high-performance ultrathick bulk battery electrodes. Adv. Mater. **30**, 1706745 (2018). https://doi.org/10.1002/adma.201706745
18. Chen, C.J., Zhang, Y., Li, Y.J., et al.: Highly conductive, lightweight, low-tortuosity carbon frameworks as ultrathick 3D current collectors. Adv. Energy Mater. **7**, 1700595 (2017). https://doi.org/10.1002/aenm.201700595
19. Jian, Z.L., Luo, W., Ji, X.L.: Carbon electrodes for K-ion batteries. J. Am. Chem. Soc. **137**, 11566–11569 (2015). https://doi.org/10.1021/jacs.5b06809
20. Choi, J.W., Aurbach, D.: Promise and reality of post-lithium-ion batteries with high energy densities. Nat. Rev. Mater. **1**, 16013 (2016). https://doi.org/10.1038/natrevmats.2016.13
21. Liu, M.Q., Xu, M., Xue, Y.F., et al.: Efficient capacitive deionization using natural basswood-derived, freestanding, hierarchically porous carbon electrodes. ACS Appl. Mater. Interfaces **10**, 31260–31270 (2018). https://doi.org/10.1021/acsami.8b08232
22. Wang, R.H., Cui, W.S., Chu, F.L., et al.: Lithium metal anodes: present and future. J. Energy Chem. **48**, 145–159 (2020). https://doi.org/10.1016/j.jechem.2019.12.024
23. Chen, R., Yu, M., Sahu, R.P., et al.: The development of pseudocapacitor electrodes and devices with high active mass loading. Adv. Energy Mater. **10**, 1903848 (2020). https://doi.org/10.1002/aenm.201903848
24. Choi, S., Jung, D.S., Choi, J.W.: Scalable fracture-free SiOC glass coating for robust silicon nanoparticle anodes in lithium secondary batteries. Nano Lett. **14**, 7120–7125 (2014). https://doi.org/10.1021/nl503620z
25. Li, X.L., Peng, W.X., Tian, R.Z., et al.: Excellent performance single-crystal NCM cathode under high mass loading for all-solid-state lithium batteries. Electrochim. Acta **363**, 137185 (2020). https://doi.org/10.1016/j.electacta.2020.137185
26. Chen, Y., Zhou, Z.L., Li, N., et al.: Thick electrodes upon biomass-derivative carbon current collectors: high-areal capacity positive electrodes for aluminum-ion batteries. Electrochim. Acta **323**, 134805 (2019). https://doi.org/10.1016/j.electacta.2019.134805
27. Black, J.M., Andreas, H.A.: Pore shape affects spontaneous charge redistribution in small pores. J. Phys. Chem. C **114**, 12030–12038 (2010). https://doi.org/10.1021/jp103766q
28. Ervin, M.H.: Etching holes in graphene supercapacitor electrodes for faster performance. Nanotechnology **26**, 234003 (2015). https://doi.org/10.1088/0957-4484/26/23/234003
29. Chmiola, J., Yushin, G., Gogotsi, Y., et al.: Anomalous increase in carbon capacitance at pore sizes less than 1 nanometer. Science **313**, 1760–1763 (2006). https://doi.org/10.1126/science.1132195
30. Merlet, C., Péan, C., Rotenberg, B., et al.: Highly confined ions store charge more efficiently in supercapacitors. Nat. Commun. **4**, 2701 (2013). https://doi.org/10.1038/ncomms3701
31. Kondrat, S., Georgi, N., Fedorov, M.V., et al.: A superionic state in nano-porous double-layer capacitors: insights from Monte Carlo simulations. Phys. Chem. Chem. Phys. **13**, 11359–11366 (2011). https://doi.org/10.1039/c1cp20798a
32. Urita, K., Ide, N., Isobe, K., et al.: Enhanced electric double-layer capacitance by desolvation of lithium ions in confined nanospaces of microporous carbon. ACS Nano **8**, 3614–3619 (2014). https://doi.org/10.1021/nn500169k
33. Prehal, C., Weingarth, D., Perre, E., et al.: Tracking the structural arrangement of ions in carbon supercapacitor nanopores using in situ small-angle X-ray scattering. Energy Environ. Sci. **8**, 1725–1735 (2015). https://doi.org/10.1039/C5EE00488H
34. Galhena, D.T.L., Bayer, B.C., Hofmann, S., et al.: Understanding capacitance variation in sub-nanometer pores by in situ tuning of interlayer constrictions. ACS Nano **10**, 747–754 (2016). https://doi.org/10.1021/acsnano.5b05819
35. Centeno, T.A., Sereda, O., Stoeckli, F.: Capacitance in carbon pores of 0.7 to 15 nm: a regular pattern. Phys. Chem. Chem. Phys. **13**, 12403–12406 (2011). https://doi.org/10.1039/C1CP20748B
36. Zhi, J., Wang, Y.F., Deng, S., et al.: Study on the relation between pore size and supercapacitance in mesoporous carbon electrodes with silica-supported carbon nanomembranes. RSC Adv. **4**, 40296–40300 (2014). https://doi.org/10.1039/C4RA06260D
37. Ebner, M., Chung, D.W., García, R.E., et al.: Tortuosity anisotropy in lithium-ion battery electrodes. Adv. Energy Mater. **4**, 1301278 (2014). https://doi.org/10.1002/aenm.201301278
38. Gao, H., Wu, Q., Hu, Y.X., et al.: Revealing the rate-limiting Li-ion diffusion pathway in ultrathick electrodes for Li-ion batteries. J. Phys. Chem. Lett. **9**, 5100–5104 (2018). https://doi.org/10.1021/acs.jpclett.8b02229
39. Ogihara, N., Itou, Y., Sasaki, T., et al.: Impedance spectroscopy characterization of porous electrodes under different electrode thickness using a symmetric cell for high-performance lithium-ion batteries. J. Phys. Chem. C **119**, 4612–4619 (2015). https://doi.org/10.1021/jp512564f
40. Hou, S., Gao, T., Li, X.G., et al.: Operando probing ion and electron transport in porous electrodes. Nano Energy **67**, 104254 (2020). https://doi.org/10.1016/j.nanoen.2019.104254
41. Du, Z.J., Wood, D.L., Daniel, C., et al.: Understanding limiting factors in thick electrode performance as applied to high energy density Li-ion batteries. J. Appl. Electrochem. **47**, 405–415 (2017). https://doi.org/10.1007/s10800-017-1047-4
42. Ike, I.S., Sigalas, I., Iyuke, S.E.: Modelling and optimization of electrodes utilization in symmetric electrochemical capacitors for high energy and power. J. Energy Storage **12**, 261–275 (2017). https://doi.org/10.1016/j.est.2017.05.006
43. Sun, N., Zhu, Q.Z., Anasori, B., et al.: MXene-bonded flexible hard carbon film as anode for stable Na/K-ion storage. Adv. Funct. Mater. **29**, 1906282 (2019). https://doi.org/10.1002/adfm.201906282
44. Higgins, T.M., Park, S.H., King, P.J., et al.: A commercial conducting polymer as both binder and conductive additive for silicon nanoparticle-based lithium-ion battery negative electrodes. ACS Nano **10**, 3702–3713 (2016). https://doi.org/10.1021/acsnano.6b00218
45. Liu, L., Zhao, H.P., Wang, Y., et al.: Evaluating the role of nanostructured current collectors in energy storage capability of supercapacitor electrodes with thick electroactive materials layers. Adv. Funct. Mater. **28**, 1705107 (2018). https://doi.org/10.1002/adfm.201705107
46. Hasegawa, G., Deguchi, T., Kanamori, K., et al.: High-level doping of nitrogen, phosphorus, and sulfur into activated carbon monoliths and their electrochemical capacitances. Chem. Mater. **27**, 4703–4712 (2015). https://doi.org/10.1021/acs.chemmater.5b01349
47. Wang, Y., Fu, X.W., Zheng, M., et al.: Strategies for building robust traffic networks in advanced energy storage devices: a focus on composite electrodes. Adv. Mater. **31**, 1804204 (2019). https://doi.org/10.1002/adma.201804204

48. Liu, T., Zhang, F., Song, Y., et al.: Revitalizing carbon supercapacitor electrodes with hierarchical porous structures. J. Mater. Chem. A **5**, 17705–17733 (2017). https://doi.org/10.1039/C7TA05646J
49. Dai, Y.H., Li, Q.D., Tan, S.S., et al.: Nanoribbons and nanoscrolls intertwined three-dimensional vanadium oxide hydrogels for high-rate lithium storage at high mass loading level. Nano Energy **40**, 73–81 (2017). https://doi.org/10.1016/j.nanoen.2017.08.011
50. Yao, B., Chandrasekaran, S., Zhang, H.Z., et al.: 3D-printed structure boosts the kinetics and intrinsic capacitance of pseudocapacitive graphene aerogels. Adv. Mater. **32**, 1906652 (2020). https://doi.org/10.1002/adma.201906652
51. Hao, Z.B., He, X.C., Li, H.D., et al.: Vertically aligned and ordered arrays of 2D MCo_2S_4@Metal with ultrafast ion/electron transport for thickness-independent pseudocapacitive energy storage. ACS Nano **14**, 12719–12731 (2020). https://doi.org/10.1021/acsnano.0c02973
52. Yi, H.M., Li, D., Lv, Z., et al.: Constructing high-performance 3D porous self-standing electrodes with various morphologies and shapes by a flexible phase separation-derived method. J. Mater. Chem. A **7**, 22550–22558 (2019). https://doi.org/10.1039/C9TA08845H
53. Liu, Y.W., Zhou, T.F., Zheng, Y., et al.: Local electric field facilitates high-performance Li-ion batteries. ACS Nano **11**, 8519–8526 (2017). https://doi.org/10.1021/acsnano.7b04617
54. Li, Z., Zhang, C.Z., Han, F., et al.: Towards high-volumetric performance of Na/Li-ion batteries: a better anode material with molybdenum pentachloride-graphite intercalation compounds ($MoCl_5$-GICs). J. Mater. Chem. A **8**, 2430–2438 (2020). https://doi.org/10.1039/C9TA12651A
55. Chen, C.J., Zhang, Y., Li, Y.J., et al.: All-wood, low tortuosity, aqueous, biodegradable supercapacitors with ultra-high capacitance. Energy Environ. Sci. **10**, 538–545 (2017). https://doi.org/10.1039/c6ee03716j
56. Li, H., Peng, L., Wu, D.B., et al.: Ultrahigh-capacity and fire-resistant $LiFePO_4$-based composite cathodes for advanced lithium-ion batteries. Adv. Energy Mater. **9**, 1802930 (2019). https://doi.org/10.1002/aenm.201802930
57. Zhang, Q.T., Yu, Z.L., Du, P., et al.: Carbon nanomaterials used as conductive additives in lithium ion batteries. Recent Patents Nanotechnol. **4**, 100–110 (2010). https://doi.org/10.2174/187221010791208803
58. Bitsch, B., Gallasch, T., Schroeder, M., et al.: Capillary suspensions as beneficial formulation concept for high energy density Li-ion battery electrodes. J. Power Sources **328**, 114–123 (2016). https://doi.org/10.1016/j.jpowsour.2016.07.102
59. Karkar, Z., Mazouzi, D., Hernandez, C.R., et al.: Threshold-like dependence of silicon-based electrode performance on active mass loading and nature of carbon conductive additive. Electrochim. Acta **215**, 276–288 (2016). https://doi.org/10.1016/j.electacta.2016.08.118
60. Kuang, Y.D., Chen, C.J., Pastel, G., et al.: Conductive cellulose nanofiber enabled thick electrode for compact and flexible energy storage devices. Adv. Energy Mater. **8**, 1802398 (2018). https://doi.org/10.1002/aenm.201802398
61. Yu, L.Y., Hu, L.F., Anasori, B., et al.: MXene-bonded activated carbon as a flexible electrode for high-performance supercapacitors. ACS Energy Lett. **3**, 1597–1603 (2018). https://doi.org/10.1021/acsenergylett.8b00718
62. Fan, Z.M., Wang, Y.S., Xie, Z.M., et al.: Modified MXene/holey graphene films for advanced supercapacitor electrodes with superior energy storage. Adv. Sci. **5**, 1800750 (2018). https://doi.org/10.1002/advs.201800750
63. Wang, B., Li, X.L., Luo, B., et al.: Intertwined network of Si/C nanocables and carbon nanotubes as lithium-ion battery anodes. ACS Appl. Mater. Interfaces **5**, 6467–6472 (2013). https://doi.org/10.1021/am402022n
64. Shi, Y., Zhou, X.Y., Yu, G.H.: Material and structural design of novel binder systems for high-energy, high-power lithium-ion batteries. Acc. Chem. Res. **50**, 2642–2652 (2017). https://doi.org/10.1021/acs.accounts.7b00402
65. Ryu, J., Kim, S., Kim, J., et al.: Room-temperature crosslinkable natural polymer binder for high-rate and stable silicon anodes. Adv. Funct. Mater. **30**, 1908433 (2020). https://doi.org/10.1002/adfm.201908433
66. Yue, Y., Liang, H.: 3D current collectors for lithium-ion batteries: a topical review. Small Methods **2**, 1800056 (2018). https://doi.org/10.1002/smtd.201800056
67. Zheng, J.X., Zhao, Q., Liu, X., et al.: Nonplanar electrode architectures for ultrahigh areal capacity batteries. ACS Energy Lett. **4**, 271–275 (2019). https://doi.org/10.1021/acsenergylett.8b02131
68. de las Casas, C., Li, W.Z.: A review of application of carbon nanotubes for lithium ion battery anode material. J. Power Sources **208**, 74–85 (2012). https://doi.org/10.1016/j.jpowsour.2012.02.013
69. Park, S.H., King, P.J., Tian, R.Y., et al.: High areal capacity battery electrodes enabled by segregated nanotube networks. Nat. Energy **4**, 560–567 (2019). https://doi.org/10.1038/s41560-019-0398-y
70. Nguyen, B.P.N., Kumar, N.A., Gaubicher, J., et al.: Nanosilicon-based thick negative composite electrodes for lithium batteries with graphene as conductive additive. Adv. Energy Mater. **3**, 1351–1357 (2013). https://doi.org/10.1002/aenm.201300330
71. Ke, L., Lv, W., Su, F.Y., et al.: Electrode thickness control: precondition for quite different functions of graphene conductive additives in $LiFePO_4$ electrode. Carbon **92**, 311–317 (2015). https://doi.org/10.1016/j.carbon.2015.04.064
72. Zhang, C.J., Park, S.H., Seral-Ascaso, A., et al.: High capacity silicon anodes enabled by MXene viscous aqueous ink. Nat. Commun. **10**, 849 (2019). https://doi.org/10.1038/s41467-019-08383-y
73. Zang, Y.H., Du, J., Du, Y.F., et al.: The migration of styrene butadiene latex during the drying of coating suspensions: when and how does migration of colloidal particles occur? Langmuir **26**, 18331–18339 (2010). https://doi.org/10.1021/la103675f
74. Müller, M., Pfaffmann, L., Jaiser, S., et al.: Investigation of binder distribution in graphite anodes for lithium-ion batteries. J. Power Sources **340**, 1–5 (2017). https://doi.org/10.1016/j.jpowsour.2016.11.051
75. Bitla, S., Tripp, C.P., Bousfield, D.W.: A Raman spectroscopic study of migration in paper coatings. J. Pulp Pap. Sci. **29**, 382–385 (2003)
76. Landesfeind, J., Eldiven, A., Gasteiger, H.A.: Influence of the binder on lithium ion battery electrode tortuosity and performance. J. Electrochem. Soc. **165**, A1122–A1128 (2018). https://doi.org/10.1149/2.0971805jes
77. Shim, J., Kostecki, R., Richardson, T., et al.: Electrochemical analysis for cycle performance and capacity fading of a lithium-ion battery cycled at elevated temperature. J. Power Sources **112**, 222–230 (2002). https://doi.org/10.1016/S0378-7753(02)00363-4
78. Mazouzi, D., Lestriez, B., Roué, L., et al.: Silicon composite electrode with high capacity and long cycle life. Electrochem. Solid-State Lett. **12**, A215 (2009). https://doi.org/10.1149/1.3212894
79. Ibing, L., Gallasch, T., Schneider, P., et al.: Towards water based ultra-thick Li ion battery electrodes: a binder approach. J. Power Sources **423**, 183–191 (2019). https://doi.org/10.1016/j.jpowsour.2019.03.020

80. Lee, J.H., Paik, U., Hackley, V.A., et al.: Effect of poly(acrylic acid) on adhesion strength and electrochemical performance of natural graphite negative electrode for lithium-ion batteries. J. Power Sources **161**, 612–616 (2006). https://doi.org/10.1016/j.jpowsour.2006.03.087
81. Michael, M.S., Jacob, M.M.E., Prabaharan, S.R.S., et al.: Enhanced lithium ion transport in PEO-based solid polymer electrolytes employing a novel class of plasticizers. Solid State Ionics **98**, 167–174 (1997). https://doi.org/10.1016/S0167-2738(97)00117-3
82. Shi, H., Zhao, Y., Dong, X., et al.: Frustrated crystallisation and hierarchical self-assembly behaviour of comb-like polymers. Chem. Soc. Rev. **42**, 2075–2099 (2013). https://doi.org/10.1039/c2cs35350d
83. Cao, P.F., Naguib, M., Du, Z.J., et al.: Effect of binder architecture on the performance of silicon/graphite composite anodes for lithium ion batteries. ACS Appl. Mater. Interfaces **10**, 3470–3478 (2018). https://doi.org/10.1021/acsami.7b13205
84. Zhou, Z.L., Li, N., Yang, Y.Z., et al.: Ultra-lightweight 3D carbon current collectors: constructing all-carbon electrodes for stable and high energy density dual-ion batteries. Adv. Energy Mater. **8**, 1801439 (2018). https://doi.org/10.1002/aenm.201801439
85. Li, N., Xin, Y.D., Chen, H.S., et al.: Thickness evolution of graphite-based cathodes in the dual ion batteries via in operando optical observation. J. Energy Chem. **29**, 122–128 (2019). https://doi.org/10.1016/j.jechem.2018.03.003
86. Singh, M., Kaiser, J., Hahn, H.: Thick electrodes for high energy lithium ion batteries. J. Electrochem. Soc. **162**, A1196–A1201 (2015). https://doi.org/10.1149/2.0401507jes
87. Yang, G.F., Song, K.Y., Joo, S.K.: Ultra-thick Li-ion battery electrodes using different cell size of metal foam current collectors. RSC Adv. **5**, 16702–16706 (2015). https://doi.org/10.1039/C4RA14485F
88. Zhao, H.P., Lei, Y.: 3D nanostructures for the next generation of high-performance nanodevices for electrochemical energy conversion and storage. Adv. Energy Mater. **10**, 2001460 (2020). https://doi.org/10.1002/aenm.202001460
89. Wang, H., Shao, Y., Mei, S.L., et al.: Polymer-derived heteroatom-doped porous carbon materials. Chem. Rev. **120**, 9363–9419 (2020). https://doi.org/10.1021/acs.chemrev.0c00080
90. Liu, M.Q., Huo, S.L., Xu, M., et al.: Structural engineering of N/S co-doped carbon material as high-performance electrode for supercapacitors. Electrochim. Acta **274**, 389–399 (2018). https://doi.org/10.1016/j.electacta.2018.04.084
91. Jin, H.L., Feng, X., Li, J., et al.: Heteroatom-doped porous carbon materials with unprecedented high volumetric capacitive performance. Angew. Chem. Int. Ed. **58**, 2397–2401 (2019). https://doi.org/10.1002/anie.201813686
92. Ghosh, S., Barg, S., Jeong, S.M., et al.: Heteroatom-doped and oxygen-functionalized nanocarbons for high-performance supercapacitors. Adv. Energy Mater. **10**, 2001239 (2020). https://doi.org/10.1002/aenm.202001239
93. Pan, Z.H., Zhi, H.Z., Qiu, Y.C., et al.: Achieving commercial-level mass loading in ternary-doped holey graphene hydrogel electrodes for ultrahigh energy density supercapacitors. Nano Energy **46**, 266–276 (2018). https://doi.org/10.1016/j.nanoen.2018.02.007
94. Zhang, L.P., Niu, J.B., Dai, L.M., et al.: Effect of microstructure of nitrogen-doped graphene on oxygen reduction activity in fuel cells. Langmuir **28**, 7542–7550 (2012). https://doi.org/10.1021/la2043262
95. Kong, X.K., Chen, Q.W., Sun, Z.Y.: Enhanced oxygen reduction reactions in fuel cells on H-decorated and B-substituted graphene. ChemPhysChem **14**, 514–519 (2013). https://doi.org/10.1002/cphc.201200918
96. Denis, P.A., Faccio, R., Mombru, A.W.: Is it possible to dope single-walled carbon nanotubes and graphene with sulfur? ChemPhysChem **10**, 715–722 (2009). https://doi.org/10.1002/cphc.200800592
97. Denis, P.A.: Band gap opening of monolayer and bilayer graphene doped with aluminium, silicon, phosphorus, and sulfur. Chem. Phys. Lett. **492**, 251–257 (2010). https://doi.org/10.1016/j.cplett.2010.04.038
98. Kong, X.K., Chen, C.L., Chen, Q.W.: Doped graphene for metal-free catalysis. Chem. Soc. Rev. **43**, 2841–2857 (2014). https://doi.org/10.1039/c3cs60401b
99. Lai, F.L., Feng, J.R., Heil, T., et al.: Strong metal oxide-support interactions in carbon/hematite nanohybrids activate novel energy storage modes for ionic liquid-based supercapacitors. Energy Storage Mater. **20**, 188–195 (2019). https://doi.org/10.1016/j.ensm.2019.04.035
100. Sahoo, G., Polaki, S.R., Ghosh, S., et al.: Plasma-tuneable oxygen functionalization of vertical graphenes enhance electrochemical capacitor performance. Energy Storage Mater. **14**, 297–305 (2018). https://doi.org/10.1016/j.ensm.2018.05.011
101. Pender, J., Guerrera, J.V., Wygant, B.R., et al.: Carbon nitride transforms into a high lithium storage capacity nitrogen-rich carbon. ACS Nano **13**, 9279–9291 (2019). https://doi.org/10.1021/acsnano.9b03861
102. Kumar, R., Sahoo, S., Joanni, E., et al.: Heteroatom doped graphene engineering for energy storage and conversion. Mater. Today **39**, 47–65 (2020). https://doi.org/10.1016/j.mattod.2020.04.010
103. Sun, Q., He, B., Zhang, X.Q., et al.: Engineering of hollow core-shell interlinked carbon spheres for highly stable lithium-sulfur batteries. ACS Nano **9**, 8504–8513 (2015). https://doi.org/10.1021/acsnano.5b03488
104. Lv, Q., Liu, Y., Ma, T.Y., et al.: Hollow structured silicon anodes with stabilized solid electrolyte interphase film for lithium-ion batteries. ACS Appl. Mater. Interfaces **7**, 23501–23506 (2015). https://doi.org/10.1021/acsami.5b05970
105. Liu, N., Lu, Z.D., Zhao, J., et al.: A pomegranate-inspired nanoscale design for large-volume-change lithium battery anodes. Nat. Nanotechnol. **9**, 187–192 (2014). https://doi.org/10.1038/nnano.2014.6
106. Pan, L., Huang, H.J., Zhong, M., et al.: Hydrogel-derived foams of nitrogen-doped carbon loaded with Sn nanodots for high-mass-loading Na-ion storage. Energy Storage Mater. **16**, 519–526 (2019). https://doi.org/10.1016/j.ensm.2018.09.010
107. Yao, H.B., Zheng, G.Y., Li, W.Y., et al.: Crab shells as sustainable templates from nature for nanostructured battery electrodes. Nano Lett. **13**, 3385–3390 (2013). https://doi.org/10.1021/nl401729r
108. Zheng, Y.H., Lu, Y.X., Qi, X.G., et al.: Superior electrochemical performance of sodium-ion full-cell using poplar wood derived hard carbon anode. Energy Storage Mater. **18**, 269–279 (2019). https://doi.org/10.1016/j.ensm.2018.09.002
109. Wang, B., Ryu, J., Choi, S., et al.: Folding graphene film yields high areal energy storage in lithium-ion batteries. ACS Nano **12**, 1739–1746 (2018). https://doi.org/10.1021/acsnano.7b08489
110. Xu, X.M., Wu, P.J., Li, Q., et al.: Realizing stable lithium and sodium storage with high areal capacity using novel nanosheet-assembled compact CaV_4O_9 microflowers. Nano Energy **50**, 606–614 (2018). https://doi.org/10.1016/j.nanoen.2018.06.012
111. Zhu, C., Liu, T., Qian, F., et al.: Supercapacitors based on three-dimensional hierarchical graphene aerogels with periodic macropores. Nano Lett. **16**, 3448–3456 (2016). https://doi.org/10.1021/acs.nanolett.5b04965
112. Zhu, C., Han, T.Y., Duoss, E.B., et al.: Highly compressible 3D periodic graphene aerogel microlattices. Nat. Commun. **6**, 6962 (2015). https://doi.org/10.1038/ncomms7962

113. Zhao, Z.D., Sun, M.Q., Chen, W.J., et al.: Sandwich, vertical-channeled thick electrodes with high rate and cycle performance. Adv. Funct. Mater. **29**, 1809196 (2019). https://doi.org/10.1002/adfm.201809196
114. Zhu, Y., Ju, Z.Y., Zhang, X., et al.: Evaporation-induced vertical alignment enabling directional ion transport in a 2D-nanosheet-based battery electrode. Adv. Mater. **32**, 1907941 (2020). https://doi.org/10.1002/adma.201907941
115. Bai, Y., Zhou, X.Z., Zhan, C., et al.: 3D hierarchical nanoflake/micro-flower iron fluoride with hydration water induced tunnels for secondary lithium battery cathodes. Nano Energy **32**, 10–18 (2017). https://doi.org/10.1016/j.nanoen.2016.12.017
116. Ni, W., Xue, Y.F., Zang, X.G., et al.: Fluorine doped cagelike carbon electrocatalyst: an insight into the structure-enhanced CO selectivity for CO_2 reduction at high overpotential. ACS Nano **14**, 2014–2023 (2020). https://doi.org/10.1021/acsnano.9b08528
117. Zang, X.G., Xue, Y.F., Ni, W., et al.: Enhanced electrosorption ability of carbon nanocages as an advanced electrode material for capacitive deionization. ACS Appl. Mater. Interfaces **12**, 2180–2190 (2020). https://doi.org/10.1021/acsami.9b12744
118. Li, Y., Bai, Y., Wu, C., et al.: Three-dimensional fusiform hierarchical micro/nano $Li_{1.2}Ni_{0.2}Mn_{0.6}O_2$ with a preferred orientation (110) plane as a high energy cathode material for lithium-ion batteries. J. Mater. Chem. A **4**, 5942–5951 (2016). https://doi.org/10.1039/C6TA00460A
119. Zhu, J., Shan, Y., Wang, T., et al.: A hyperaccumulation pathway to three-dimensional hierarchical porous nanocomposites for highly robust high-power electrodes. Nat. Commun. **7**, 13432 (2016). https://doi.org/10.1038/ncomms13432
120. Zhang, S., Zhu, J.Y., Qing, Y., et al.: Ultramicroporous carbons puzzled by graphene quantum dots: Integrated high gravimetric, volumetric, and areal capacitances for supercapacitors. Adv. Funct. Mater. **28**, 1805898 (2018). https://doi.org/10.1002/adfm.201805898
121. Dutta, D., Jiang, J.Y., Jamaluddin, A., et al.: Nanocatalyst-assisted fine tailoring of pore structure in holey-graphene for enhanced performance in energy storage. ACS Appl. Mater. Interfaces **11**, 36560–36570 (2019). https://doi.org/10.1021/acsami.9b09927
122. Fu, K., Yao, Y.G., Dai, J.Q., et al.: Progress in 3D printing of carbon materials for energy-related applications. Adv. Mater. **29**, 1603486 (2017). https://doi.org/10.1002/adma.201603486
123. Barg, S., Perez, F.M., Ni, N., et al.: Mesoscale assembly of chemically modified graphene into complex cellular networks. Nat. Commun. **5**, 4328 (2014). https://doi.org/10.1038/ncomms5328
124. Billaud, J., Bouville, F., Magrini, T., et al.: Magnetically aligned graphite electrodes for high-rate performance Li-ion batteries. Nat. Energy **1**, 16097 (2016). https://doi.org/10.1038/nenergy.2016.97
125. Li, Y., Wu, C., Bai, Y., et al.: Hierarchical mesoporous lithium-rich $Li[Li_{0.2}Ni_{0.2}Mn_{0.6}]O_2$ cathode material synthesized via ice templating for lithium-ion battery. ACS Appl. Mater. Interfaces **8**, 18832–18840 (2016). https://doi.org/10.1021/acsami.6b04687
126. Li, P., Wang, Y.N., Jeong, J.Y., et al.: Vertically constructed monolithic electrodes for sodium ion batteries: toward low tortuosity and high energy density. J. Mater. Chem. A **7**, 25985–25992 (2019). https://doi.org/10.1039/c9ta09644b
127. Kou, W., Li, X.C., Liu, Y., et al.: Triple-layered carbon-SiO_2 composite membrane for high energy density and long cycling Li-S batteries. ACS Nano **13**, 5900–5909 (2019). https://doi.org/10.1021/acsnano.9b01703
128. Zheng, Y., Zhou, T.F., Zhang, C.F., et al.: Boosted charge transfer in SnS/SnO_2 heterostructures: toward high rate capability for sodium-ion batteries. Angew. Chem. Int. Ed. **55**, 3408–3413 (2016). https://doi.org/10.1002/anie.201510978
129. Zheng, Q., Yi, H.M., Liu, W.Q., et al.: Improving the electrochemical performance of $Na_3V_2(PO_4)_3$ cathode in sodium ion batteries through Ce/V substitution based on rational design and synthesis optimization. Electrochim. Acta **238**, 288–297 (2017). https://doi.org/10.1016/j.electacta.2017.04.029
130. Zheng, Y., Zhou, T.F., Zhao, X.D., et al.: Atomic interface engineering and electric-field effect in ultrathin Bi_2MoO_6 nanosheets for superior lithium ion storage. Adv. Mater. **29**, 1700396 (2017). https://doi.org/10.1002/adma.201700396
131. Luo, W., Li, F., Li, Q.D., et al.: Heterostructured Bi_2S_3-Bi_2O_3 nanosheets with a built-in electric field for improved sodium storage. ACS Appl. Mater. Interfaces **10**, 7201–7207 (2018). https://doi.org/10.1021/acsami.8b01613
132. Zou, X., Su, J., Silva, R., et al.: Efficient oxygen evolution reaction catalyzed by low-density Ni-doped Co_3O_4 nanomaterials derived from metal-embedded graphitic C_3N_4. Chem Commun (Camb) **49**, 7522–7524 (2013). https://doi.org/10.1039/c3cc42891e
133. Ye, L., Zhou, Y.T., Zhao, Y.G., et al.: Engineering oxygen vacancy on iron oxides/hollow carbon cloth electrode toward stable lithium-ion batteries. Chem. Eng. J. **388**, 124229 (2020). https://doi.org/10.1016/j.cej.2020.124229
134. Wu, F., Liu, L., Yuan, Y.F., et al.: Expanding interlayer spacing of hard carbon by natural K^+ doping to boost Na-ion storage. ACS Appl. Mater. Interfaces **10**, 27030–27038 (2018). https://doi.org/10.1021/acsami.8b08380
135. Guo, D.L., Qin, J.W., Yin, Z.G., et al.: Achieving high mass loading of $Na_3V_2(PO_4)_3$@carbon on carbon cloth by constructing three-dimensional network between carbon fibers for ultralong cycle-life and ultrahigh rate sodium-ion batteries. Nano Energy **45**, 136–147 (2018). https://doi.org/10.1016/j.nanoen.2017.12.038
136. Chen, Y.J., Wang, Y.S., Wang, Z.P., et al.: Densification by compaction as an effective low-cost method to attain a high areal lithium storage capacity in a CNT@Co_3O_4 sponge. Adv. Energy Mater. **8**, 1702981 (2018). https://doi.org/10.1002/aenm.201702981
137. Chen, J.Z., Xu, J.L., Zhou, S., et al.: Nitrogen-doped hierarchically porous carbon foam: a free-standing electrode and mechanical support for high-performance supercapacitors. Nano Energy **25**, 193–202 (2016). https://doi.org/10.1016/j.nanoen.2016.04.037
138. Zhang, W., Wei, S., Wu, Y., et al.: Poly(ionic liquid)-derived graphitic nanoporous carbon membrane enables superior supercapacitive energy storage. ACS Nano **13**, 10261–10271 (2019). https://doi.org/10.1021/acsnano.9b03514
139. Wu, C.L., Zhang, S., Wu, W., et al.: Carbon nanotubes grown on the inner wall of carbonized wood tracheids for high-performance supercapacitors. Carbon **150**, 311–318 (2019). https://doi.org/10.1016/j.carbon.2019.05.032
140. Li, Y.J., Fu, K., Chen, C.J., et al.: Enabling high-areal-capacity lithium-sulfur batteries: designing anisotropic and low-tortuosity porous architectures. ACS Nano **11**, 4801–4807 (2017). https://doi.org/10.1021/acsnano.7b01172
141. Chodankar, N.R., Patil, S.J., Rama Raju, G.S., et al.: Two-dimensional materials for high-energy solid-state asymmetric pseudocapacitors with high mass loadings. Chemsuschem **13**, 1582–1592 (2020). https://doi.org/10.1002/cssc.201902339
142. Liu, T., Zhou, Z.P., Guo, Y.C., et al.: Block copolymer derived uniform mesopores enable ultrafast electron and ion transport at high mass loadings. Nat. Commun. **10**, 675 (2019). https://doi.org/10.1038/s41467-019-08644-w
143. Zhu, G.X., Xi, C.Y., Liu, Y.J., et al.: CN foam loaded with few-layer graphene nanosheets for high-performance supercapacitor

electrodes. J. Mater. Chem. A **3**, 7591–7599 (2015). https://doi.org/10.1039/c5ta00837a
144. Li, H., Yuan, D., Tang, C.H., et al.: Lignin-derived interconnected hierarchical porous carbon monolith with large areal/volumetric capacitances for supercapacitor. Carbon **100**, 151–157 (2016). https://doi.org/10.1016/j.carbon.2015.12.075
145. Wang, H., Min, S.X., Wang, Q., et al.: Nitrogen-doped nanoporous carbon membranes with Co/CoP Janus-type nanocrystals as hydrogen evolution electrode in both acidic and alkaline environments. ACS Nano **11**, 4358–4364 (2017). https://doi.org/10.1021/acsnano.7b01946
146. Shao, Y., Jiang, Z.P., Zhang, Y.J., et al.: All-poly(ionic liquid) membrane-derived porous carbon membranes: scalable synthesis and application for photothermal conversion in seawater desalination. ACS Nano **12**, 11704–11710 (2018). https://doi.org/10.1021/acsnano.8b07526
147. Shen, F., Luo, W., Dai, J.Q., et al.: Ultra-thick, low-tortuosity, and mesoporous wood carbon anode for high-performance sodium-ion batteries. Adv. Energy Mater. **6**, 1600377 (2016). https://doi.org/10.1002/aenm.201600377
148. Yousaf, M., Wang, Y.S., Chen, Y.J., et al.: A 3D trilayered CNT/$MoSe_2$/C heterostructure with an expanded $MoSe_2$ interlayer spacing for an efficient sodium storage. Adv. Energy Mater. **9**, 1900567 (2019). https://doi.org/10.1002/aenm.201900567
149. Liu, Y., Fang, Y.J., Zhao, Z.W., et al.: A ternary $Fe_{1-x}S$@Porous carbon nanowires/reduced graphene oxide hybrid film electrode with superior volumetric and gravimetric capacities for flexible sodium ion batteries. Adv. Energy Mater. **9**, 1803052 (2019). https://doi.org/10.1002/aenm.201803052
150. Li, P., Li, H., Han, D.L., et al.: Packing activated carbons into dense graphene network by capillarity for high volumetric performance supercapacitors. Adv. Sci. **6**, 1802355 (2019). https://doi.org/10.1002/advs.201802355
151. Han, D.L., Weng, Z., Li, P., et al.: Electrode thickness matching for achieving high-volumetric-performance lithium-ion capacitors. Energy Storage Mater. **18**, 133–138 (2019). https://doi.org/10.1016/j.ensm.2019.01.020
152. Cho, S.J., Choi, K.H., Yoo, J.T., et al.: Hetero-nanonet rechargeable paper batteries: toward ultrahigh energy density and origami foldability. Adv. Funct. Mater. **25**, 6029–6040 (2015). https://doi.org/10.1002/adfm.201502833
153. Kim, J.M., Park, C.H., Wu, Q.L., et al.: 1D building blocks-intermingled heteronanomats as a platform architecture for high-performance ultrahigh-capacity lithium-ion battery cathodes. Adv. Energy Mater. **6**, 1501594 (2016). https://doi.org/10.1002/aenm.201501594
154. Cabana, J., Casas-Cabanas, M., Omenya, F.O., et al.: Composition-structure relationships in the Li-ion battery electrode material $LiNi_{0.5}Mn_{1.5}O_4$. Chem. Mater. **24**, 2952–2964 (2012). https://doi.org/10.1021/cm301148d
155. de Biasi, L., Kondrakov, A.O., Geßwein, H., et al.: Between Scylla and Charybdis: balancing among structural stability and energy density of layered NCM cathode materials for advanced lithium-ion batteries. J. Phys. Chem. C **121**, 26163–26171 (2017). https://doi.org/10.1021/acs.jpcc.7b06363
156. Ashton, T.E., Baker, P.J., Bauer, D., et al.: Multiple diffusion pathways in $Li_xNi_{0.77}Co_{0.14}Al_{0.09}O_2$ (NCA) Li-ion battery cathodes. J. Mater. Chem. A **8**, 11545–11552 (2020). https://doi.org/10.1039/D0TA03809A
157. Kim, S.J., Naguib, M., Zhao, M.Q., et al.: High mass loading, binder-free MXene anodes for high areal capacity Li-ion batteries. Electrochim. Acta **163**, 246–251 (2015). https://doi.org/10.1016/j.electacta.2015.02.132
158. Liu, C.Y., Xu, F., Liu, Y.L., et al.: High mass loading ultrathick porous $Li_4Ti_5O_{12}$ electrodes with improved areal capacity fabricated via low temperature direct writing. Electrochim. Acta **314**, 81–88 (2019). https://doi.org/10.1016/j.electacta.2019.05.082
159. Haridas, A.K., Gangaja, B., Srikrishnarka, P., et al.: Spray pyrolysis-deposited nanoengineered TiO_2 thick films for ultra-high areal and volumetric capacity lithium ion battery applications. J. Power Sources **345**, 50–58 (2017). https://doi.org/10.1016/j.jpowsour.2017.01.136
160. Noelle, D.J., Wang, M., Qiao, Y.: Improved safety and mechanical characterizations of thick lithium-ion battery electrodes structured with porous metal current collectors. J. Power Sources **399**, 125–132 (2018). https://doi.org/10.1016/j.jpowsour.2018.07.076
161. Sotomayor, M.E., Torre-Gamarra, C.D.L., Levenfeld, B., et al.: Ultra-thick battery electrodes for high gravimetric and volumetric energy density Li-ion batteries. J. Power Sources **437**, 226923 (2019). https://doi.org/10.1016/j.jpowsour.2019.226923
162. Sun, C., Liu, S.R., Shi, X.L., et al.: 3D printing nanocomposite gel-based thick electrode enabling both high areal capacity and rate performance for lithium-ion battery. Chem. Eng. J. **381**, 122641 (2020). https://doi.org/10.1016/j.cej.2019.122641
163. Wang, J.W., Sun, Q., Gao, X.J., et al.: Toward high areal energy and power density electrode for Li-ion batteries via optimized 3D printing approach. ACS Appl. Mater. Interfaces **10**, 39794–39801 (2018). https://doi.org/10.1021/acsami.8b14797
164. Wang, Z.P., Wang, Y.S., Chen, Y.J., et al.: Reticulate dual-nanowire aerogel for multifunctional applications: a high-performance strain sensor and a high areal capacity rechargeable anode. Adv. Funct. Mater. **29**, 1807467 (2019). https://doi.org/10.1002/adfm.201807467
165. Pan, L., Wei, Y.C., Sun, Z.M., et al.: Layered hydrotalcite derived holey porous cobalt oxide nanosheets coated with nitrogen-doped carbon for high-mass-loading Li-ion storage. J. Mater. Chem. A **8**, 26150–26157 (2020). https://doi.org/10.1039/d0ta08789k
166. Tian, T., Lu, L.L., Yin, Y.C., et al.: Multiscale designed niobium titanium oxide anode for fast charging lithium ion batteries. Adv. Funct. Mater. **166**, 2007419 (2021). https://doi.org/10.1002/adfm.202007419
167. Wei, T.S., Ahn, B.Y., Grotto, J., et al.: 3D printing of customized Li-ion batteries with thick electrodes. Adv. Mater. **30**, 1703027 (2018). https://doi.org/10.1002/adma.201703027
168. Li, G., Ouyang, T., Xiong, T.Z., et al.: All-carbon-frameworks enabled thick electrode with exceptional high-areal-capacity for Li-Ion storage. Carbon **174**, 1–9 (2021). https://doi.org/10.1016/j.carbon.2020.12.018
169. Huang, C., Dontigny, M., Zaghib, K., et al.: Low-tortuosity and graded lithium ion battery cathodes by ice templating. J. Mater. Chem. A **7**, 21421–21431 (2019). https://doi.org/10.1039/C9TA07269A
170. Elango, R., Demortière, A., de Andrade, V., et al.: Thick binder-free electrodes for Li-ion battery fabricated using templating approach and spark plasma sintering reveals high areal capacity. Adv. Energy Mater. **8**, 1703031 (2018). https://doi.org/10.1002/aenm.201703031
171. Li, C.C., Zhu, L., Qi, S.Y., et al.: Ultrahigh-areal-capacity battery anodes enabled by free-standing vanadium Nitride@N-doped carbon/graphene architecture. ACS Appl. Mater. Interfaces **12**, 49607–49616 (2020). https://doi.org/10.1021/acsami.0c13859
172. Oh, D.Y., Nam, Y.J., Park, K.H., et al.: Slurry-fabricable Li+-conductive polymeric binders for practical all-solid-state lithium-ion batteries enabled by solvate ionic liquids. Adv. Energy Mater. **9**, 1802927 (2019). https://doi.org/10.1002/aenm.201802927
173. Peled, E., Patolsky, F., Golodnitsky, D., et al.: Tissue-like silicon nanowires-based three-dimensional anodes for high-capacity lithium ion batteries. Nano Lett. **15**, 3907–3916 (2015). https://doi.org/10.1021/acs.nanolett.5b00744

174. Abe, H., Kubota, M., Nemoto, M., et al.: High-capacity thick cathode with a porous aluminium current collector for lithium secondary batteries. J. Power Sources **334**, 78–85 (2016). https://doi.org/10.1016/j.jpowsour.2016.10.016
175. de la Torre-Gamarra, C., Sotomayor, M.E., Sanchez, J.Y., et al.: High mass loading additive-free $LiFePO_4$ cathodes with 500 µm thickness for high areal capacity Li-ion batteries. J. Power Sources **458**, 228033 (2020). https://doi.org/10.1016/j.jpowsour.2020.228033
176. Sotomayor, M.E., de la Torre-Gamarra, C., Bucheli, W., et al.: Additive-free $Li_4Ti_5O_{12}$ thick electrodes for Li-ion batteries with high electrochemical performance. J. Mater. Chem. A **6**, 5952–5961 (2018). https://doi.org/10.1039/c7ta10683a
177. Wu, F.X., Yushin, G.: Conversion cathodes for rechargeable lithium and lithium-ion batteries. Energy Environ. Sci. **10**, 435–459 (2017). https://doi.org/10.1039/c6ee02326f
178. Ni, Q., Zheng, L.M., Bai, Y., et al.: An extremely fast charging $Li_3V_2(PO_4)_3$ cathode at a 4.8 V cutoff voltage for Li-ion batteries. ACS Energy Lett. **5**, 1763–1770 (2020). https://doi.org/10.1021/acsenergylett.0c00702
179. Liu, H., Zhu, Z., Yan, Q., et al.: A disordered rock salt anode for fast-charging lithium-ion batteries. Nature **585**, 63–67 (2020). https://doi.org/10.1038/s41586-020-2637-6
180. Xu, J.T., Dou, Y.H., Wei, Z.X., et al.: Recent progress in graphite intercalation compounds for rechargeable metal (Li, Na, K, Al)-ion batteries. Adv. Sci. **4**, 1700146 (2017). https://doi.org/10.1002/advs.201700146
181. Ding, Y.L., Cano, Z.P., Yu, A.P., et al.: Automotive Li-ion batteries: current status and future perspectives. Electrochem. Energy Rev. **2**, 1–28 (2019). https://doi.org/10.1007/s41918-018-0022-z
182. Lu, Y., Yu, L., Lou, X.W.: Nanostructured conversion-type anode materials for advanced lithium-ion batteries. Chem **4**, 972–996 (2018). https://doi.org/10.1016/j.chempr.2018.01.003
183. Aravindan, V., Lee, Y.S., Madhavi, S.: Research progress on negative electrodes for practical Li-ion batteries: beyond carbonaceous anodes. Adv. Energy Mater. **5**, 1402225 (2015). https://doi.org/10.1002/aenm.201402225
184. Nitta, N., Wu, F.X., Lee, J.T., et al.: Li-ion battery materials: present and future. Mater. Today **18**, 252–264 (2015). https://doi.org/10.1016/j.mattod.2014.10.040
185. Chen, K.H., Namkoong, M.J., Goel, V., et al.: Efficient fast-charging of lithium-ion batteries enabled by laser-patterned three-dimensional graphite anode architectures. J. Power Sources **471**, 228475 (2020). https://doi.org/10.1016/j.jpowsour.2020.228475
186. Yuan, T., Tan, Z.P., Ma, C.R., et al.: Challenges of spinel $Li_4Ti_5O_{12}$ for lithium-ion battery industrial applications. Adv. Energy Mater. **7**, 1601625 (2017). https://doi.org/10.1002/aenm.201601625
187. Li, H., Guo, S.T., Wang, L.B., et al.: Thermally durable lithium-ion capacitors with high energy density from all hydroxyapatite nanowire-enabled fire-resistant electrodes and separators. Adv. Energy Mater. **9**, 1902497 (2019). https://doi.org/10.1002/aenm.201902497
188. Wang, Y., Luo, S.N., Chen, M., et al.: Uniformly confined germanium quantum dots in 3D ordered porous carbon framework for high-performance Li-ion battery. Adv. Funct. Mater. **30**, 2000373 (2020). https://doi.org/10.1002/adfm.202000373
189. Yan, Y.H., Xu, H.Y., Peng, C.X., et al.: 3D phosphorus-carbon electrode with aligned nanochannels promise high-areal-capacity and cyclability in lithium-ion battery. Appl. Surf. Sci. **489**, 734–740 (2019). https://doi.org/10.1016/j.apsusc.2019.05.329
190. Wang, L., Liu, T.F., Peng, X., et al.: Highly stretchable conductive glue for high-performance silicon anodes in advanced lithium-ion batteries. Adv. Funct. Mater. **28**, 1704858 (2018). https://doi.org/10.1002/adfm.201704858
191. Evanoff, K., Khan, J., Balandin, A.A., et al.: Towards ultrathick battery electrodes: aligned carbon nanotube-enabled architecture. Adv. Mater. **24**, 533–537 (2012). https://doi.org/10.1002/adma.201103044
192. Lim, E., Jo, C., Kim, H., et al.: Facile synthesis of Nb_2O_5@Carbon core-shell nanocrystals with controlled crystalline structure for high-power anodes in hybrid supercapacitors. ACS Nano **9**, 7497–7505 (2015). https://doi.org/10.1021/acsnano.5b02601
193. Wang, X.L., Li, G., Chen, Z., et al.: High-performance supercapacitors based on nanocomposites of Nb_2O_5 nanocrystals and carbon nanotubes. Adv. Energy Mater. **1**, 1089–1093 (2011). https://doi.org/10.1002/aenm.201100332
194. Wang, X., Yan, C.Y., Yan, J., et al.: Orthorhombic niobium oxide nanowires for next generation hybrid supercapacitor device. Nano Energy **11**, 765–772 (2015). https://doi.org/10.1016/j.nanoen.2014.11.020
195. Sun, H., Mei, L., Liang, J., et al.: Three-dimensional holey-graphene/niobia composite architectures for ultrahigh-rate energy storage. Science **356**, 599–604 (2017). https://doi.org/10.1126/science.aam5852
196. Sun, P.C., Davis, J., Cao, L.X., et al.: High capacity 3D structured tin-based electroplated Li-ion battery anodes. Energy Storage Mater. **17**, 151–156 (2019). https://doi.org/10.1016/j.ensm.2018.11.017
197. Zhao, Y.T., Huang, G.S., Li, Y.L., et al.: Three-dimensional carbon/ZnO nanomembrane foam as an anode for lithium-ion battery with long-life and high areal capacity. J. Mater. Chem. A **6**, 7227–7235 (2018). https://doi.org/10.1039/c8ta00940f
198. Kim, C., Hwang, G., Jung, J.W., et al.: Fast, scalable synthesis of micronized Ge_3N_4@C with a high tap density for excellent lithium storage. Adv. Funct. Mater. **27**, 1605975 (2017). https://doi.org/10.1002/adfm.201605975
199. Liang, J.F., Sun, H.T., Zhao, Z.P., et al.: Ultra-high areal capacity realized in three-dimensional holey graphene/SnO_2 composite anodes. iScience **19**, 728–736 (2019). https://doi.org/10.1016/j.isci.2019.08.025
200. Song, J.X., Zhou, M.J., Yi, R., et al.: Interpenetrated gel polymer binder for high-performance silicon anodes in lithium-ion batteries. Adv. Funct. Mater. **24**, 5904–5910 (2014). https://doi.org/10.1002/adfm.201401269
201. Luo, W., Chen, X.Q., Xia, Y., et al.: Surface and interface engineering of silicon-based anode materials for lithium-ion batteries. Adv. Energy Mater. **7**, 1701083 (2017). https://doi.org/10.1002/aenm.201701083
202. Zhou, M., Li, X.L., Wang, B., et al.: High-performance silicon battery anodes enabled by engineering graphene assemblies. Nano Lett. **15**, 6222–6228 (2015). https://doi.org/10.1021/acs.nanolett.5b02697
203. Koo, B., Kim, H., Cho, Y., et al.: A highly cross-linked polymeric binder for high-performance silicon negative electrodes in lithium ion batteries. Angew. Chem. Int. Ed. **51**, 8762–8767 (2012). https://doi.org/10.1002/anie.201201568
204. Bie, Y.T., Yang, J., Liu, X.L., et al.: Polydopamine wrapping silicon cross-linked with polyacrylic acid as high-performance anode for lithium-ion batteries. ACS Appl. Mater. Interfaces **8**, 2899–2904 (2016). https://doi.org/10.1021/acsami.5b10616
205. Wang, J., Meng, X.C., Fan, X.L., et al.: Scalable synthesis of defect abundant Si nanorods for high-performance Li-ion battery anodes. ACS Nano **9**, 6576–6586 (2015). https://doi.org/10.1021/acsnano.5b02565
206. Xu, Q., Li, J.Y., Sun, J.K., et al.: Watermelon-inspired Si/C microspheres with hierarchical buffer structures for densely compacted lithium-ion battery anodes. Adv. Energy Mater. **7**, 1601481 (2017). https://doi.org/10.1002/aenm.201601481
207. Xu, Q., Sun, J.K., Li, J.Y., et al.: Scalable synthesis of spherical Si/C granules with 3D conducting networks as ultrahigh loading

anodes in lithium-ion batteries. Energy Storage Mater. **12**, 54–60 (2018). https://doi.org/10.1016/j.ensm.2017.11.015
208. Li, X., Gu, M., Hu, S., et al.: Mesoporous silicon sponge as an anti-pulverization structure for high-performance lithium-ion battery anodes. Nat. Commun. **5**, 4105 (2014). https://doi.org/10.1038/ncomms5105
209. Lyu, Y.C., Wu, X., Wang, K., et al.: An overview on the advances of $LiCoO_2$ cathodes for lithium-ion batteries. Adv. Energy Mater. (2020). https://doi.org/10.1002/aenm.202000982
210. Wang, J.J., Sun, X.L.: Olivine $LiFePO_4$: the remaining challenges for future energy storage. Energy Environ. Sci. **8**, 1110–1138 (2015). https://doi.org/10.1039/C4EE04016C
211. Kang, Y.S., Kim, D.Y., Yoon, J., et al.: Shape control of hierarchical lithium cobalt oxide using biotemplates for connected nanoparticles. J. Power Sources **436**, 226836 (2019). https://doi.org/10.1016/j.jpowsour.2019.226836
212. Shi, B.H., Shang, Y.Y., Pei, Y., et al.: Low tortuous, highly conductive, and high-areal-capacity battery electrodes enabled by through-thickness aligned carbon fiber framework. Nano Lett. **20**, 5504–5512 (2020). https://doi.org/10.1021/acs.nanolett.0c02053
213. Wu, X.S., Xia, S.X., Huang, Y.Q., et al.: High-performance, low-cost, and dense-structure electrodes with high mass loading for lithium-ion batteries. Adv. Funct. Mater. **29**, 1903961 (2019). https://doi.org/10.1002/adfm.201903961
214. Li, Y., Chen, M.H., Liu, B., et al.: Heteroatom doping: an effective way to boost sodium ion storage. Adv. Energy Mater. **10**, 2000927 (2020). https://doi.org/10.1002/aenm.202000927
215. Lao, M.M., Zhang, Y., Luo, W.B., et al.: Alloy-based anode materials toward advanced sodium-ion batteries. Adv. Mater. **29**, 1700622 (2017). https://doi.org/10.1002/adma.201700622
216. Saurel, D., Orayech, B., Xiao, B.W., et al.: From charge storage mechanism to performance: a roadmap toward high specific energy sodium-ion batteries through carbon anode optimization. Adv. Energy Mater. **8**, 1703268 (2018). https://doi.org/10.1002/aenm.201703268
217. Xu, C.Y., Kou, X.D., Cao, B.K., et al.: Hierarchical graphene@TiO_2 sponges for sodium-ion storage with high areal capacity and robust stability. Electrochim. Acta **355**, 136782 (2020). https://doi.org/10.1016/j.electacta.2020.136782
218. Liu, L.L., Qi, X.G., Ma, Q., et al.: Toothpaste-like electrode: a novel approach to optimize the interface for solid-state sodium-ion batteries with ultralong cycle life. ACS Appl. Mater. Interfaces **8**, 32631–32636 (2016). https://doi.org/10.1021/acsami.6b11773
219. He, Y.W., Bai, P.X., Gao, S.Y., et al.: Marriage of an ether-based electrolyte with hard carbon anodes creates superior sodium-ion batteries with high mass loading. ACS Appl. Mater. Interfaces **10**, 41380–41388 (2018). https://doi.org/10.1021/acsami.8b15274
220. Fu, H., Xu, Z.W., Li, R.Z., et al.: Network carbon with macropores from apple pomace for stable and high areal capacity of sodium storage. ACS Sustain. Chem. Eng. **6**, 14751–14758 (2018). https://doi.org/10.1021/acssuschemeng.8b03297
221. Yang, T., Niu, X., Qian, T., et al.: Half and full sodium-ion batteries based on maize with high-loading density and long-cycle life. Nanoscale **8**, 15497–15504 (2016). https://doi.org/10.1039/c6nr04424g
222. Yu, S.C., Liu, Z.G., Tempel, H., et al.: Self-standing NASICON-type electrodes with high mass loading for fast-cycling all-phosphate sodium-ion batteries. J. Mater. Chem. A **6**, 18304–18317 (2018). https://doi.org/10.1039/C8TA07313A
223. Yousaf, M., Wang, Z.P., Wang, Y.S., et al.: Core-shell $FeSe_2$/C nanostructures embedded in a carbon framework as a free standing anode for a sodium ion battery. Small **16**, 2002200 (2020). https://doi.org/10.1002/smll.202002200
224. Liu, Y.P., He, X.Y., Hanlon, D., et al.: Liquid phase exfoliated MoS_2 nanosheets percolated with carbon nanotubes for high volumetric/areal capacity sodium-ion batteries. ACS Nano **10**, 8821–8828 (2016). https://doi.org/10.1021/acsnano.6b04577
225. Wang, H.Q., Wang, R.H., Song, Z.H., et al.: A novel aqueous Li+ (or Na^+)/Br^- hybrid-ion battery with super high areal capacity and energy density. J. Mater. Chem. A **7**, 13050–13059 (2019). https://doi.org/10.1039/C9TA03212F
226. Li, L., Zheng, Y., Zhang, S.L., et al.: Recent progress on sodium ion batteries: potential high-performance anodes. Energy Environ. Sci. **11**, 2310–2340 (2018). https://doi.org/10.1039/C8EE01023D
227. Li, Z.F., Zheng, Y., Liu, Q.Y., et al.: Recent advances in nanostructured metal phosphides as promising anode materials for rechargeable batteries. J. Mater. Chem. A **8**, 19113–19132 (2020). https://doi.org/10.1039/D0TA06533A
228. Li, Y., Xu, Y.H., Wang, Z.H., et al.: Stable carbon-selenium bonds for enhanced performance in tremella-like 2D chalcogenide battery anode. Adv. Energy Mater. **8**, 1800927 (2018). https://doi.org/10.1002/aenm.201800927
229. Wu, F., Zhang, M.H., Bai, Y., et al.: Lotus seedpod-derived hard carbon with hierarchical porous structure as stable anode for sodium-ion batteries. ACS Appl. Mater. Interfaces **11**, 12554–12561 (2019). https://doi.org/10.1021/acsami.9b01419
230. Wang, Q.D., Zhao, C.L., Lu, Y.X., et al.: Advanced nanostructured anode materials for sodium-ion batteries. Small **13**, 1701835 (2017). https://doi.org/10.1002/smll.201701835
231. Wang, Z.H., Wang, X.R., Bai, Y., et al.: Developing an interpenetrated porous and ultrasuperior hard-carbon anode via a promising molten-salt evaporation method. ACS Appl. Mater. Interfaces **12**, 2481–2489 (2020). https://doi.org/10.1021/acsami.9b18495
232. Li, Y., Yuan, Y.F., Bai, Y., et al.: Insights into the Na^+ storage mechanism of phosphorus-functionalized hard carbon as ultrahigh capacity anodes. Adv. Energy Mater. **8**, 1702781 (2018). https://doi.org/10.1002/aenm.201702781
233. Yu, K.H., Zhao, H.C., Wang, X.R., et al.: Hyperaccumulation route to Ca-rich hard carbon materials with cation self-incorporation and interlayer spacing optimization for high-performance sodium-ion batteries. ACS Appl. Mater. Interfaces **12**, 10544–10553 (2020). https://doi.org/10.1021/acsami.9b22745
234. Li, X., Sun, X.H., Hu, X.D., et al.: Review on comprehending and enhancing the initial Coulombic efficiency of anode materials in lithium-ion/sodium-ion batteries. Nano Energy **77**, 105143 (2020). https://doi.org/10.1016/j.nanoen.2020.105143
235. Xiong, P.X., Bai, P.X., Li, A., et al.: Bismuth Nanoparticle@Carbon composite anodes for ultralong cycle life and high-rate sodium-ion batteries. Adv. Mater. **31**, 1904771 (2019). https://doi.org/10.1002/adma.201904771
236. Han, L., Wang, J., Mu, X., et al.: Anisotropic, low-tortuosity and ultra-thick red P@C-Wood electrodes for sodium-ion batteries. Nanoscale **12**, 14642–14650 (2020). https://doi.org/10.1039/d0nr03059g
237. Park, J., Lee, M., Feng, D.W., et al.: Stabilization of hexaaminobenzene in a 2D conductive metal-organic framework for high power sodium storage. J. Am. Chem. Soc. **140**, 10315–10323 (2018). https://doi.org/10.1021/jacs.8b06020
238. Yu, K.H., Wang, X.R., Yang, H.Y., et al.: Insight to defects regulation on sugarcane waste-derived hard carbon anode for sodium-ion batteries. J. Energy Chem. **55**, 499–508 (2021). https://doi.org/10.1016/j.jechem.2020.07.025
239. Liu, X.X., Tan, Y.C., Liu, T.C., et al.: A simple electrode-level chemical presodiation route by solution spraying to improve the energy density of sodium-ion batteries. Adv. Funct. Mater. **29**, 1903795 (2019). https://doi.org/10.1002/adfm.201903795
240. Ni, Q., Dong, R.Q., Bai, Y., et al.: Superior sodium-storage behavior of flexible anatase TiO_2 promoted by oxygen vacancies.

Energy Storage Mater. **25**, 903–911 (2020). https://doi.org/10.1016/j.ensm.2019.09.001
241. Ni, Q., Bai, Y., Guo, S.N., et al.: Carbon nanofiber elastically confined nanoflowers: a highly efficient design for molybdenum disulfide-based flexible anodes toward fast sodium storage. ACS Appl. Mater. Interfaces **11**, 5183–5192 (2019). https://doi.org/10.1021/acsami.8b21729
242. Zhang, Z.Y., Yoshikawa, H., Awaga, K.: Monitoring the solid-state electrochemistry of Cu(2, 7-AQDC) (AQDC = anthraquinone dicarboxylate) in a lithium battery: coexistence of metal and ligand redox activities in a metal-organic framework. J. Am. Chem. Soc. **136**, 16112–16115 (2014). https://doi.org/10.1021/ja508197w
243. Sun, L., Campbell, M.G., Dincă, M.: Electrically conductive porous metal-organic frameworks. Angew. Chem. Int. Ed. **55**, 3566–3579 (2016). https://doi.org/10.1002/anie.201506219
244. Gao, L., Chen, S., Zhang, L.L., et al.: Self-supported $Na_{0.7}CoO_2$ nanosheet arrays as cathodes for high performance sodium ion batteries. J. Power Sources **396**, 379–385 (2018). https://doi.org/10.1016/j.jpowsour.2018.06.047
245. Gao, L., Chen, S., Zhang, L.L., et al.: High areal capacity $Na_{0.67}CoO_2$ bundle array cathode tailored for high-performance sodium-ion batteries. ChemElectroChem **6**, 947–952 (2019). https://doi.org/10.1002/celc.201900031
246. Wang, X.P., Wang, C.Y., Han, K., et al.: A synergistic Na-Mn-O composite cathodes for high-capacity Na-ion storage. Adv. Energy Mater. **8**, 1802180 (2018). https://doi.org/10.1002/aenm.201802180
247. Lv, Z., Ling, M.X., Yi, H.M., et al.: Electrode design for high-performance sodium-ion batteries: coupling nanorod-assembled $Na_3V_2(PO_4)_3$@C microspheres with a 3D conductive charge transport network. ACS Appl. Mater. Interfaces **12**, 13869–13877 (2020). https://doi.org/10.1021/acsami.9b22746
248. Xiang, X.D., Zhang, K., Chen, J.: Recent advances and prospects of cathode materials for sodium-ion batteries. Adv. Mater. **27**, 5343–5364 (2015). https://doi.org/10.1002/adma.201501527
249. Kang, S.M., Park, J.H., Jin, A.H., et al.: Na^+/vacancy disordered P2-$Na_{0.67}Co_{1-x}Ti_xO_2$: high-energy and high-power cathode materials for sodium ion batteries. ACS Appl. Mater. Interfaces **10**, 3562–3570 (2018). https://doi.org/10.1021/acsami.7b16077
250. Du, K., Zhu, J.Y., Hu, G.R., et al.: Exploring reversible oxidation of oxygen in a manganese oxide. Energy Environ. Sci. **9**, 2575–2577 (2016). https://doi.org/10.1039/c6ee01367h
251. Li, H., Bai, Y., Wu, F., et al.: Na-rich $Na_{3+x}V_{2-x}Ni_x(PO_4)_3$/C for sodium ion batteries: controlling the doping site and improving the electrochemical performances. ACS Appl. Mater. Interfaces **8**, 27779–27787 (2016). https://doi.org/10.1021/acsami.6b09898
252. Ni, Q., Bai, Y., Wu, F., et al.: Polyanion-type electrode materials for sodium-ion batteries. Adv. Sci. **4**, 1600275 (2017). https://doi.org/10.1002/advs.201600275
253. Wu, F., Zhu, N., Bai, Y., et al.: Unveil the mechanism of solid electrolyte interphase on $Na_3V_2(PO_4)_3$ formed by a novel $NaPF_6$/BMITFSI ionic liquid electrolyte. Nano Energy **51**, 524–532 (2018). https://doi.org/10.1016/j.nanoen.2018.07.003
254. Ni, Q., Bai, Y., Li, Y., et al.: 3D electronic channels wrapped large-sized $Na_3V_2(PO_4)_3$ as flexible electrode for sodium-ion batteries. Small **14**, 1702864 (2018). https://doi.org/10.1002/smll.201702864
255. Hwang, J.Y., Myung, S.T., Sun, Y.K.: Recent progress in rechargeable potassium batteries. Adv. Funct. Mater. **28**, 1802938 (2018). https://doi.org/10.1002/adfm.201802938
256. Kim, H., Kim, J.C., Bianchini, M., et al.: Recent progress and perspective in electrode materials for K-ion batteries. Adv. Energy Mater. **8**, 1702384 (2018). https://doi.org/10.1002/aenm.201702384
257. Wei, S.Y., Choudhury, S., Tu, Z.Y., et al.: Electrochemical interphases for high-energy storage using reactive metal anodes. Acc. Chem. Res. **51**, 80–88 (2018). https://doi.org/10.1021/acs.accounts.7b00484
258. Fan, L., Ma, R.F., Zhang, Q.F., et al.: Graphite anode for a potassium-ion battery with unprecedented performance. Angew. Chem. Int. Ed. **131**, 10610–10615 (2019). https://doi.org/10.1002/ange.201904258
259. Fan, L., Chen, S.H., Ma, R.F., et al.: Ultrastable potassium storage performance realized by highly effective solid electrolyte interphase layer. Small **14**, 1801806 (2018). https://doi.org/10.1002/smll.201801806
260. Wu, Z.B., Liang, G.M., Pang, W.K., et al.: Coupling topological insulator $SnSb_2Te_4$ nanodots with highly doped graphene for high-rate energy storage. Adv. Mater. **32**, 1905632 (2020). https://doi.org/10.1002/adma.201905632
261. Yao, K., Xu, Z.W., Ma, M., et al.: Densified metallic MoS_2/graphene enabling fast potassium-ion storage with superior gravimetric and volumetric capacities. Adv. Funct. Mater. (2020). https://doi.org/10.1002/adfm.202004244
262. Zhang, C., Lyu, R.Y., Lv, W., et al.: A lightweight 3D Cu nanowire network with phosphidation gradient as current collector for high-density nucleation and stable deposition of lithium. Adv. Mater. **31**, 1904991 (2019). https://doi.org/10.1002/adma.201904991
263. Sun, Z.W., Jin, S., Jin, H.C., et al.: Robust expandable carbon nanotube scaffold for ultrahigh-capacity lithium-metal anodes. Adv. Mater. **30**, 1800884 (2018). https://doi.org/10.1002/adma.201800884
264. Song, H.Y., Chen, X.L., Zheng, G.L., et al.: Dendrite-free composite Li anode assisted by Ag nanoparticles in a wood-derived carbon frame. ACS Appl. Mater. Interfaces **11**, 18361–18367 (2019). https://doi.org/10.1021/acsami.9b01694
265. Deng, W., Zhu, W.H., Zhou, X.F., et al.: Regulating capillary pressure to achieve ultralow areal mass loading metallic lithium anodes. Energy Storage Mater. **23**, 693–700 (2019). https://doi.org/10.1016/j.ensm.2019.02.027
266. Zheng, J., Kim, M.S., Tu, Z., et al.: Regulating electrodeposition morphology of lithium: towards commercially relevant secondary Li metal batteries. Chem. Soc. Rev. **49**, 2701–2750 (2020). https://doi.org/10.1039/c9cs00883g
267. Wu, F., Yuan, Y.X., Cheng, X.B., et al.: Perspectives for restraining harsh lithium dendrite growth: towards robust lithium metal anodes. Energy Storage Mater. **15**, 148–170 (2018). https://doi.org/10.1016/j.ensm.2018.03.024
268. Yuan, Y.X., Wu, F., Bai, Y., et al.: Regulating Li deposition by constructing LiF-rich host for dendrite-free lithium metal anode. Energy Storage Mater. **16**, 411–418 (2019). https://doi.org/10.1016/j.ensm.2018.06.022
269. Huang, A., Liu, H.D., Manor, O., et al.: Enabling rapid charging lithium metal batteries via surface acoustic wave-driven electrolyte flow. Adv. Mater. **32**, 1907516 (2020). https://doi.org/10.1002/adma.201907516
270. Kim, P.J., Pol, V.G.: High performance lithium metal batteries enabled by surface tailoring of polypropylene separator with a polydopamine/graphene layer. Adv. Energy Mater. **8**, 1802665 (2018). https://doi.org/10.1002/aenm.201802665
271. Liu, H.D., Yue, X.J., Xing, X., et al.: A scalable 3D lithium metal anode. Energy Storage Mater. **16**, 505–511 (2019). https://doi.org/10.1016/j.ensm.2018.09.021
272. Liu, H.D., Wang, X.F., Zhou, H.Y., et al.: Structure and solution dynamics of lithium methyl carbonate as a protective layer for lithium metal. ACS Appl. Energy Mater. **1**, 1864–1869 (2018). https://doi.org/10.1021/acsaem.8b00348
273. Zhou, H.Y., Yu, S.C., Liu, H.D., et al.: Protective coatings for lithium metal anodes: recent progress and future perspectives.

J. Power Sources **450**, 227632 (2020). https://doi.org/10.1016/j.jpowsour.2019.227632
274. Yu, L., Chen, S.R., Lee, H., et al.: A localized high-concentration electrolyte with optimized solvents and lithium difluoro(oxalate)borate additive for stable lithium metal batteries. ACS Energy Lett. **3**, 2059–2067 (2018). https://doi.org/10.1021/acsenergylett.8b00935
275. Zhang, C., Lv, W., Zhou, G.M., et al.: Vertically aligned lithiophilic CuO nanosheets on a Cu collector to stabilize lithium deposition for lithium metal batteries. Adv. Energy Mater. **8**, 1703404 (2018). https://doi.org/10.1002/aenm.201703404
276. Jin, C.B., Sheng, O.W., Luo, J.M., et al.: 3D lithium metal embedded within lithiophilic porous matrix for stable lithium metal batteries. Nano Energy **37**, 177–186 (2017). https://doi.org/10.1016/j.nanoen.2017.05.015
277. Zhang, Y., Luo, W., Wang, C., et al.: High-capacity, low-tortuosity, and channel-guided lithium metal anode. Proc. Natl. Acad. Sci. U. S. A. **114**, 3584–3589 (2017). https://doi.org/10.1073/pnas.1618871114
278. Yang, G., Tan, J., Jin, H., et al.: Creating effective nanoreactors on carbon nanotubes with mechanochemical treatments for high-areal-capacity sulfur cathodes and lithium anodes. Adv. Funct. Mater. **28**, 1800595 (2018). https://doi.org/10.1002/adfm.201800595
279. Yao, Y., Wang, H.Y., Yang, H., et al.: A dual-functional conductive framework embedded with TiN-VN heterostructures for highly efficient polysulfide and lithium regulation toward stable Li–S full batteries. Adv. Mater. **32**, 1905658 (2020). https://doi.org/10.1002/adma.201905658
280. Zhou, Z.F., Chen, B.B., Fang, T.T., et al.: A multifunctional separator enables safe and durable lithium/magnesium-sulfur batteries under elevated temperature. Adv. Energy Mater. **10**, 1902023 (2020). https://doi.org/10.1002/aenm.201902023
281. Chung, S.H., Manthiram, A.: Designing lithium-sulfur cells with practically necessary parameters. Joule **2**, 710–724 (2018). https://doi.org/10.1016/j.joule.2018.01.002
282. Fu, K.K., Gong, Y.H., Hitz, G.T., et al.: Three-dimensional bilayer garnet solid electrolyte based high energy density lithium metal–sulfur batteries. Energy Environ. Sci. **10**, 1568–1575 (2017). https://doi.org/10.1039/c7ee01004d
283. Peng, H.J., Huang, J.Q., Cheng, X.B., et al.: Review on high-loading and high-energy lithium–sulfur batteries. Adv. Energy Mater. **7**, 1700260 (2017). https://doi.org/10.1002/aenm.201700260
284. Hu, Y., Chen, W., Lei, T., et al.: Strategies toward high-loading lithium–sulfur battery. Adv. Energy Mater. **10**, 2000082 (2020). https://doi.org/10.1002/aenm.202000082
285. Rana, M., Ahad, S.A., Li, M., et al.: Review on areal capacities and long-term cycling performances of lithium sulfur battery at high sulfur loading. Energy Storage Mater. **18**, 289–310 (2019). https://doi.org/10.1016/j.ensm.2018.12.024
286. Qu, H.T., Zhang, J.J., Du, A.B., et al.: Multifunctional sandwich-structured electrolyte for high-performance lithium–sulfur batteries. Adv. Sci. **5**, 1700503 (2018). https://doi.org/10.1002/advs.201700503
287. Zhang, S.G., Ueno, K., Dokko, K., et al.: Recent advances in electrolytes for lithium–sulfur batteries. Adv. Energy Mater. **5**, 1500117 (2015). https://doi.org/10.1002/aenm.201500117
288. Chen, G.H., Zhang, K., Liu, Y.R., et al.: Flame-retardant gel polymer electrolyte and interface for quasi-solid-state sodium ion batteries. Chem. Eng. J. **401**, 126065 (2020). https://doi.org/10.1016/j.cej.2020.126065
289. Gao, Y.S., Chen, G.H., Wang, X.R., et al.: PY13FSI-infiltrated SBA-15 as nonflammable and high ion-conductive ionogel electrolytes for quasi-solid-state sodium-ion batteries. ACS Appl. Mater. Interfaces **12**, 22981–22991 (2020). https://doi.org/10.1021/acsami.0c04878
290. Wu, F., Zhang, K., Liu, Y.R., et al.: Polymer electrolytes and interfaces toward solid-state batteries: recent advances and prospects. Energy Storage Mater. **33**, 26–54 (2020). https://doi.org/10.1016/j.ensm.2020.08.002
291. Chen, G.H., Ye, L., Zhang, K., et al.: Hyperbranched polyether boosting ionic conductivity of polymer electrolytes for all-solid-state sodium ion batteries. Chem. Eng. J. **394**, 124885 (2020). https://doi.org/10.1016/j.cej.2020.124885
292. Wang, C.W., Fu, K., Kammampata, S.P., et al.: Garnet-type solid-state electrolytes: materials, interfaces, and batteries. Chem. Rev. **120**, 4257–4300 (2020). https://doi.org/10.1021/acs.chemrev.9b00427
293. Liu, J., Zhou, J.Q., Wang, M.F., et al.: A functional-gradient-structured ultrahigh modulus solid polymer electrolyte for all-solid-state lithium metal batteries. J. Mater. Chem. A **7**, 24477–24485 (2019). https://doi.org/10.1039/C9TA07876B
294. Kwak, W.J., Rosy, D.S., et al.: Lithium-oxygen batteries and related systems: potential, status, and future. Chem. Rev. **120**, 6626–6683 (2020). https://doi.org/10.1021/acs.chemrev.9b00609
295. Lin, Y., Moitoso, B., Martinez-Martinez, C., et al.: Ultrahigh-capacity lithium-oxygen batteries enabled by dry-pressed holey graphene air cathodes. Nano Lett. **17**, 3252–3260 (2017). https://doi.org/10.1021/acs.nanolett.7b00872
296. Song, H.Y., Xu, S.M., Li, Y.J., et al.: Hierarchically porous, ultrathick, "breathable" wood-derived cathode for lithium-oxygen batteries. Adv. Energy Mater. **8**, 1701203 (2018). https://doi.org/10.1002/aenm.201701203
297. Lee, Y., Park, S.H., Kim, S.H., et al.: High-rate and high-areal-capacity air cathodes with enhanced cycle life based on RuO_2/MnO_2 bifunctional electrocatalysts supported on CNT for pragmatic Li-O_2 batteries. ACS Catal. **8**, 2923–2934 (2018). https://doi.org/10.1021/acscatal.8b00248
298. Lacey, S.D., Walsh, E.D., Hitz, E., et al.: Highly compressible, binderless and ultrathick holey graphene-based electrode architectures. Nano Energy **31**, 386–392 (2017). https://doi.org/10.1016/j.nanoen.2016.11.005
299. Zhu, C.L., Du, L., Luo, J.M., et al.: A renewable wood-derived cathode for Li-O_2 batteries. J. Mater. Chem. A **6**, 14291–14298 (2018). https://doi.org/10.1039/c8ta04703k
300. Xu, S.M., Chen, C.J., Kuang, Y.D., et al.: Flexible lithium-CO_2 battery with ultrahigh capacity and stable cycling. Energy Environ. Sci. **11**, 3231–3237 (2018). https://doi.org/10.1039/C8EE01468J
301. Qiao, Y., Liu, Y., Chen, C.J., et al.: 3D-printed graphene oxide framework with thermal shock synthesized nanoparticles for Li-CO_2 batteries. Adv. Funct. Mater. **28**, 1805899 (2018). https://doi.org/10.1002/adfm.201805899
302. Zhao, T., Zhang, G.M., Zhou, F.S., et al.: Toward tailorable Zn-ion textile batteries with high energy density and ultrafast capability: building high-performance textile electrode in 3D hierarchical branched design. Small **14**, 1802320 (2018). https://doi.org/10.1002/smll.201802320
303. Jiao, T.P., Yang, Q., Wu, S.L., et al.: Binder-free hierarchical VS_2 electrodes for high-performance aqueous Zn ion batteries towards commercial level mass loading. J. Mater. Chem. A **7**, 16330–16338 (2019). https://doi.org/10.1039/C9TA04798K
304. Zhang, W., Liang, S.Q., Fang, G.Z., et al.: Ultra-high mass-loading cathode for aqueous zinc-ion battery based on graphene-wrapped aluminum vanadate nanobelts. Nano-Micro Lett. **11**, 1–12 (2019). https://doi.org/10.1007/s40820-019-0300-2
305. Wei, T.Y., Li, Q., Yang, G.Z., et al.: Pseudo-Zn-air and Zn-ion intercalation dual mechanisms to realize high-areal capacitance and long-life energy storage in aqueous Zn battery. Adv. Energy

Mater. **9**, 1901480 (2019). https://doi.org/10.1002/aenm.201901480
306. Zhang, H.Z., Fang, Y.B., Yang, F., et al.: Aromatic organic molecular crystal with enhanced π–π stacking interaction for ultrafast Zn-ion storage. Energy Environ. Sci. **13**, 2515–2523 (2020). https://doi.org/10.1039/d0ee01723j
307. Ni, Q., Jiang, H., Sandstrom, S., et al.: A $Na_3V_2(PO_4)_2O_{1.6}F_{1.4}$ cathode of Zn-ion battery enabled by a water-in-bisalt electrolyte. Adv. Funct. Mater. **30**, 2003511 (2020). https://doi.org/10.1002/adfm.202003511
308. Yu, P., Zeng, Y.X., Zhang, H.Z., et al.: Flexible Zn-ion batteries: Recent progresses and challenges. Small **15**, 1804760 (2019). https://doi.org/10.1002/smll.201804760
309. Song, M., Tan, H., Chao, D.L., et al.: Recent advances in Zn-ion batteries. Adv. Funct. Mater. **28**, 1802564 (2018). https://doi.org/10.1002/adfm.201802564
310. Wang, Y.R., Wang, C.X., Ni, Z.G., et al.: Binding zinc ions by carboxyl groups from adjacent molecules toward long-life aqueous zinc-organic batteries. Adv. Mater. **32**, 2000338 (2020). https://doi.org/10.1002/adma.202000338
311. Xing, L.L., Owusu, K.A., Liu, X.Y., et al.: Insights into the storage mechanism of VS_4 nanowire clusters in aluminum-ion battery. Nano Energy **79**, 105384 (2021). https://doi.org/10.1016/j.nanoen.2020.105384
312. Wang, H.L., Gu, S.C., Bai, Y., et al.: Anion-effects on electrochemical properties of ionic liquid electrolytes for rechargeable aluminum batteries. J. Mater. Chem. A **3**, 22677–22686 (2015). https://doi.org/10.1039/C5TA06187C
313. Zhang, Y., Liu, S.Q., Ji, Y.J., et al.: Emerging nonaqueous aluminum-ion batteries: challenges, status, and perspectives. Adv. Mater. **30**, 1706310 (2018). https://doi.org/10.1002/adma.201706310
314. Wu, F., Yang, H.Y., Bai, Y., et al.: Paving the path toward reliable cathode materials for aluminum-ion batteries. Adv. Mater. **31**, 1806510 (2019). https://doi.org/10.1002/adma.201806510
315. Gu, S.C., Wang, H.L., Wu, C., et al.: Confirming reversible Al^{3+} storage mechanism through intercalation of Al^{3+} into V_2O_5 nanowires in a rechargeable aluminum battery. Energy Storage Mater. **6**, 9–17 (2017). https://doi.org/10.1016/j.ensm.2016.09.001
316. Zhu, N., Wu, F., Wang, Z.H., et al.: Reversible Al^{3+} storage mechanism in anatase TiO_2 cathode material for ionic liquid electrolyte-based aluminum-ion batteries. J. Energy Chem. **51**, 72–80 (2020). https://doi.org/10.1016/j.jechem.2020.03.032
317. Dong, X.Z., Xu, H.Y., Chen, H., et al.: Commercial expanded graphite as high-performance cathode for low-cost aluminum-ion battery. Carbon **148**, 134–140 (2019). https://doi.org/10.1016/j.carbon.2019.03.080
318. Muñoz-Torrero, D., Molina, A., Palma, J., et al.: Widely commercial carbonaceous materials as cathode for Al-ion batteries. Carbon **167**, 475–484 (2020). https://doi.org/10.1016/j.carbon.2020.06.019
319. Park, J., Xu, Z.L., Yoon, G., et al.: Stable and high-power calcium-ion batteries enabled by calcium intercalation into graphite. Adv. Mater. **32**, 1904411 (2020). https://doi.org/10.1002/adma.201904411
320. Cheng, X., Zhang, Z., Kong, Q., et al.: Highly reversible cuprous mediated cathode chemistry for magnesium batteries. Angew Chem Int Ed Engl **59**, 11477–11482 (2020). https://doi.org/10.1002/anie.202002177
321. Gummow, R.J., Vamvounis, G., Kannan, M.B., et al.: Calcium-ion batteries: current state-of-the-art and future perspectives. Adv. Mater. **30**, 1801702 (2018). https://doi.org/10.1002/adma.201801702
322. Murata, Y., Takada, S., Obata, T., et al.: Effect of water in electrolyte on the Ca^{2+} insertion/extraction properties of V_2O_5. Electrochim. Acta **294**, 210–216 (2019). https://doi.org/10.1016/j.electacta.2018.10.103
323. Zhang, Y.F., Geng, H.B., Wei, W.F., et al.: Challenges and recent progress in the design of advanced electrode materials for rechargeable Mg batteries. Energy Storage Mater. **20**, 118–138 (2019). https://doi.org/10.1016/j.ensm.2018.11.033
324. Yoo, H.D., Shterenberg, I., Gofer, Y., et al.: Mg rechargeable batteries: an on-going challenge. Energy Environ. Sci. **6**, 2265 (2013). https://doi.org/10.1039/c3ee40871j
325. Aravindan, V., Gnanaraj, J., Lee, Y.S., et al.: Insertion-type electrodes for nonaqueous Li-ion capacitors. Chem. Rev. **114**, 11619–11635 (2014). https://doi.org/10.1021/cr5000915
326. Wang, X., Kajiyama, S., Iinuma, H., et al.: Pseudocapacitance of MXene nanosheets for high-power sodium-ion hybrid capacitors. Nat. Commun. **6**, 6544 (2015). https://doi.org/10.1038/ncomms7544
327. Yang, J.L., Ju, Z.C., Jiang, Y., et al.: Enhanced capacity and rate capability of nitrogen/oxygen dual-doped hard carbon in capacitive potassium-ion storage. Adv. Mater. **30**, 1700104 (2018). https://doi.org/10.1002/adma.201700104
328. Song, Z.Q., Li, W.Y., Bao, Y., et al.: A new route to tailor high mass loading all-solid-state supercapacitor with ultra-high volumetric energy density. Carbon **136**, 46–53 (2018). https://doi.org/10.1016/j.carbon.2018.04.036
329. Vijayakumar, M., Santhosh, R., Adduru, J., et al.: Activated carbon fibres as high performance supercapacitor electrodes with commercial level mass loading. Carbon **140**, 465–476 (2018). https://doi.org/10.1016/j.carbon.2018.08.052
330. Wu, L.L., Liu, M.Q., Huo, S.L., et al.: Mold-casting prepared free-standing activated carbon electrodes for capacitive deionization. Carbon **149**, 627–636 (2019). https://doi.org/10.1016/j.carbon.2019.04.102
331. Ma, X.L., Song, X.Y., Yu, Z.Q., et al.: S-doping coupled with pore-structure modulation to conducting carbon black: toward high mass loading electrical double-layer capacitor. Carbon **149**, 646–654 (2019). https://doi.org/10.1016/j.carbon.2019.04.110
332. Liu, L.Y., Wang, X.H., Izotov, V., et al.: Capacitance of coarse-grained carbon electrodes with thickness up to 800 μm. Electrochim. Acta **302**, 38–44 (2019). https://doi.org/10.1016/j.electacta.2019.02.004
333. Huang, T.Q., Chu, X.Y., Cai, S.Y., et al.: Tri-high designed graphene electrodes for long cycle-life supercapacitors with high mass loading. Energy Storage Mater. **17**, 349–357 (2019). https://doi.org/10.1016/j.ensm.2018.07.001
334. Yuan, G., Liang, Y.R., Hu, H., et al.: Extraordinary thickness-independent electrochemical energy storage enabled by cross-linked microporous carbon nanosheets. ACS Appl. Mater. Interfaces **11**, 26946–26955 (2019). https://doi.org/10.1021/acsami.9b06402
335. Song, Y., Liu, T., Yao, B., et al.: Ostwald ripening improves rate capability of high mass loading manganese oxide for supercapacitors. ACS Energy Lett. **2**, 1752–1759 (2017). https://doi.org/10.1021/acsenergylett.7b00405
336. Huang, Z.H., Song, Y., Feng, D.Y., et al.: High mass loading MnO_2 with hierarchical nanostructures for supercapacitors. ACS Nano **12**, 3557–3567 (2018). https://doi.org/10.1021/acsnano.8b00621
337. Li, H., Tao, Y., Zheng, X.Y., et al.: Ultra-thick graphene bulk supercapacitor electrodes for compact energy storage. Energy Environ. Sci. **9**, 3135–3142 (2016). https://doi.org/10.1039/c6ee00941g
338. Zhang, M., Yu, X.W., Ma, H.Y., et al.: Robust graphene composite films for multifunctional electrochemical capacitors with an ultrawide range of areal mass loading toward high-rate frequency response and ultrahigh specific capacitance. Energy Environ. Sci. **11**, 559–565 (2018). https://doi.org/10.1039/c7ee03349d

339. VahidMohammadi, A., Moncada, J., Chen, H.Z., et al.: Thick and freestanding MXene/PANI pseudocapacitive electrodes with ultrahigh specific capacitance. J. Mater. Chem. A **6**, 22123–22133 (2018). https://doi.org/10.1039/C8TA05807E
340. Liu, J.C., Li, H., Batmunkh, M., et al.: Structural engineering to maintain the superior capacitance of molybdenum oxides at ultrahigh mass loadings. J. Mater. Chem. A **7**, 23941–23948 (2019). https://doi.org/10.1039/C9TA04835A
341. Cai, X., Song, Y., Wang, S.Q., et al.: Extending the cycle life of high mass loading MoO_x electrode for supercapacitor applications. Electrochim. Acta **325**, 134877 (2019). https://doi.org/10.1016/j.electacta.2019.134877
342. Qi, Z., Ye, J.C., Chen, W., et al.: 3D-printed, superelastic polypyrrole-graphene electrodes with ultrahigh areal capacitance for electrochemical energy storage. Adv. Mater. Technol. **3**, 1800053 (2018). https://doi.org/10.1002/admt.201800053
343. Li, X., Shao, J., Kim, S.K., et al.: High energy flexible supercapacitors formed via bottom-up infilling of gel electrolytes into thick porous electrodes. Nat. Commun. **9**, 2578 (2018). https://doi.org/10.1038/s41467-018-04937-8
344. Song, Y., Liu, T., Li, M.Y., et al.: Engineering of mesoscale pores in balancing mass loading and rate capability of hematite films for electrochemical capacitors. Adv. Energy Mater. **8**, 1801784 (2018). https://doi.org/10.1002/aenm.201801784
345. Yao, B., Chandrasekaran, S., Zhang, J., et al.: Efficient 3D printed pseudocapacitive electrodes with ultrahigh MnO_2 loading. Joule **3**, 459–470 (2019). https://doi.org/10.1016/j.joule.2018.09.020
346. Guo, S.Q., Li, H.C., Zhang, X., et al.: Lignin carbon aerogel/nickel binary network for cubic supercapacitor electrodes with ultra-high areal capacitance. Carbon (2020). https://doi.org/10.1016/j.carbon.2020.12.051
347. Liu, K., Mo, R.W., Dong, W.J., et al.: Nature-derived, structure and function integrated ultra-thick carbon electrode for high-performance supercapacitors. J. Mater. Chem. A **8**, 20072–20081 (2020). https://doi.org/10.1039/D0TA06108E
348. Zhao, J., Li, Y.J., Wang, G.L., et al.: Enabling high-volumetric-energy-density supercapacitors: designing open, low-tortuosity heteroatom-doped porous carbon-tube bundle electrodes. J. Mater. Chem. A **5**, 23085–23093 (2017). https://doi.org/10.1039/C7TA07010A
349. Lv, Z., Tang, Y., Zhu, Z., et al.: Honeycomb-lantern-inspired 3D stretchable supercapacitors with enhanced specific areal capacitance. Adv. Mater. **30**, e1805468 (2018). https://doi.org/10.1002/adma.201805468
350. Huo, S.L., Liu, M.Q., Wu, L.L., et al.: Synthesis of ultrathin and hierarchically porous carbon nanosheets based on interlayer-confined inorganic/organic coordination for high performance supercapacitors. J. Power Sources **414**, 383–392 (2019). https://doi.org/10.1016/j.jpowsour.2019.01.028
351. Huo, S.L., Liu, M.Q., Wu, L.L., et al.: Methanesulfonic acid-assisted synthesis of N/S co-doped hierarchically porous carbon for high performance supercapacitors. J. Power Sources **387**, 81–90 (2018). https://doi.org/10.1016/j.jpowsour.2018.03.061
352. Wang, J.F., Wang, J.R., Kong, Z., et al.: Conducting-polymer-based materials for electrochemical energy conversion and storage. Adv. Mater. **29**, 1703044 (2017). https://doi.org/10.1002/adma.201703044
353. Zhang, Z.T., Liao, M., Lou, H.Q., et al.: Conjugated polymers for flexible energy harvesting and storage. Adv. Mater. **30**, 1704261 (2018). https://doi.org/10.1002/adma.201704261
354. Liao, C.R., Xiong, F., Li, X.J., et al.: Progress in conductive polymers in fibrous energy devices. Acta Phys. Chim. Sin. **33**, 329–343 (2017)
355. Fan, Z.Y., Islam, N., Bayne, S.B.: Towards kilohertz electrochemical capacitors for filtering and pulse energy harvesting. Nano Energy **39**, 306–320 (2017). https://doi.org/10.1016/j.nanoen.2017.06.048
356. Feng, D.W., Lei, T., Lukatskaya, M.R., et al.: Robust and conductive two-dimensional metal−organic frameworks with exceptionally high volumetric and areal capacitance. Nat. Energy **3**, 30–36 (2018). https://doi.org/10.1038/s41560-017-0044-5
357. Yang, Z.Y., Jin, L.J., Lu, G.Q., et al.: Sponge-templated preparation of high surface area graphene with ultrahigh capacitive deionization performance. Adv. Funct. Mater. **24**, 3917–3925 (2014). https://doi.org/10.1002/adfm.201304091
358. Li, L., Zhang, N., Zhang, M.Y., et al.: Ag-nanoparticle-decorated 2D titanium carbide (MXene) with superior electrochemical performance for supercapacitors. ACS Sustain. Chem. Eng. **6**, 7442–7450 (2018). https://doi.org/10.1021/acssuschemeng.8b00047
359. Li, L., Zhang, M.Y., Zhang, X.T., et al.: New Ti_3C_2 aerogel as promising negative electrode materials for asymmetric supercapacitors. J. Power Sources **364**, 234–241 (2017). https://doi.org/10.1016/j.jpowsour.2017.08.029
360. Guo, M., Liu, C.B., Zhang, Z.Z., et al.: Flexible $Ti_3C_2T_x$@Al electrodes with ultrahigh areal capacitance: in situ regulation of interlayer conductivity and spacing. Adv. Funct. Mater. **28**, 1803196 (2018). https://doi.org/10.1002/adfm.201803196
361. Xia, Y., Mathis, T.S., Zhao, M.Q., et al.: Thickness-independent capacitance of vertically aligned liquid-crystalline MXenes. Nature **557**, 409–412 (2018). https://doi.org/10.1038/s41586-018-0109-z
362. Wang, Y.M., Wang, X., Li, X.L., et al.: Engineering 3D ion transport channels for flexible MXene films with superior capacitive performance. Adv. Funct. Mater. **29**, 1900326 (2019). https://doi.org/10.1002/adfm.201900326
363. Kong, J., Yang, H.C., Guo, X.Z., et al.: High-mass-loading porous $Ti_3C_2T_x$ films for ultrahigh-rate pseudocapacitors. ACS Energy Lett. **5**, 2266–2274 (2020). https://doi.org/10.1021/acsenergylett.0c00704
364. Wang, Y.M., Lin, X.J., Liu, T., et al.: Wood-derived hierarchically porous electrodes for high-performance all-solid-state supercapacitors. Adv. Funct. Mater. **28**, 1806207 (2018). https://doi.org/10.1002/adfm.201806207
365. Hu, L.Y., Gao, R., Zhang, A.Q., et al.: Cu^{2+} intercalation activates bulk redox reactions of MnO_2 for enhancing capacitive performance. Nano Energy **74**, 104891 (2020). https://doi.org/10.1016/j.nanoen.2020.104891
366. Feng, D.Y., Sun, Z., Huang, Z.H., et al.: Highly loaded manganese oxide with high rate capability for capacitive applications. J. Power Sources **396**, 238–245 (2018). https://doi.org/10.1016/j.jpowsour.2018.06.026
367. Zhang, Y., Yuan, X.M., Lu, W.B., et al.: MnO_2 based sandwich structure electrode for supercapacitor with large voltage window and high mass loading. Chem. Eng. J. **368**, 525–532 (2019). https://doi.org/10.1016/j.cej.2019.02.206
368. Chen, C.F., Verma, A., Mukherjee, P.P.: Probing the role of electrode microstructure in the lithium-ion battery thermal behavior. J. Electrochem. Soc. **164**, E3146–E3158 (2017). https://doi.org/10.1149/2.0161711jes
369. Yang, C., Xin, S., Mai, L.Q., et al.: Materials design for high-safety sodium-ion battery. Adv. Energy Mater. (2020). https://doi.org/10.1002/aenm.202000974
370. Li, H., Qi, C.S., Tao, Y., et al.: Quantifying the volumetric performance metrics of supercapacitors. Adv. Energy Mater. **9**, 1900079 (2019). https://doi.org/10.1002/aenm.201900079
371. Xiao, K.F., Pan, J., Liang, K., et al.: Layered conductive polymer-inorganic anion network for high-performance ultra-loading capacitive electrodes. Energy Storage Mater. **14**, 90–99 (2018). https://doi.org/10.1016/j.ensm.2018.02.018
372. Xu, Y., Tao, Y., Zheng, X.Y., et al.: A metal-free supercapacitor electrode material with a record high volumetric capacitance over

800 F cm^{-3}. Adv. Mater. **27**, 8082–8087 (2015). https://doi.org/10.1002/adma.201504151
373. Bu, Y.F., Sun, T., Cai, Y.J., et al.: Compressing carbon nanocages by capillarity for optimizing porous structures toward ultrahigh-volumetric-performance supercapacitors. Adv. Mater. **29**, 1700470 (2017). https://doi.org/10.1002/adma.201700470
374. Ghidiu, M., Lukatskaya, M.R., Zhao, M.Q., et al.: Conductive two-dimensional titanium carbide "clay" with high volumetric capacitance. Nature **516**, 78–81 (2014). https://doi.org/10.1038/nature13970
375. Murali, S., Quarles, N., Zhang, L.L., et al.: Volumetric capacitance of compressed activated microwave-expanded graphite oxide (a-MEGO) electrodes. Nano Energy **2**, 764–768 (2013). https://doi.org/10.1016/j.nanoen.2013.01.007
376. Xu, Y., Lin, Z., Zhong, X., et al.: Holey graphene frameworks for highly efficient capacitive energy storage. Nat. Commun. **5**, 4554 (2014). https://doi.org/10.1038/ncomms5554
377. Ma, H.Y., Kong, D.B., Xu, Y., et al.: Disassembly-reassembly approach to RuO_2/graphene composites for ultrahigh volumetric capacitance supercapacitor. Small **13**, 1701026 (2017). https://doi.org/10.1002/smll.201701026
378. Zhao, X., Zhang, L.L., Murali, S., et al.: Incorporation of manganese dioxide within ultraporous activated graphene for high-performance electrochemical capacitors. ACS Nano **6**, 5404–5412 (2012). https://doi.org/10.1021/nn3012916
379. Yang, X., Cheng, C., Wang, Y., et al.: Liquid-mediated dense integration of graphene materials for compact capacitive energy storage. Science **341**, 534–537 (2013). https://doi.org/10.1126/science.1239089
380. Acerce, M., Voiry, D., Chhowalla, M.: Metallic 1T phase MoS_2 nanosheets as supercapacitor electrode materials. Nat. Nanotechnol. **10**, 313–318 (2015). https://doi.org/10.1038/nnano.2015.40
381. Zhang, W., Topsakal, M., Cama, C., et al.: Multi-stage structural transformations in zero-strain lithium titanate unveiled by *in situ* X-ray absorption fingerprints. J. Am. Chem. Soc. **139**, 16591–16603 (2017). https://doi.org/10.1021/jacs.7b07628
382. Ciez, R.E., Steingart, D.: Asymptotic cost analysis of intercalation lithium-ion systems for multi-hour duration energy storage. Joule **4**, 597–614 (2020). https://doi.org/10.1016/j.joule.2020.01.007
383. Adams, R.A., Varma, A., Pol, V.G.: Carbon anodes for nonaqueous alkali metal-ion batteries and their thermal safety aspects. Adv. Energy Mater. **9**, 1900550 (2019). https://doi.org/10.1002/aenm.201900550
384. Mei, W.X., Chen, H.D., Sun, J.H., et al.: The effect of electrode design parameters on battery performance and optimization of electrode thickness based on the electrochemical–thermal coupling model. Sustain. Energy Fuels **3**, 148–165 (2019). https://doi.org/10.1039/c8se00503f
385. Lin, H.P., Chua, D., Salomon, M., et al.: Low-temperature behavior of Li-ion cells. Electrochem. Solid-State Lett. **4**, A71 (2001). https://doi.org/10.1149/1.1368736
386. Spotnitz, R., Franklin, J.: Abuse behavior of high-power, lithium-ion cells. J. Power Sources **113**, 81–100 (2003). https://doi.org/10.1016/S0378-7753(02)00488-3
387. Li, H., Wu, D.B., Wu, J., et al.: Flexible, high-wettability and fire-resistant separators based on hydroxyapatite nanowires for advanced lithium-ion batteries. Adv. Mater. **29**, 1703548 (2017). https://doi.org/10.1002/adma.201703548
388. Lei, D.N., Benson, J., Magasinski, A., et al.: Transformation of bulk alloys to oxide nanowires. Science **355**, 267–271 (2017). https://doi.org/10.1126/science.aal2239
389. Wang, J.H., Yamada, Y., Sodeyama, K., et al.: Fire-extinguishing organic electrolytes for safe batteries. Nat. Energy **3**, 22–29 (2018). https://doi.org/10.1038/s41560-017-0033-8
390. Wang, Z.Q., Tan, R., Wang, H.B., et al.: A metal-organic-framework-based electrolyte with nanowetted interfaces for high-energy-density solid-state lithium battery. Adv. Mater. **30**, 1704436 (2018). https://doi.org/10.1002/adma.201704436
391. Simon, P., Gogotsi, Y.: Capacitive energy storage in nanostructured carbon-electrolyte systems. Acc. Chem. Res. **46**, 1094–1103 (2013). https://doi.org/10.1021/ar200306b
392. Thomitzek, M., Schmidt, O., Röder, F., et al.: Simulating process-product interdependencies in battery production systems. Procedia CIRP **72**, 346–351 (2018). https://doi.org/10.1016/j.procir.2018.03.056
393. Shi, S.Q., Gao, J., Liu, Y., et al.: Multi-scale computation methods: their applications in lithium-ion battery research and development. Chin. Phys. B **25**, 178–201 (2016)
394. Pecher, O., Carretero-González, J., Griffith, K.J., et al.: Materials' methods: NMR in battery research. Chem. Mater. **29**, 213–242 (2017). https://doi.org/10.1021/acs.chemmater.6b03183
395. Li, Y.Z., Yan, K., Lee, H.W., et al.: Growth of conformal graphene cages on micrometre-sized silicon particles as stable battery anodes. Nat. Energy **1**, 15029 (2016). https://doi.org/10.1038/nenergy.2015.29
396. Li, Y., Li, Y., Pei, A., et al.: Atomic structure of sensitive battery materials and interfaces revealed by cryo-electron microscopy. Science **358**, 506–510 (2017). https://doi.org/10.1126/science.aam6014
397. Nelson, J., Misra, S., Yang, Y., et al.: In operando X-ray diffraction and transmission X-ray microscopy of lithium sulfur batteries. J. Am. Chem. Soc. **134**, 6337–6343 (2012). https://doi.org/10.1021/ja2121926
398. Wood, D.L., Li, J.L., Daniel, C.: Prospects for reducing the processing cost of lithium ion batteries. J. Power Sources **275**, 234–242 (2015). https://doi.org/10.1016/j.jpowsour.2014.11.019
399. Ciez, R.E., Whitacre, J.F.: Comparison between cylindrical and prismatic lithium-ion cell costs using a process based cost model. J. Power Sources **340**, 273–281 (2017). https://doi.org/10.1016/j.jpowsour.2016.11.054

Feng Wu is the director of the Green Energy Research Institute, and the vice president of the China Battery Industry Association. As the chief scientist, he has hosted three "National Program on Key Basic Research Projects (973 Programs)". He has published over 500 peer-reviewed papers. In 2012, he was awarded the IBA Research Award for outstanding research of battery material and systems for electric vehicles. In 2017, Prof. Wu was elected as an academician of the Chinese Academy of Engineering.

Mingquan Liu received his Bachelor's degree (2016) and Master's degree (2019) from Northeast Forestry University and the Beijing Institute of Technology (BIT), respectively. He is currently a Ph.D. candidate under the supervision of Professor Feng Wu in the School of Materials Science and Engineering, BIT. His research interests focus on structure engineering of carbon materials for supercapacitors and sodium-ion batteries.

Ying Li is currently a Ph.D. candidate in the School of Materials Science and Engineering at the Beijing Institute of Technology, where she received her M.S. degree in 2019. She received her B.S. degree at the University of Science and Technology Beijing. Her research focuses on silicon-based materials for high performance sodium ion batteries.

Xin Feng received his M.S. degree in the School of Materials Science and Engineering at Wenzhou University in 2016. He is currently a Ph.D. candidate at the Beijing Institute of Technology. His research focuses on materials for high performance supercapacitors and sodium ion batteries.

Kun Zhang is currently a Ph.D. candidate under the supervision of Professor Feng Wu in the School of Materials Science and Engineering, Beijing Institute of Technology (BIT). She received her B.S. degree from Shandong Normal University in 2014 and obtained her M.S. degree from the BIT in 2017. Her research interests mainly focus on polymer materials and related applications in solid-state batteries.

Ying Bai is currently a professor at the Beijing Institute of Technology (BIT). Her research interests focus on electrochemical energy storage and conversion technology. Dr. Bai earned her bachelor degree from the Applied Chemistry Division at the Harbin Institute of Technology (HIT), China in 1997. She completed her Ph.D. from the School of Chemical Engineering and Materials Science at the BIT in 2003. In 2013, she was awarded "New Century Excellent Talents in University" from the Chinese Ministry of Education. She hosted and is hosting the projects of the National Natural Science Foundation of China as a principal investigator.

Xinran Wang received his Ph.D. and B.S. from the University of Chinese Academy of Sciences. He is currently an associate professor in the School of Materials Science and Engineering at the Beijing Institute of Technology (BIT). His current researches focused on advanced multi-electron reaction materials for use in rechargeable batteries and energy storage.

Chuan Wu is a professor at the Beijing Institute of Technology (BIT), where his research interests are new materials for energy conversion and storage, and secondary batteries based on multi-electron materials. He received his Ph.D. degree in Applied Chemistry from the BIT in 2002, followed by a 2-year postdoctoral fellowship in the Dalian Institute of Chemical Physics, Chinese Academy of Sciences. Dr. Wu was awarded the Beijing Outstanding Talents Cultivation Project in 2007, the Beijing Nova Program Award in 2009, and "New Century Excellent Talents in University" in 2012.